



UNIVERSITÀ DEGLI STUDI DI TRENTO

CIMeC - Center for Mind/Brain Sciences

Doctorate School in Cognitive and Brain Sciences: 36th cycle

A computational study of the origin of brain oscillations at multiple scales

Candidate: Shahryar Noei

Supervisor: Stefano Panzeri

Neural Computation Lab, Center for Neuroscience and Cognitive Systems,
Istituto Italiano di Tecnologia, Rovereto, IT;

Center for Mind/Brain Sciences (CIMeC), University of Trento.

This dissertation is submitted for the degree of Doctor of Philosophy

November 2022

AUTHOR

Shahryar Noei

Neural Computational Lab, Center for Neuroscience and Cognitive Systems,
Istituto Italiano di Tecnologia, Rovereto, IT;

Center for Mind/Brain Sciences, University of Trento;

C.so Bettini, 31

38068 Rovereto (TN), IT.

EMAIL

shahryar.noei@iit.it, shahryr.noei@unitn.it, sh.noei69@gmail.com.

DECLARATION

This dissertation is the result of my work unless specifically cited and acknowledged as material from another source. It has never been submitted to any other institute for any degree/diploma.

Signed:

Shahryar Noei

Date:

23/10/2022

Shahryar Noei

ABSTRACT

Brain activity recordings from multiple locations from the brain at rest often demonstrate dynamic spatiotemporal reconfigurations of oscillatory activity. These oscillatory patterns are observed both using indirect recordings of neural activity, such as resting-state functional magnetic resonance imaging (rs-fMRI), or direct recording of neural activity with electrophysiology. The origin and role of such oscillatory patterns and their relationship between those observed with fMRI and electrophysiology is the subject of much investigation. Here I present computational work that sheds light on these questions.

In our first study, I analyzed data from the lab of Alessandro Gozzi to demonstrate that changes in the resting-state fMRI connectivity caused by chemogenetic chronic inhibition of the prefrontal cortex (PFC) are reflected by an increase of slow oscillatory power (<4 Hz) in the local field potential and an increase of coherence in those bands, suggesting that rs-fMRI connectivity primarily reflects low-frequency neural oscillations.

In the second study, I analyzed data from the lab of Nelson Totah to investigate how prefrontal cortical oscillations are modulated by variations in the activity of ascending neuromodulatory systems. Noradrenergic Locus Coeruleus (LC) is a major neuromodulatory system and is believed to regulate the excitability of cortical targets by an en-masse synchronous increase of firing, and the changes in excitability. A recent study, however, has demonstrated a low observed correlation among LC pairs during anesthesia and has paved the way for potential ensemble-based modulation of the cortex. Here, utilizing the non-negative matrix factorization technique on populations of tens of simultaneously recorded neurons in anesthetized rats, we found multiple ensembles of LC cells with diverse spatiotemporal properties. Aligning the ongoing rhythms of the prefrontal cortex (PFC) around the activation of different LC ensembles, we found that the pattern of oscillations in the prefrontal cortex varied dynamically depending on which LC ensemble was active. Our results demonstrate that the spontaneous activity of LC ensembles can be associated with different oscillatory cortical states.

ACKNOWLEDGEMENTS

I would like to thank everybody who supported me in all my endeavors. I appreciate all the great life lessons that I've learned in the past 4 years.

Especially, I would like to express my gratitude towards Stefano Panzeri, for his supervision and help in designing, interpreting, and writing the methods/results of the computational part of the studies, Nelson Totah for sharing data, all his great feedback, and for writing a major part of the "PNAS" paper, my dear friend Federico Rocchi for collecting the data and all the great time we have spent together (both inside/outside work), and Alessandro Gozzi for entrusting me to be part of his research, all his interpretations of the results and his contribution in writing most of the "nature communication" paper's manuscript.

TABLE OF CONTENTS

| | | |
|--------|--|----|
| 1 | Introduction..... | 1 |
| 2 | Chemogenetic manipulation of Brain Oscillations | 8 |
| 2.1 | Introduction | 8 |
| 2.2 | Methods | 10 |
| 2.2.1 | Ethical statement | 10 |
| 2.2.2 | Animals..... | 11 |
| 2.2.3 | Anatomical definition of mouse medial prefrontal cortex..... | 11 |
| 2.2.4 | Viral injections | 11 |
| 2.2.5 | rsfMRI acquisitions..... | 12 |
| 2.2.6 | Image preprocessing and analysis | 13 |
| 2.2.7 | Electrophysiological recordings | 16 |
| 2.2.8 | Multielectrode coherence | 20 |
| 2.2.9 | Power spectrum of simulated spiking activity..... | 22 |
| 2.2.10 | Relationships between spikes and LFP phases | 22 |
| 2.2.11 | LFP-LFP phase differences | 23 |
| 2.3 | Results | 24 |
| 2.3.1 | rsfMRI overconnectivity upon chronic inactivation of the mouse prefrontal cortex | 24 |
| 2.3.2 | rsfMRI overconnectivity upon acute chemogenetic inactivation of the mouse prefrontal cortex | 28 |
| 2.3.3 | Chemogenetic inhibition of the prefrontal cortex leads to thalamo-cortical rsfMRI overconnectivity | 34 |
| 2.3.4 | Chemogenetic inactivation of the prefrontal cortex inhibits firing not locked to slow rhythms, resulting in increased slow oscillatory power | 37 |

| | | |
|-------|--|----|
| 2.3.5 | Chemogenetic inhibition of the prefrontal cortex increases interareal slow oscillatory coherence | 42 |
| 2.4 | Discussion..... | 47 |
| 3 | Locus Coeruleus and cortical states | 54 |
| 3.1 | Introduction | 54 |
| 3.2 | Materials and Methods..... | 57 |
| 3.2.1 | Rats and recording procedures..... | 57 |
| 3.2.2 | NMF decomposition | 58 |
| 3.2.3 | The evaluation of physical clustering of ensembles according to location on the recording array..... | 60 |
| 3.2.4 | Spike train simulation | 61 |
| 3.2.5 | The assignment of single unit types in the ensembles..... | 62 |
| 3.2.6 | Auto- and cross-correlograms and permutation testing..... | 62 |
| 3.2.7 | Definition of the synchrony index | 62 |
| 3.2.8 | LC ensemble activation-aligned averaged LFP spectrogram and BLP modulations..... | 63 |
| 3.2.9 | Spectrogram clustering..... | 64 |
| 3.3 | Results | 65 |
| 3.3.1 | NMF detects the neuronal composition and activation times of ensembles..... | 65 |
| 3.3.2 | Spontaneous LC population activity consists of distinct ensembles with largely non-overlapping activation dynamics | 69 |
| 3.3.3 | LC ensembles are temporally distinct and are sparsely active..... | 74 |
| 3.3.4 | LC ensembles can be synchronously active..... | 76 |
| 3.3.5 | Spontaneous activation of distinct LC ensembles is associated with different cortical states | 77 |

| | | |
|-------|--|-----|
| 3.3.6 | Synchronous spontaneous activation of a larger pool of LC ensembles results in a more homogeneous cortical state | 84 |
| 3.4 | Discussion..... | 86 |
| 3.4.1 | Potential neurophysiological causes of the diversity in cortical state 88 | |
| 3.4.2 | An LC ensemble code enables greater diversity in neuromodulatory functions | 89 |
| 4 | General Discussion | 91 |
| | List of Figures | 100 |
| | Bibliography | 102 |

1 INTRODUCTION

Much progress in the understanding of how networks in the brain interact to produce functions arises from simultaneous measurements of brain electrical activity from multiple recording sites (Pesaran *et al.*, 2018). Simultaneous recording of electrical signals from multiple areas has revealed that these signals show oscillatory nature over a wide range of frequencies with a power spectrum that may have local bumps (corresponding to increased power in specific frequency bands) but that in general follows a power law ($1/f^n$) shape (Buzsáki *et al.*, 2012; Einevoll *et al.*, 2013; Pesaran *et al.*, 2018; Mitra, Partha & Bokli, 2007; Mahmud and Vassanelli, 2016). A significant body of research has demonstrated that these oscillations are not simply a by-product of brain activity, but play a pivotal role in many cognitive functions (Martínez-Cañada *et al.*, 2021; Siegel *et al.*, 2012; Buzsaki, 2004; Singer, 1999; Donner and Siegel, 2011). Traditionally, these oscillations have been divided into wide frequency bands often referred to as delta (1-4 Hz), theta (4-8 Hz), alpha (8-12 Hz), beta (15-30 Hz), and gamma (30 – 100 Hz) (Martínez-Cañada *et al.*, 2021). Different bands have been hypothesized to play a role in shaping distinct brain states and sensory processing (Belitski *et al.*, 2008; Lakatos *et al.*, 2008; Ray and Maunsell, 2011; Pesaran *et al.*, 2018; Nunez and Srinivasan, 2006). The cortex during rest is believed to function under a synchronous state which is characterized by the dominance of power in slower frequencies (Harris and Thiele, 2011; Van Someren *et al.*, 2011). When recorded from multiple areas, These electrical oscillations show spatiotemporally correlated patterns at different frequencies (He *et al.*, 2008; Hipp *et al.*, 2012).

Additionally, brain electrical oscillations have been hypothesized to play a role in interactions between and within brain regions (Siegel *et al.*, 2012). Examples of famous theories regarding brain oscillations and communications are the communication through coherence (Fries, 2015) framework indicating that inter-regional communication is mediated by an increase in the gamma band coherency

and gating by inhibition (Jensen and Mazaheri, 2010) which hypothesizes that communication between regions is established through suppression of alpha band activity. Several studies have reported multiple features of brain oscillations to play a role in neuronal communication and how changes in brain state can shape those features (Siegel *et al.*, 2008; Brovelli *et al.*, 2004; Bastos *et al.*, 2015; Bosman *et al.*, 2012; Besserve *et al.*, 2010; Ferro *et al.*, 2021).

Brain activity at rest can also be monitored via indirect measurements such as blood oxygen level-dependent (BOLD) signal using functional Magnetic Resonance Imaging (rs-fMRI). Correlating the BOLD signal across different brain regions has served as a measure of functional communication between different brain regions (Friston, 2011; van den Heuvel and Hulshoff Pol, 2010). Applying such methods often demonstrate a set of repeated spatiotemporal correlated patterns in humans often referred to as resting-state networks (van den Heuvel and Hulshoff Pol, 2010). Animal studies in primates and rodents have also found resting-state networks resembling those of humans (Rilling *et al.*, 2007; Vincent *et al.*, 2007; Gutierrez-Barragan *et al.*, 2022; Liska *et al.*, 2015; Sforazzini *et al.*, 2014). Specifically, attention to studying rs-fMRI has been raised due to studies demonstrating that changes in rs-fMRI correlated patterns of activity are associated with brain dysfunctions (Power *et al.*, 2014). Examples are: reduced rs-fMRI connectivity in associative cortical regions for patients with schizophrenia (Huang *et al.*, 2010; Lynall *et al.*, 2010), stronger rs-fMRI coupling in the frontal and parietal regions in depression (L. Wang *et al.*, 2012), and reduced connectivity in prefrontal regions in patients suffering from bipolar disorder (Leichsenring *et al.*, 2011). Disruptions in rs-fMRI connectivity have also been observed in neurodevelopmental disorders such as Autism Spectrum Disorder (ASD). (Di Martino *et al.*, 2014; Holiga *et al.*, 2019; Hull *et al.*, 2017). Interestingly, changes in the patterns of rs-fMRI connectivity have also been observed in animal models of ASD (Zerbi *et al.*, 2021). Studies using resting-state electroencephalogram (EEG) have also associated changes in the spectral properties of the signal, with multiple psychiatric disorders (for a systemic review look (Newson and Thiagarajan, 2019)).

Despite the extensive use of rs-fMRI connectivity to study neural communication, the relationship between these functional connectivity measures and the correlations observed between neural electrical oscillations at different sites are poorly known. A pivotal study (Logothetis *et al.*, 2001) demonstrated that fluctuations of the BOLD signal due to visual stimuli in monkeys were largely correlated with changes in the gamma power of local field potentials (LFP). Subsequent studies found a similar relation between BOLD amplitude and the gamma power of LFP in cats, awake, and anesthetized monkeys' visual cortex (Kayser, 2004; Niessing *et al.*, 2005; Goense and Logothetis, 2008; Murayama *et al.*, 2010). While these studies were performed under stimulation, in (Schölvinck *et al.*, 2010), the authors demonstrated that global fluctuations of fMRI signal during rest in monkeys also correlate strongly with changes in the LFP gamma band power. This phenomenon was observed robustly across multiple cortical areas. Although most of these studies nominate gamma power as the best proxy for interpreting fMRI signal, authors in (Magri *et al.*, 2012) pointed out that despite the gamma band being most informative about the BOLD signal, both the alpha and beta band carry complementary information about the amplitude and latency of the BOLD signal. All these studies examined the relationship between the BOLD signal and the electrical oscillations locally. Using electrocorticography (ECoG) in humans (He *et al.*, 2008) found that the slow frequency correlation structure in the electrical oscillations was similar to what was observed by the spontaneous BOLD fluctuations. Similarly, low frequency (<20 Hz) coherence was demonstrated to explain the interareal BOLD correlations better than the gamma band (Liang Wang *et al.*, 2012). Another study suggested the delta band power coherence of LFP as the neural Correlate of resting-state fMRI signal in anesthetized rats (Lu *et al.*, 2007). While this relation between slower frequencies of the brain electrical oscillations and rs-fMRI connectivity has been reported in other studies as well (Neuner *et al.*, 2014; Chan *et al.*, 2017), some others have nominated the gamma power modulations (Nir *et al.*, 2008) or the ultraslow (0.1 Hz) fluctuations of the gamma power envelope coherence (Mateo *et al.*, 2017) as proxies for describing

rs-fMRI connectivity. These conflicting results would suggest that more investigations are needed for understanding the relationship between rs-fMRI connectivity and neural electrical oscillations,

Chemogenetic manipulations have been demonstrated to be able to causally affect rs-fMRI networks (Giorgi *et al.*, 2017; Grayson *et al.*, 2016; Peeters *et al.*, 2020; Tu *et al.*, 2021). This would enable researchers, to investigate the relation between rs-fMRI and brain electrical oscillations by correlating the imposed changes due to these manipulations in both signals. Here, in the first study presented in the 2nd chapter (Rocchi *et al.*, 2022), we tried to investigate the relation between rs-fMRI and electrical oscillations by studying how the effect of perturbation of one region to whole-brain connectivity in fMRI data caused by chronic inhibition of the medial prefrontal cortex (PFC) in anesthetized mice is reflected in brain electrical oscillations. (Rocchi *et al.*, 2022).

The changes in the spatiotemporal and spectrotemporal patterns of activity of neural oscillations are often associated with changes in brain states/cognitive states which are necessary for the brain to carry out multiple different behaviors (McCormick *et al.*, 2020; Harris and Thiele, 2011; McGinley *et al.*, 2015). These changes are not only modulated by the presence of external stimuli. They can also be caused by internal variations such as stress, hunger, or sleepiness. How these changes are controlled through internal brain mechanisms has been the subject of studies. They are believed to be partly modulated through the neuromodulatory systems (McCormick *et al.*, 2020; Harris and Thiele, 2011). Neuromodulators, usually placed in the brainstem or other subcortical areas, control brain states through local and broad projection of neurotransmitters (McCormick *et al.*, 2020). Neuromodulatory systems control the number of released neurotransmitters that can have both excitatory and inhibitory effects. The most well-known and investigated pathways are cholinergic, noradrenergic, serotonergic, and histaminergic (Jones, 2020; McCormick *et al.*, 2020). Neuromodulatory pathways can impact almost every possible function of the brain. For example, the excitability of pyramidal cells in the cortex can be

controlled by acetylcholine or norepinephrine which would in turn result in a change in brain state (McCormick *et al.*, 2020). Moreover, studies in awake mice have revealed a strong relationship between the activation of the cholinergic, and noradrenergic systems and whisking, and locomotion (Eggermann *et al.*, 2014; Lee *et al.*, 2014).

Among the neuromodulatory systems is the noradrenergic brainstem nucleus, locus coeruleus (LC), which controls neuronal excitability by releasing norepinephrine through broad projections (Swanson and Hartman, 1975; McCormick, 1992; Mircea Steriade *et al.*, 1993; Devilbiss, 2004). Given its broad projections, it is no surprise that norepinephrine is implicated in many functions such as enhancing the perception of visual and auditory stimuli (Aston-Jones *et al.*, 1994), diminishing the perception of nociceptive stimuli (Brooks *et al.*, 2017), promoting fear conditioning and fear extinction (Quirarte *et al.*, 1998; Mueller *et al.*, 2008), analgesia (Hirschberg *et al.*, 2017), pain/stress (Hickey *et al.*, 2014; McCall *et al.*, 2015), and etc. (see (Chandler *et al.*, 2019) for more). Other studies have also pointed out that activation of LC is associated with changes in brain states such as awakening and arousal (Carter *et al.*, 2010; Hayat *et al.*, 2020). It has been demonstrated that pupil diameter (as a proxy for the level of arousal) in the mouse, is highly correlated with the level of activation of the noradrenergic system (Reimer *et al.*, 2016). The broad projections from the locus coeruleus to the forebrain are generally believed to suppress slow oscillations and create an activated state (M Steriade *et al.*, 1993; Marzo, Nelson K. Totah, *et al.*, 2014; Hayat *et al.*, 2020; Sara and Bouret, 2012; Carter *et al.*, 2010). This effect is believed to be undifferentiated across the cortex due to observed highly synchronous LC spiking activity (Alvarez *et al.*, 2002; Aston-Jones and Bloom, 1981a; Aston-Jones and Bloom, 1981b; Chen and Sara, 2007; Finlayson and Marshall, 1988; Ishimatsu and Williams, 1996). However, this belief is partly shaped by the fact that most of these studies were performed when LC was activated either using electric or optogenetic stimulation. Stimulation of LC which consists of more than 1500 neurons in a volume of approximately 0.1 mm³ (Swanson, 1976; Grzanna and

Molliver, 1980), would result in an elevated firing activity in a large proportion of LC units (Noei *et al.*, 2022). Less is known about how the spatiotemporal pattern of LC spontaneous activity is shaped and how it relates to the brain state. A recent study has collected large populations of LC single units during anesthesia and has reported that spontaneous activity of LC cell pairs has sparse yet structured time-averaged cross-correlations, which is unlike the highly synchronous neuronal activity evoked by stimulation (Totah *et al.*, 2018). Having a structured cross-correlation can suggest potential LC ensembles with different spatiotemporal patterns of activity which can have different effects on cortical rhythms. This is particularly of importance, due to recent studies pointing towards more differentiated, modular and regionally-specific control of cortical areas (Uematsu *et al.*, 2017; Uematsu *et al.*, 2015; Chandler *et al.*, 2019; Chandler *et al.*, 2014; McCormick *et al.*, 2020). However, looking at pairwise time-averaged cross-correlation, cannot give us information about higher-order interactions or how the activity of ensembles resolves over time.

In our second study (Noei *et al.*, 2022) presented in the 3rd chapter, we used non-negative matrix factorization (NMF) (Lee and Seung, 1999) to analyze large populations of simultaneously recorded single units in the anesthetized rat LC to search for potential LC ensembles. NMF can detect multicell ensembles and resolve their activity over time. We aimed to correlate the activity of these ensembles to the ongoing rhythms in the PFC to test the hypothesis that spontaneous activation of distinct LC ensembles can be associated with a multitude of cortical states (Noei *et al.*, 2022) which can bring us closer to understanding how the spontaneous cortical activity is organized.

The research presented here was the result of a large multidisciplinary effort. Therefore, it is useful to specify my contribution to these studies. Data collection was performed by members of Gozzi and Totah labs, as will be specified in the chapters, I performed the analyses of electrophysiology data for the first study (Rocchi *et al.*, 2022) and the entire analyses for the second study (Noei *et al.*,

2022). The senior authors of both papers (Gozzi, Totah, Panzeri) wrote most of the text as published in the articles.

2 CHEMOGENETIC MANIPULATION OF BRAIN OSCILLATIONS

This chapter reports results published in Nature Communications in the article “Increased fMRI connectivity upon chemogenetic inhibition of the mouse prefrontal cortex” (Rocchi *et al.*, 2022), or which I was listed as 3rd author with equal 1st author contribution. This study is the result of a large multidisciplinary effort. In this work, members of the Gozzi lab (mostly Federico Rocchi) performed the experiments and collected the data. I performed the analyses of the electrophysiological data. Alessandro Gozzi wrote the text with Stefano Panzeri. We refer to the Author Contribution Section of that paper for full details. For completeness and ease of reading and to produce a full context, the purpose of cohesion in reading, the entire paper is included in this chapter.

2.1 Introduction

A rapidly expanding approach to understand the functional organization of brain networks is to map large-scale patterns of spontaneous activity via non-invasive neuroimaging. The ease and reproducibility of “resting state” fMRI (rsfMRI) have promoted the widespread use of this approach, leading to the observation that spontaneous fMRI activity is organized into highly coherent functional networks, defined by temporally correlated fluctuations in BOLD signal (Power *et al.*, 2014). The non-invasive nature of rsfMRI has fueled the use of this method to map intrinsic brain network organization in the healthy human brain, as well as in psychiatric or neurological conditions, in which evidence of disrupted or aberrant rsfMRI functional coupling has been largely documented (Power *et al.*, 2014). However, despite the growing popularity of rsfMRI, our knowledge of the underpinnings of brain-wide fMRI coupling remains very limited.

Multiple lines of evidence suggest that structural and rsfMRI-based connectivity are robustly related (Power *et al.*, 2014). First, structural and functional connection strengths are correlated both at the whole-brain and mesoscopic scale (Coletta *et al.*, 2020; Hagmann *et al.*, 2008; Wang *et al.*, 2013), and rsfMRI network topography closely recapitulates patterns of anatomical connectivity in several mammalian species (Coletta *et al.*, 2020; Goñi *et al.*, 2014; Honey *et al.*, 2009). Second, experimental resection of callosal connections (O'Reilly *et al.*, 2013) or chemogenetic inactivation of the amygdala result in reduced rsfMRI connectivity with regions anatomically linked to the manipulated area (Grayson *et al.*, 2016). Lastly, computational modeling corroborates a tight relationship between structural and functional connectivity, as synchronous rsfMRI fluctuations can be modeled by dynamical systems endowed with realistic anatomical connectivity patterns of long-range axonal interactions (Ponce-Alvarez *et al.*, 2015). Accordingly, simulated axonal lesions in these models result in reduced functional coupling (Alstott *et al.*, 2009).

These observations have prompted the widespread use of statistical dependencies in spontaneous fMRI signal as an index of interareal functional communication (Power *et al.*, 2014). However, the neural mechanisms linking regional brain activity to large-scale rsfMRI network connectivity remain unclear. For example, growing experimental evidence suggests that, while tightly constrained by underlying anatomy, rsfMRI connectivity may only partially reflect direct interactions between areas, as widespread BOLD signal modulation might arise via subcortical connections, whether through the thalamus via long-range loops (Gent *et al.*, 2018), or as a result of diffuse neuromodulation mediated by brainstem nuclei (Liu *et al.*, 2018; Munn *et al.*, 2021). This notion is epitomized by the observation of intact rsfMRI coupling among brain regions not directly structurally connected as in the case of acallosal humans, primates, and rodents (O'Reilly *et al.*, 2013; Sforazzini *et al.*, 2016; Tyszka *et al.*, 2011). Moreover, rsfMRI network topography can dynamically reconfigure in response to local perturbations (Eldaief *et al.*, 2011) or pathological processes (Pagani *et al.*, 2021). In keeping with this,

neurological disorders such as Parkinson's disease, stroke, and Alzheimer's disease have been often found to be associated with unexpectedly increased interareal rsfMRI connectivity despite the loss of cortical function characterizing these conditions (Hillary and Grafman, 2017; Siegel *et al.*, 2016). Taken together, these observations point at a complex relationship between interareal brain activity and rsfMRI coupling, and call for a deeper investigation of the neural mechanisms underlying the reconfiguration of rsfMRI connectivity in response to varying interareal input or pathological perturbations.

Here we combine rsfMRI, neural and chemogenetic inhibition (chemo-fMRI (Giorgi *et al.*, 2017)), and in vivo electrophysiology in the mouse to probe how inactivation of a cortical area causally affects rsfMRI coupling. Surprisingly, we find that chronic and acute inhibition of the medial prefrontal cortex (PFC), a core component of the mouse default mode network (DMN, (Whitesell *et al.*, 2021)), can increase rsfMRI coupling with its thalamo-cortical targets. This effect is associated with decreased γ power in the suppressed region and robustly increased low frequency (0.1-4 Hz) electrophysiological coherence between functionally overconnected PFC targets. These findings reveal a highly dynamic, non-monotonic relationship between regional cortical activity and network-wide rsfMRI connectivity, and provide an interpretative framework for the observation of counterintuitively increased rsfMRI connectivity in pathological conditions characterized by impaired cortical function.

2.2 Methods

2.2.1 Ethical statement

All in vivo experiments were conducted in accordance with the Italian law (DL 26/214, EU 63/2010, Ministero della Sanità, Roma). Animal research protocols were reviewed and consented by the animal care committee of the University of Trento and Italian Ministry of Health (authorization no. 852/17 to A.G.). All surgical procedures were performed under anesthesia.

2.2.2 Animals

Adult (6-week-old) male C57Bl6/J mice, and transgenic animals expressing Cre recombinase in parvalbumin-positive GABAergic neurons (B6.129P2-Pvalbtm1(cre)Arbr/J, (Cardin *et al.*, 2009) were bred in house. Mice were housed with temperature maintained at $21 \pm 1^\circ\text{C}$ and humidity at $60 \pm 10\%$.

2.2.3 Anatomical definition of mouse medial prefrontal cortex

Our anatomical definition of mouse medial prefrontal cortex (PFC) reflects recent neuroanatomical (Carlén, 2017) and cytoarchitectural cross-species comparisons (Vogt and Paxinos, 2014), according to which the mouse PFC comprises a prelimbic region, corresponding to primate Brodmann area 32 (A32), the anterior cingulate cortex, corresponding to Brodmann area A24b, and the infralimbic cortex, corresponding to Brodmann area A24a. Our viral manipulations were therefore aimed to inhibit an anatomical ensemble comprising all the above-mentioned regions at the following coordinates, expressed in millimeter from Bregma: 1.7 from anterior to posterior, ± 0.3 lateral, -1.7 deep (Paxinos and Watson, 2017).

2.2.4 Viral injections

Mice were anesthetized with isoflurane and head-fixed in a stereotaxic apparatus (Stoelting). Injections were performed with a Hamilton syringe mounted on Nanoliter Syringe Pump with controller (KD Scientific), at a speed of 0.05 $\mu\text{L}/\text{min}$, followed by a 5–10 min waiting period, to avoid backflow of viral solution. To prevent layer- or cell-type specific expression (Nathanson *et al.*, 2009), all in vivo viral transductions were carried out using high-titer ($> 10^{13}$ vg/mL) viral suspensions. The following injections volumes were employed: 300 nL (AAV8-hSyn-hM4D(Gi)-mCherry and AAV8-hSyn-GFP; <http://www.addgene.org>) or 2 μL (AAV8-hSyn-MYC-mKir2.1(E224G/Y242F)-IRES-GFP, Xue *et al.* 2004, <http://www.vectorbiolabs.com> or AAV8-hSyn-GFP <http://www.addgene.org>), or 1 μL (AAV8-CamkII-hM3D(Gq)-mCherry; <http://www.addgene.org>) or 300 nL (AAV9-hSyn-DIO-hM4D(Gi)-mCherry; <http://www.addgene.org>) of viral

suspension were injected bilaterally in the mouse PFC (see coordinates above). Control groups for both CamkII-hM3D(Gq) and PV-hM4D(Gi) were obtained by sham-injecting genotype-matched littermates. rsfMRI or electrophysiological recordings were carried out no sooner than three weeks after the injection to allow for maximal viral expression.

2.2.5 rsfMRI acquisitions

The animal preparation protocol was recently described in detail (Ferrari *et al.*, 2012; Gutierrez-Barragan *et al.*, 2019; Sforazzini *et al.*, 2014). Briefly, mice were anesthetized with isoflurane (5%, induction), intubated and artificially ventilated (2%, surgery). The left femoral artery was cannulated for continuous blood pressure monitoring. At the end of surgery, isoflurane was discontinued and substituted with a shallow halothane regimen (0.75%) to obtain light sedation and to preserve cerebral blood flow auto-regulation (Gozzi *et al.*, 2007). Ventilation parameters were adjusted to maintain normo-physiological paCO_2 (< 40 mmHg) and paO_2 levels (> 90 mmHg, corresponding to $>98\%$ hemoglobin saturation). To probe the generalizability of our findings, we also repeated our inhibitory chemo-fMRI manipulations under a combination of medetomidine and low-dose isoflurane (0.05 mg/kg bolus and 0.1 mg/kg/h IV infusion, plus 0.5% isoflurane, (Grandjean *et al.*, 2020; Lee *et al.*, 2021).

rsfMRI data acquisition commenced 30 min after isoflurane cessation. Functional images were acquired with a 7T MRI scanner (Bruker, Ettlingen) equipped with a BGA-9 gradient set (380 mT/m, max. linear slew rate 3,420 T/m/s) as previously described (Liska *et al.*, 2015), using a 72 mm birdcage transmit coil and a 4-channel solenoid coil for signal reception. Single-shot BOLD rsfMRI time series were acquired using an EPI sequence with the following parameters: TR/TE 1000/15 ms, flip angle 60° , matrix 98×98 , FOV 2.3×2.3 cm, 18 coronal slices, slice thickness $550 \mu\text{m}$, bandwidth 250 KHz. rsfMRI acquisition with Kir2.1-transduced (AAV8-hSyn-MYC-mKir2.1(E224G/Y242F)-IRES-GFP, $n = 16$) and control mice (AAV8-hSyn-

GFP, $n = 19$) encompassed 35-minute long timeseries, corresponding to 2100 volumes.

Chemo-fMRI acquisitions comprised two consecutive rsfMRI timeseries, encompassing 1800 volumes (30 min) and 2100 volumes (35 min), respectively. CNO (2 mg/kg, Sigma Aldrich) was injected intravenously fifteen minutes (volume #900) after the start of the first scan. The first 900 fMRI volumes of this first timeseries scan were used as pre-CNO baseline rsfMRI reference in time-resolved analyses. Based on the pharmacokinetic profile of CNO, the post CNO window was split into temporal domains as follows: the first 15 min post injection (900 volumes) were considered part of a drug equilibration window, while the following 35 min (2100 volumes) were considered to cover the DREADD active time window (Trakoshis *et al.*, 2020). All group comparisons in the chemo-fMRI study were carried out within this latter time window, unless otherwise stated. After post-mortem analyses of viral expressions, a total of $n = 15$ hM4Di and $n = 19$ GFP-transduced animals were retained for analyses.

2.2.6 Image preprocessing and analysis

Raw rsfMRI timeseries were preprocessed as described in previous work (Gutierrez-Barragan *et al.*, 2019; Sforazzini *et al.*, 2014). Briefly, the initial 120 volumes of the time series were removed to allow for thermal gradient equilibration. Data were then despiked, motion corrected, and spatially registered to a common reference template. Motion traces of head realignment parameters (3 translations + 3 rotations) and mean ventricular signal (corresponding to the averaged BOLD signal within a reference ventricular mask) were used as nuisance covariates and regressed out from each time course. All rsfMRI time series also underwent band - pass filtering within a frequency window of 0.01 - 0.1 Hz (halothane) or 0.01-0.25 Hz (MED-ISO, (Grandjean *et al.*, 2020)) followed by spatial smoothing with a full width at half maximum of 0.6 mm. To control for the effects of global fMRI signal regression on the mapped changes, all rsfMRI timeseries were also recomputed by after global signal regression. Global signal

regression was performed to remove the global signal from each voxel using a linear regression. Global signal was calculated by taking the average of the signal over all voxels within an intracerebral mask at each time point. Global signal regression is believed to reduce some global motion and respiration artifacts (Li *et al.*, 2019).

rsfMRI connectivity of the mouse DMN in Kir2.1 and chemo-fMRI scans was probed using a seed-based approach. In the case of the chemo-fMRI study, this quantification was carried out during the CNO active time window. A 5x5x2 seed region was selected to cover the PFC areas targeted by viral injections. Voxel - wise intergroup differences in seed-based mapping were assessed using a 2 - tailed Student's t test ($|t| > 2$, $p < 0.05$) and family - wise error (FWE) cluster - corrected using a cluster threshold of $p = 0.05$ as implemented in FSL (<https://fsl.fmrib.ox.ac.uk/fsl/>). The antero - posterior connectivity profile of the DMN was assessed by computing Person correlation between the PFC seed abovementioned and a series of 6 x 6 x 2 voxel seeds placed along the midline extension of the cingulate and retrosplenial cortices as previously described (Pagani *et al.*, 2019). Quantification of cortico-thalamic connectivity was carried out with respect to a meta-regional parcellation of the mouse cortex in volumes-of-interest. To rule out a possible confounding contribution of spurious neurovascular changes in CNO-induced rsfMRI connectivity alterations, we calculated and statistically compared the characteristic hemodynamic response function between Kir2.1 and control mice, and between hM4Di-expressing and control mice upon CNO-administration (active phase), as previously described in (Pagani *et al.*, 2019; Wu *et al.*, 2013).

Whole-brain connectivity in hM4Di and Control mice was calculated across a set of volumes of interest recapitulating anatomical areas of the Allen brain atlas. The anatomical probed area were selected according to their coverage of previously characterized network systems of the mouse brain (Liska *et al.*, 2015; Sforazzini *et al.*, 2014; Whitesell *et al.*, 2021): TH: thalamus (thalamus polymodal association cortex related, Thalamus Sensory-Motor cortex related); STR: striatum (Striatum

dorsal region left, striatum dorsal region right, striatum ventral region left, striatum ventral region right); LCN: lateral cortical network (LCN: primary motor cortex left, primary motor cortex right, primary somatosensory cortex left, primary somatosensory cortex right, secondary somatosensory cortex left, secondary somatosensory cortex right, Lateral septal complex left, lateral septal complex right); HCP: hippocampus (Ammon's horn left; Ammon's horn right, dentate gyrus left; dentate gyrus right, Entorhinal area left, entorhinal area right, subiculum left, subiculum right); DMN: default mode network (anterior cingulate area; Infralimbic area, secondary motor cortex left, secondary motor cortex right, orbital area, prelimbic area, posterior parietal association areas left, Posterior parietal association areas right, retrosplenial area).

To relate the strength of underlying anatomical connectivity to the regions exhibiting increased rsfMRI connectivity with voxel resolution, we extracted outgoing projections from the affected PFC regions using a spatially-resampled (0.027 mm³) version of a voxel scale model of the Allen Brain Institute structural connectome (Coletta *et al.*, 2020). We then plotted the strength of PFC-departing structural projections against the corresponding between-group difference in rsfMRI connectivity using the cluster-corrected difference map and assessed differences in the distribution of overconnected areas with respect to all the brain voxels using a Wilcoxon rank-sum test.

To quantify the contribution of distinct thalamic subregions to overall group differences, we used k-means clustering to partition voxels within the thalamus, based on whole-brain rsfMRI group-difference obtained using the PFC seed as recently described (Schleifer *et al.*, 2019; Arthur and Vassilvitskii, 2007). This approach revealed two major thalamic clusters, one medial and one bilateral partition encompassing sensory areas. Seed-based functional connectivity was subsequently computed for each of the two-resultant k-means clusters independently, and the resulting functional connectivity maps were compared and quantified across cortical VOIs.

2.2.7 Electrophysiological recordings

Electrophysiological recordings were carried out in animals subjected to the same animal preparation and sedation regime employed for rsfMRI mapping (Ferrari *et al.*, 2012; Sforazzini *et al.*, 2014). Briefly, mice were anesthetized with isoflurane (5% induction), intubated, artificially ventilated (2% maintenance), and head-fixed in a stereotaxic apparatus (Stoelting). The tail vein was cannulated for CNO injection. To ensure maximal consistency between viral injections and recording site, the skull surface was exposed and an insertion hole in the right PFC was gently drilled through the skull corresponding to the location of prior viral injection point. A single shank electrode (Neuronexus, USA, interelectrode spacing 1 - 2.5 mm) was next inserted through the overlying dura mater by a microdrive array system (Kopf Instruments, Germany) at an insertion rate of 1 $\mu\text{m}/\text{min}$ to reach the same stereotaxic coordinates employed for viral injection. The site receptive fields were plotted manually and the position and size of each field were stored together with the acquisition data. After electrode insertion, isoflurane was discontinued and replaced by halothane at a maintenance level of 0.75% to induce rsfMRI-comparable sedation. Electrophysiological data acquisition commenced 1 hour after isoflurane cessation. Such transition time was required to ensure complete washout of isoflurane anesthesia and avoid residual burst-suppressing activity associated with extended exposure to deep anesthetic levels.

Neural activity was next recorded in consecutive 5 min time bins to cover a 15 min pre-injection time window, and a 60 min post CNO timeframe in $n = 5$ hM4Di and $n = 5$ GFP-expressing mice. Signals were amplified using an RHD 2000 amplifier system (Intan Technologies) at a sampling rate of 20 kHz. For CamkII-hM3D(Gq) ($n = 4$) and PV-hM4D(Gi) ($n = 6$) experiments we acquired respectively $n = 4$ and $n = 7$ control animals. In the case of control Kir2.1 recordings, a four shank electrode was inserted along the coronal plane to bi-hemispherically cover the right (Kir2.1-expressing) and left (GFP-expressing) PFC ($n = 4$). The left region served as internal reference control to better assess the efficacy of Kir2.1 neural inhibition.

Electrophysiological signals were then recorded into 5 min time bins to cover a 35 min time-window.

To measure multi-electrode coherence, three electrodes were inserted in key cortical and subcortical substrates identified as overconnected in our chemo-fMRI mapping in $n = 4$ hM4Di and $n = 5$ GFP-expressing mice. A multi-probe micromanipulator (New-Scale Technologies) was used to insert three 16 channels single shank electrode (Neuronexus, USA, interelectrode spacing 1 - 2.5 mm) in the right prefrontal cortex, centromedial thalamus and retrosplenial cortex, respectively. Representative electrode locations are reported in Figure 3.1, corresponding to the following stereotaxic coordinates: PFC 1.7 mm AP, ± 0.3 mm ML, -1.7 mm DV; mediodorsal thalamus: -1.7 mm AP, -0.3 mm ML, -3.5mm DV (5° insertion angle); retrosplenial cortex: -2.4 mm AP, -0.3 mm ML, -1.3 mm DV. To reduce tissue damage, an insertion rate $< 1 \mu\text{m}/\text{min}$ was employed, allowing for a 30-minute equilibration every 400 μm traveled. Ground electrodes were put in contact with the cerebral brain fluid through a window drilled in the skull. Signals were then recorded into 1 min time bins to cover a 15-min pre-injection baseline and a 40-min post CNO time window.

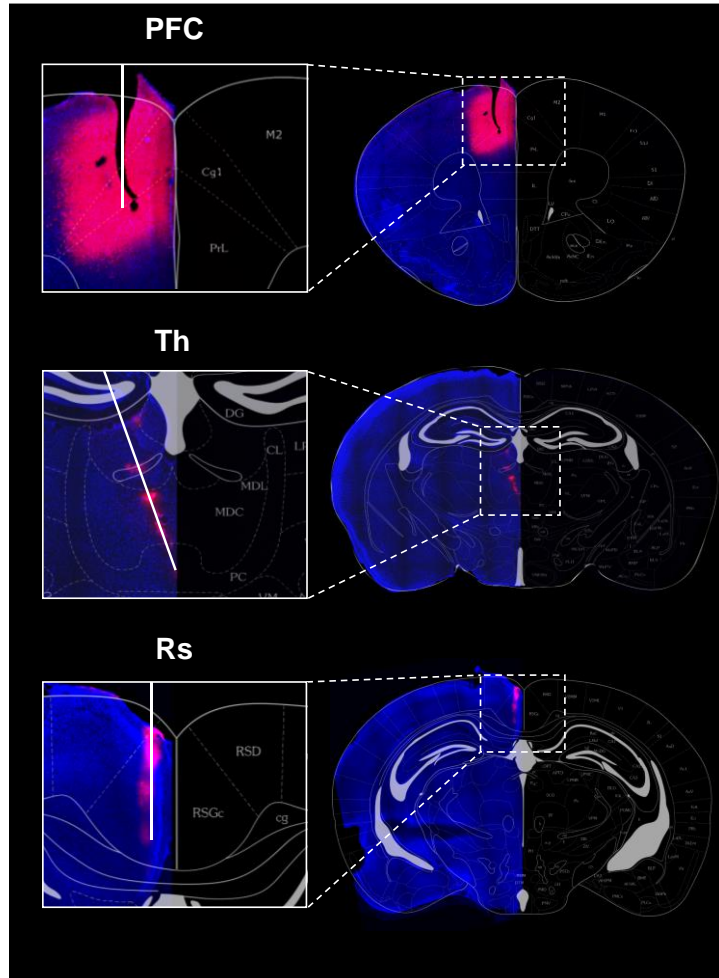


Figure 2.1 Histological validation of electrode placement. Electrode insertion traces (Th and Rs, red, lipophilic dye Dil) are here highlighted with a white line to indicate approximate electrode profile and insertion angle. In the PFC, red signal represents hSyn-hM4Di viral expression, and area of electrode insertion is indicated by the corresponding mechanically-induced lesion produced before electrode removal at the end of recording session. Individual color channels have been adjusted to increase contrast. PFC: medial prefrontal cortex; Th: thalamus; Rs: retrosplenial cortex.

LFP and multi-unit activity (MUA). To compute the LFP signal, raw extracellular recordings were first down-sampled to 4 kHz, then band-pass filtered to 1-250 Hz using a previously published two-step procedure (Belitski *et al.*, 2008). Briefly, raw timeseries were first low-pass filtered using a 4th order Butterworth filter with a cut-off frequency of 1 kHz. The resulting timeseries were next down-sampled to 2 kHz, then again filtered using a Kaiser window filter between 1Hz to 250Hz (with a sharp transition bandwidth of 1Hz, passband ripple of 0.01 dB and a stop band attenuation of 60 dB) and then resampled at 1 kHz. All the filtering was applied

both in forward and backward temporal direction to avoid any phase transitions due to filtering.

To compute multi-unity activity (MUA) we again followed the procedure described in (Belitski *et al.*, 2008). Briefly, we computed a band-passed high-frequency signal using a 4th order Butterworth filter with a <100 Hz cut off frequency, then band-pass filtered between 400 and 3000 Hz using a Kaiser window filter (with transition band of 50 Hz, stopband attenuation of 60 dB, and passband ripple of 0.01 dB). From the high frequency signal we detected spike times using a spike detection threshold corresponding to 4-times the median of the high frequency signal, then divided by 0.6745 as suggested in (Quiroga *et al.*, 2004). Spikes were considered to be biologically plausible, and as such retained in these computations, only if occurring more than 1 ms apart.

To determine the time lag at which different firing rate samples from the same channels could be considered as approximately statistically independent, we computed for each subject the autocorrelation of the channel-averaged firing rate for each subject and computed the time lag after which the autocorrelation function drops below the 95th percentile. We then, for each subject, retained samples of the baseline-normalized firing rate at different times separated by the above obtained lags. We next separately analyzed the baseline-normalized rates in three different periods: 0 to 15 minutes (transient time), 15 to 35 minutes, and 35 to 55 minutes after CNO the injection (active time). We pooled all the retained data points in these windows both over time and over subjects and then compared the median between the two populations using a two-sided Wilcoxon rank-sum test. The obtained p-values were corrected using a Benjamini-Hochberg FDR correction.

LFP spectrograms were computed using a Fourier transform with a Kaiser window with a frequency resolution of 0.15 Hz, temporal resolution of 6 seconds, and with 50% overlapping windows. Spectrograms and their differences were smoothed in time with the resolution of 30 seconds, and in frequency with the resolution of 1Hz using a median filter. To quantify the effect of CNO on LFP rhythms, we

computed a spectrogram modulation index as follows. First, we computed the channel-averaged spectrograms for the duration of the baseline recording. Next, we averaged time-frequency spectral profiles over time, resulting in frequency-resolved spectral profiles. The effect of CNO was next assessed by computing a modulation index, defined as the ratio of channel-averaged spectrogram after injection minus baseline, time-averaged spectrogram, and the sum of the same quantities, for every time window and for every frequency. This modulation index ranges between -1 and 1 and describes the changes due to drug injection over time for each frequency.

To obtain a statistical assessment of CNO effects across groups and bands, we computed the autocorrelation of spectrograms for every subject at every frequency, using (as for our assessment of firing rate) only spectrograms computed at time points far enough to be approximately statistically independent. The time lag to determine such approximately independent points was identified as the interval after which the spectrum's autocorrelation function dropped below the 95th percentile. We next computed the median of the modulation index over different frequency bands defined as follows: slow (0.1-1 Hz), δ (1-4 Hz), θ (4-8 Hz), α (8-12 Hz), β (12-30 Hz) and γ (30-70 Hz). Data within each band were pooled over uncorrelated time points (determined as above by taking time samples separated by lags at which autocorrelation became negligible) and over subjects, and the population medians were compared using two-sided Wilcoxon rank-sum tests, followed by FDR correction.

2.2.8 Multielectrode coherence

Channel averaged spectrograms were preprocessed as described above. Raw spectral power coherence was assessed by computing the magnitude of squared coherency using Welch's overlapped averaged periodogram method (Welch, 1967) with a 50% overlapping window of 2 seconds length. Coherence was calculated for every 60-second bin of channel-averaged recordings. Temporal smoothing was carried out using a 60-second median filter as described above.

CNO spectrograms (30-40 post CNO injection window) were normalized with respect to the last 3 minutes of pre-CNO baseline using a modulation index as before. To obtain a quantifiable assessment of the CNO effect across different groups and bands, data within each band were pooled into 60-second bins. Subject and the population medians were compared for each region separately using one-sided Wilcoxon rank-sum tests, followed by FDR correction. The use of 60 second bins was motivated by estimations of the time lags at which autocorrelation of electrophysiological signals drops below the 95th percentile value (and thus samples are approximately independent) as described above.

To assess changes in ultra-slow fluctuations in the γ band envelope of LFP, following the work from (Nir *et al.*, 2008), we computed LFP data spectrogram for the last 10 minutes of baseline and 30 to 40 minutes of post injection window, using a moving window of 2 seconds width and 0.75 percent overlap, resulting in an estimation of the resulting ultra-slow power for each 0.5 second interval. The γ -band envelope was computed as the integrated power of the spectrograms in the γ band (30-70 Hz), following previously published procedures (Mateo *et al.*, 2017). The power spectrum of this time series was next computed, after correction for 1/f component (Mateo *et al.*, 2017), revealing a peak in the 0.02-0.05 Hz region. Interareal coherence was then computed as described above for both experimental and control mice. To assess the effect of chemogenetic manipulations, we defined a coherence modulation index as described above for other frequency bands. Between group statistical assessments were carried out using two - sided Wilcoxon rank - sum tests, followed by FDR correction.

To quantify interregional phase coupling, LFP data were first filtered using a third order Butterworth filter in delta band, and the instantaneous phase of each channel was computed by taking the phase of the analytical signal resulted from the Hilbert transform. For all possible pairs of channels belonging to two different regions, we next computed the corresponding Phase Locking Value (PLV) as follows:

$$PLV = \frac{1}{N} \left| \sum_{j=1}^N e^{i(\theta_{ch1}(t_j) - \theta_{ch2}(t_j))} \right|$$

Where N is the number of data points in time and $\theta_{ch1}(t_j), \theta_{ch2}(t_j)$ are the instantaneous phase of the LFP of channel 1 and 2 at time j . The PLV value for each pair during the 30 to 40 minutes post CNO was next normalized with respect to the PLV value of the last 3 minutes of the pre-CNO baseline using a modulation index and was pooled over channel pairs and animals. The obtained population medians of the control and experimental group for each region pair were next compared using two-sided Wilcoxon rank-sum tests, followed by FDR correction.

2.2.9 Power spectrum of simulated spiking activity

To understand whether the increase in δ and slow LFP power observed with DREADD-induced inhibition could be explained by selective elimination of spikes not occurring at the preferred, most excitable, phase of the considered oscillation, we simulated 10 seconds epochs of spikes locked to a cosine “LFP” wave oscillating at 1 Hz. In the first scenario, representing the DREADD conditions, we generated 100 spikes (rate of 10 spikes per second) tightly distributed around the preferred phase π with values taken from a von Mises distribution with an extremely high value (20) of the concentration parameter. For the second case (representing sham condition), we added 100 more spikes distributed almost randomly across phases, with values taken from a von Mises distribution with an extremely low value (0.5) of the concentration parameter. We then smoothed spike temporal components with a Gaussian kernel (100 ms width) and computed the power spectra of the resulting spike train with the multitaper method (Matlab `pspectrum` function).

2.2.10 Relationships between spikes and LFP phases

We computed at each time point the phase of the LFP in a given frequency band as the angle of the Hilbert transform of the band passed LFP. We considered for this analysis the slow and δ bands. Signal in each band was band-passed using a

3rd order Butterworth filter. To measure the locking of spikes to specific phases of each band, we considered the distribution of the LFP phase values at the time of each MUA spike. From this distribution, we computed the phase locking value (PLV) as 1 minus the circular variance of this distribution (Methods Section “Multielectrode coherence”). PLV ranges from 0 (no locking or relationship between phase and spike times) to 1 (perfect locking of spikes to a certain phase). As for other quantities, we also computed a PLV modulation index as the difference of PLV values between the active-drug and baseline periods divided by the sum of PLV values in the active-drug and baseline periods. A two-sided Wilcoxon was used to check if the median PLV modulation index is higher for the experimental data with respect to control data.

Violin plot representations of all electrophysiological analyses include individual statistically-independent points (see above) used for intergroup comparisons. Plots were generated using Prism Graphpad 9.1. Plot truncation at extremities is introduced by the software to avoid representation of kernel density-related fictitious values above the highest data value or below the smallest.

2.2.11 LFP-LFP phase differences

To characterize the phase differences across areas, we computed the distribution across time of the difference in the instantaneous phase (computed as explained above) of PFC and Rs electrode pairs. From this distribution, we considered a channel pair to have significant PLV (see “Multielectrode coherence” section above) if its PLV value exceeded the 95th percentile of surrogate PLV distribution obtained by shuffling LFPs in time prior to filtering, and if the same PLV value was also greater than 0.1. We report in Figure 2.17 the distribution of preferred phase differences (the circular mean of the phase difference distribution) for these significant channels. In the same figure, we also report (as thick lines) the values of the circular mean across all significant channels in each condition. We here report only the results of retrosplenial and PFC electrode pairs in the δ band, because this was the only combination exhibiting very stable mean circular phases

across all baseline conditions and during the active time of the control injection. Circular and statistics were all computed with CircStat package (Berens, 2009).

2.3 Results

2.3.1 rsfMRI overconnectivity upon chronic inactivation of the mouse prefrontal cortex

The robust structural foundations of rsfMRI connectivity suggest that neural inhibition of a network node would result in diminished functional coupling with regions receiving direct axonal projections from the inactivated region (Alstott *et al.*, 2009; Grayson *et al.*, 2016; Suárez *et al.*, 2020). To test this prediction and more broadly investigate how rsfMRI dynamically reconfigures in response to local neural suppression, we carried out rsfMRI measurements in a cohort of mice in which neuronal activity in PFC was chronically inhibited via bilateral viral transduction of the inward rectifying potassium channel Kir2.1 (Figure 2.2a). Our interest in the PFC was motivated by its translational relevance as a key component of the mouse default mode network (DMN), a major phylogenetically conserved rsfMRI network that in rodents is composed by three hubs, namely the PFC, the retrosplenial cortex and the medial thalamus (Coletta *et al.*, 2020; Whitesell *et al.*, 2021). Prior research in awake animals has shown that virally - mediated Kir2.1 expression results in a reduction of both evoked and spontaneous neuronal excitability lasting several weeks (Beier *et al.*, 2017; Xue *et al.*, 2014). In keeping with this, in vivo electrophysiological recordings in the PFC of mice unilaterally transfected with Kir2.1 revealed a robust reduction of spontaneous firing rate in the targeted cortical area with respect to its contralateral control regions (N = 4, paired t test, $p = 0.002$, Figure 2.3).

We next compared the patterns of rsfMRI connectivity in Kir2.1 and GFP-transduced control littermates by imaging Kir2.1 transfected mice four weeks after viral injections (Figure 2.2a). Consistent with previous investigations (Bertero *et*

al., 2018; Pagani *et al.*, 2019), seed-based probing revealed significant long-range correlation between the PFC and thalamo-cortical components of the mouse DMN in both cohorts (Figure 2.2b). Surprisingly, between-group comparisons revealed foci of significantly increased rsfMRI connectivity in the posterior cingulate/retrosplenial cortex and centromedial thalamic regions of Kir2.1 transfected mice (t test, $p < 0.05$, $t > 2.03$, FWE cluster-corrected, $p < 0.05$; Figure 2.2c). Regional quantifications of DMN connectivity via multiple prefrontal-DMN seeds corroborated these findings, revealing increased rsfMRI synchronization along the entire midline extension of this network (two-way repeated measures ANOVA, $F_{1,33} = 6.93$; $p = 0.013$; Figure 2.2d) and its centromedial thalamic targets (t test, $t_{33} = 2.589$, $p = 0.014$; Figure 2.2e). Voxel-wise mapping did not reveal any foci of reduced functional connectivity with the PFC ($t > 2.03$, FWE cluster-corrected, $p < 0.05$). Importantly, all the thalamic and cortical regions showing increased rsfMRI connectivity in Kir2.1 mice are characterized by high axonal projection density from the PFC, as seen by comparing the magnitude of inter-group rsfMRI connectivity differences with incoming axonal connectivity strength inferred from a voxel-model of the mouse brain connectome (Coletta *et al.*, 2020) (Figure 2.2f, Wilcoxon rank-sum test, $p < 0.0001$). Interestingly, the direction and anatomical location of DMN rsfMRI overconnectivity was not altered by global fMRI signal regression (Figure 2.4), with the exception of thalamic areas, in which the connectivity difference between groups was attenuated. Together, these findings reveal that chronic inhibition of neural activity in the PFC may counterintuitively increase rsfMRI functional connectivity between long-range thalamo-cortical targets of the mouse DMN.

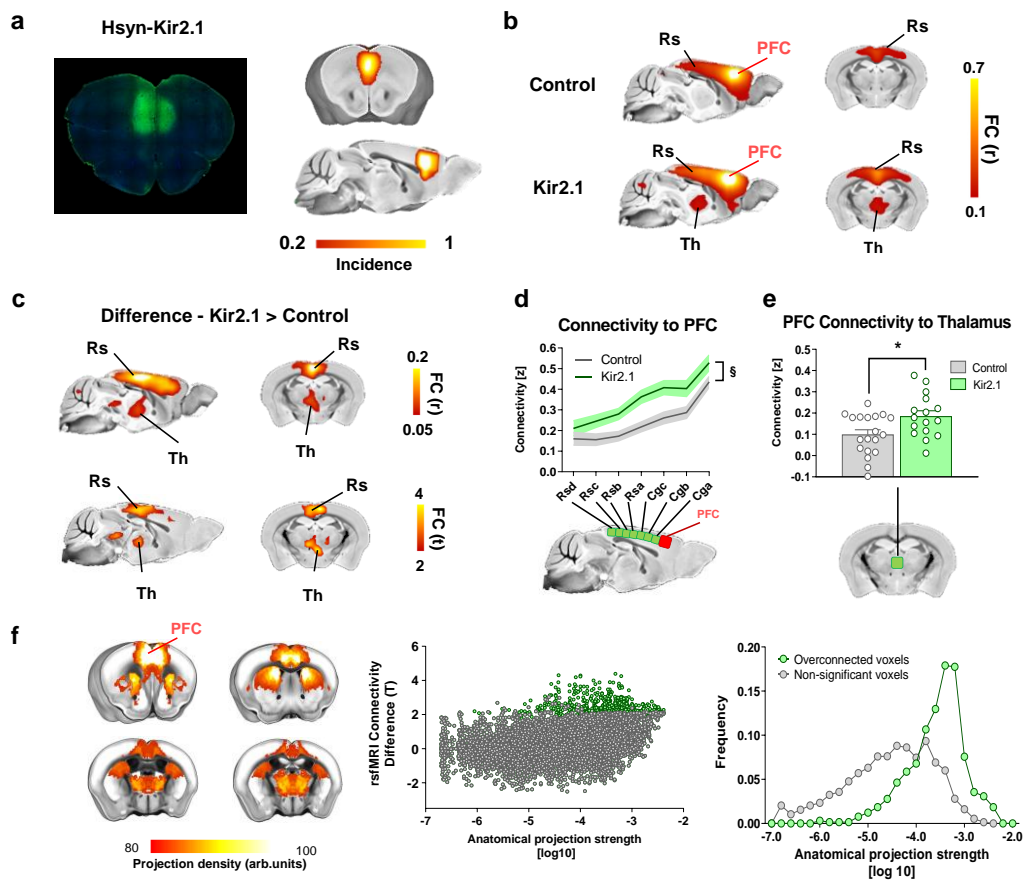


Figure 2.2 Chronic inhibition of the mouse PFC results in rsfMRI overconnectivity. (a) Viral expression localization. The potassium channel Kir2.1 ($n = 16$) or GFP (control, $n = 19$) were transduced bilaterally into the PFC of adult male mice. Left: Representative histology sample shown Kir2.1 (green). Right: Heatmaps illustrate a qualitative regional assessment of viral expression across subjects. (b) Seed based connectivity mapping of the PFC in GFP (control), and Kir2.1-transduced subjects. (c) Corresponding group difference maps. Area exhibiting significantly increased rsfMRI connectivity in Kir2.1 expressing mice are depicted in red-yellow (r and T stat difference map). (d) Antero-posterior profiling of rsfMRI connectivity of the PFC within the midline axis of the mouse DMN ($\$ p = 0.014$, two-way ANOVA with repeated measurements, genotype effect, $n = 16$ and $n = 19$ Kir2.1 or GFP-expressing mice, respectively). (e) Fronto-thalamic rsfMRI overconnectivity in Kir2.1 expressing mice ($*p = 0.014$, two-sided t test, $n = 16$ and $n = 19$ Kir2.1 or GFP-expressing mice, respectively). Data in (e) and (f) are presented as mean values \pm SEM. (f) Regions exhibiting rsfMRI overconnectivity in Kir2.1 mice are robustly innervated by the PFC. Left: Axonal projections from the PFC (top 20% strongest connections). Middle: scatter plot illustrating intergroup differences in rsfMRI connectivity as a function of PFC structural connectivity strength. Green dots indicate significantly functionally overconnected voxels. Right: Distribution of overconnected voxels as a function of axonal connectivity strength Green. FC: functional connectivity; DMN: Default Mode Network; Cg: cingulate cortex; PFC: prefrontal cortex, RS: retrosplenial; Th: Thalamus

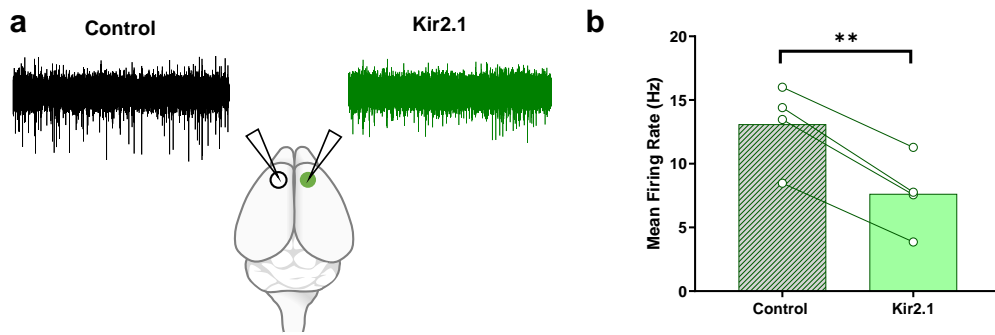


Figure 2.3 Overexpression of the potassium channel Kir2.1 in the PFC reduces spontaneous neural activity. (a) Experimental design: Kir2.1 injection was performed unilaterally in the right PFC. A viral vector encoding GFP was injected in the contralateral area. Electrophysiological recordings were carried out bilaterally using a four-shank electrode. (b) Mean spontaneous firing rate for the control side (no Kir2.1 expression), and the side expressing Kir2.1. (n=4; ** p = 0.002, two-sided paired t-test).

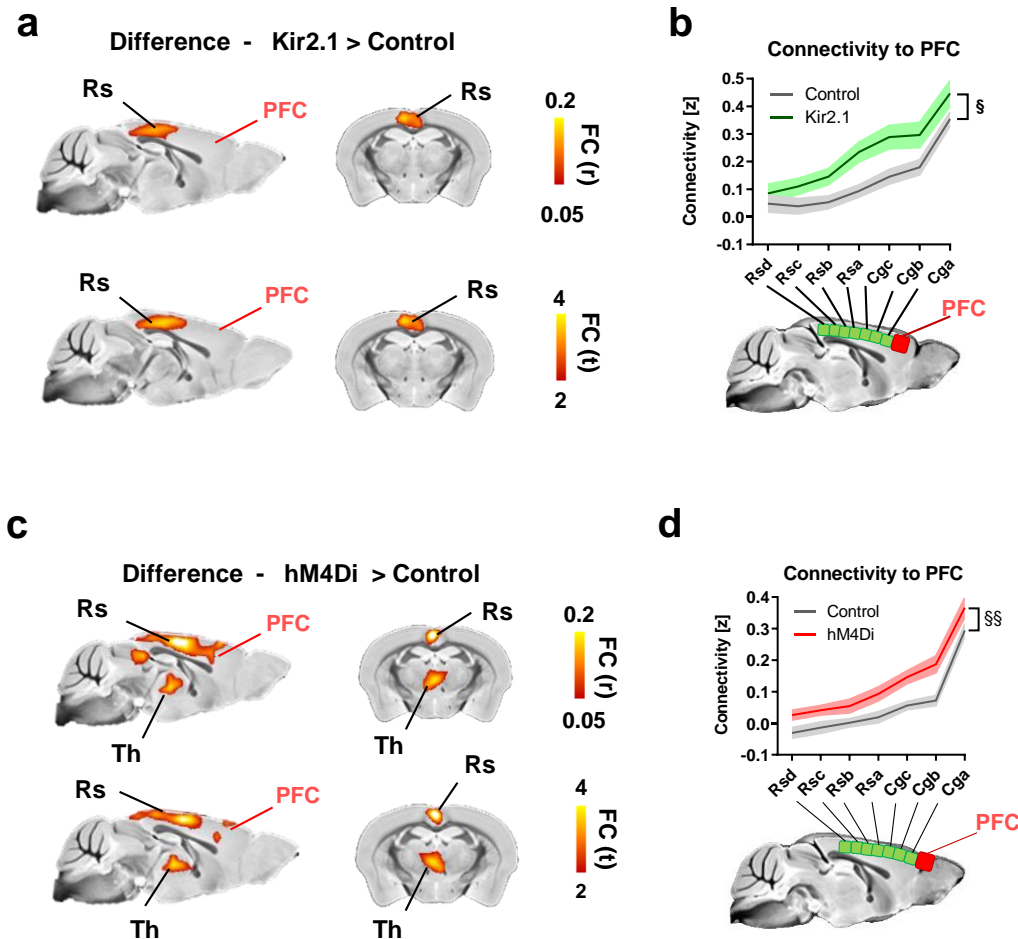


Figure 2.4 rsfMRI overconnectivity in Kir2.1 and DREADD-expressing mice persists after global fMRI signal regression. (a) Between-group difference maps (Pearson's r, and corresponding T stat difference maps). rsfMRI connectivity was here computed after fMRI global signal regressions. (b) Antero-posterior profiling of rsfMRI connectivity of the PFC along the midline axis of the mouse

DMN in the two cohorts revealing consistent overconnectivity in Kir2.1 mice (§ $p = 0.013$, 2-way ANOVA repeated measurements, genotype effect, $n = 16$ and $n = 19$ Kir2.1 or GFP-expressing mice, respectively). **(c-d)** rsfMRI overconnectivity in hM4Di mice is not affected by rsfMRI global signal regression **(c)** Between-group difference maps (Pearson's r , and corresponding T stat difference maps, two-sided). **(d)** Antero-posterior profiling of rsfMRI connectivity of the PFC along the midline axis of the mouse DMN in the two cohorts upon fMRI global signal regressions (§§ $p < 0.001$, 2-way ANOVA repeated measurements, genotype effect, $n = 15$ and $n = 19$ hM4Di or GFP-expressing mice, respectively). Data in **(b)** and **(d)** are presented as mean values \pm SEM. Cg: cingulate cortex; PFC: prefrontal cortex, RS: retrosplenial cortex, TH: Thalamus; FC: functional connectivity.

2.3.2 rsfMRI overconnectivity upon acute chemogenetic inactivation of the mouse prefrontal cortex

To corroborate the specificity of Kir2.1 findings and obtain mechanistic insight into the neural correlates of the observed fMRI overconnectivity, we designed a new set of experiments in which DREADD-based chemogenetics was employed to induce a time-controlled, acute inhibition of PFC activity during rsfMRI scanning. It should be noted that the same manipulations we hereafter refer to as “chemogenetic inhibition/inactivation”, are often termed and interpreted as “chemogenetic silencing” in neuro-behavioral neuroscience (Wiegert *et al.*, 2017). An overview of experimental procedures is provided in Figure 2.5. To enable remote inhibition of fronto-cortical activity, we bilaterally transfected the PFC with the inhibitory hM4Di DREADD using a pan-neuronal promoter (Figure 2.5a), a strategy widely used to regionally inhibit excitatory neural function in behavioral studies (Wiegert *et al.*, 2017). In keeping with previous investigations, the use of a high titer viral suspension resulted in reliable and homogeneous transduction of neurons across cortical layers (Nathanson *et al.*, 2009). Three weeks after viral injection, control (GFP-transfected) and hM4Di-expressing animals underwent rsfMRI scanning or electrophysiological recordings before and after intravenous injection of the DREADD activator clozapine-N-oxide (CNO). To account for the relatively slow pharmacokinetic profile of CNO in the rodent brain (Jendryka *et al.*, 2019; Trakoshis *et al.*, 2020), both imaging and electrophysiological recordings were split into a pre-CNO injection baseline, a transitory (0 -15 min) drug-equilibration period, and an active time window (15-50 min post CNO injection) to which all our analyses refer to, unless otherwise specified (Figure 2.5b-c).

To test the efficacy of chemogenetic inhibition, we first performed a set of electrophysiological recordings in the PFC of hM4Di- or GFP-transduced control animals prior to and after CNO administration, under the same experimental conditions used in rsfMRI imaging (Figure 2.5d-e). Baseline electrophysiological traces revealed the presence of appreciable spontaneous multi-unit activity in the PFC of both groups (mean firing rate 15.0 ± 2.2 spikes/s in hM4Di-expressing, and 14.1 ± 3.8 in GFP-transduced mice, $n = 5$ each group, $p = 0.85$, t test). As expected, CNO administration robustly inhibited firing rate in hM4Di expressing mice, but not in control subjects (Figure 2.5e-f, $p < 0.01$ FDR corrected, t test). DREADD-induced PFC inhibition was characterized by a gradual decrease of neural firing upon CNO administration, reaching a steady-state approximately 10-15 min after the intravenous bolus (Figure 2.5f).

Prompted by recent work suggesting that DREADDs may alter or disrupt, rather than completely silence, neuronal activity in vivo (Schmidt *et al.*, 2019), we next examined more in detail the firing patterns of individual electrode sites in multi-unit activity (MUA) recordings. For each group, we compared the firing rates of each MUA site under basal conditions with those obtained in the same recording site upon CNO administration. A scatterplot of spike rate across paired conditions revealed that, during the active phase, the vast majority of MUA sites in DREADD-expressing mice showed a marked decrease in firing rate, with virtually no site showing any appreciable decrease in firing in control animals (Figure 2.5g). Given that MUA is strongly biased by the spiking activity of pyramidal neurons (Logothetis, 2008), these analyses suggest that our chemogenetic manipulations produce a general decrease in excitatory firing.

To probe whether acute chemogenetic inhibition of the PFC would produce rsfMRI overconnectivity as observed with Kir2.1, we next compared rsfMRI connectivity patterns in hM4Di transfected and control mice upon acute CNO administration (active phase, Figure 2.6). Recapitulating the results of chronic PFC inhibition, voxel-wise mapping revealed foci of significantly increased rsfMRI connectivity in the posterior cingulate/retrosplenial cortices and midline thalamic regions of

DREADD-expressing mice (t test, $p < 0.05$, $t > 2.03$, FWE cluster-corrected, $p < 0.05$; Figure 2.6a). Regional quantifications corroborated the presence of rsfMRI overconnectivity along the cingulate and retrosplenial axis of the DMN, and between the PFC and medio-dorsal thalamic areas (two-way repeated measures ANOVA, $F_{1,32} = 6.58$; $p = 0.0155$; t test $t_{32} = 4.30$, $p = 0.001$, respectively; b-c), a set of regions characterized by dense incoming projections from the PFC (Figure 2.7, Wilcoxon rank-sum test, $p < 0.0001$). Notably, the direction and the anatomical location of the observed rsfMRI overconnectivity was regionally unaltered by global fMRI signal regression (Figure 2.4), arguing against an unspecific contribution of arousal related global dynamics or global fMRI co-activation to the mapped changes (Gutierrez-Barragan *et al.*, 2019; Turchi *et al.*, 2018).

Baseline PFC connectivity in these areas was comparable across groups (voxel-wise mapping, $Z > 2.03$ cluster corrected, PFC-Cingulate, two-way ANOVA, $F_{1,32} = 0.48$, $p = 0.49$, Thalamo-PFC, t test, $t_{32} = 0.23$, $p = 0.81$), and overconnectivity gradually emerged in the hM4Di cohort after CNO administration, peaking during the DREADD active time-window (PFC-Rs: $T_{32} = 2.158$, $p = 0.03$, PFC-Th: $T_{32} = 4.301$, $p = 0.0001$, t test, Figure 2.6d). Moreover, no intergroup differences were observed in the estimated characteristic hemodynamic response function in this area (kernel height $p > 0.6$; time-to-peak $p > 0.12$, full-width-at-half-peak $p > 0.37$, t test) nor were between-group differences in arterial blood pressure ($p > 0.7$, t test) or blood gas levels observed (PaCO₂ $p = 0.49$; PaO₂ $p = 0.22$, t test). These control measurements rule out major spurious vascular or hemodynamic contributions and corroborate the specificity of the mapped changes. Importantly, a replication of our chemo-fMRI study in a new set of animals imaged using a combination of medetomidine and low-dose isoflurane (Grandjean *et al.*, 2020; Lee *et al.*, 2021) revealed increased rsfMRI coupling between PFC and thalamic and retrosplenial areas (Figure 2.8), recapitulating our findings in halothane-anesthetized mice. This result suggests that the observed hyperconnectivity does not reflect pharmacological interaction of DREADDs with the specific anesthetic used, but represents a more general phenomenon that extends to other sedatives

and anesthetic condition. More broadly, our chemo-fMRI results show that acute inactivation of PFC activity results in a pattern of DMN overconnectivity closely recapitulating that observed with chronic Kir2.1-mediated neural inhibition, suggesting that the ensuing overconnectivity is not manipulation-specific, nor the indirect consequence of homeostatic reactivity to protracted neural suppression.

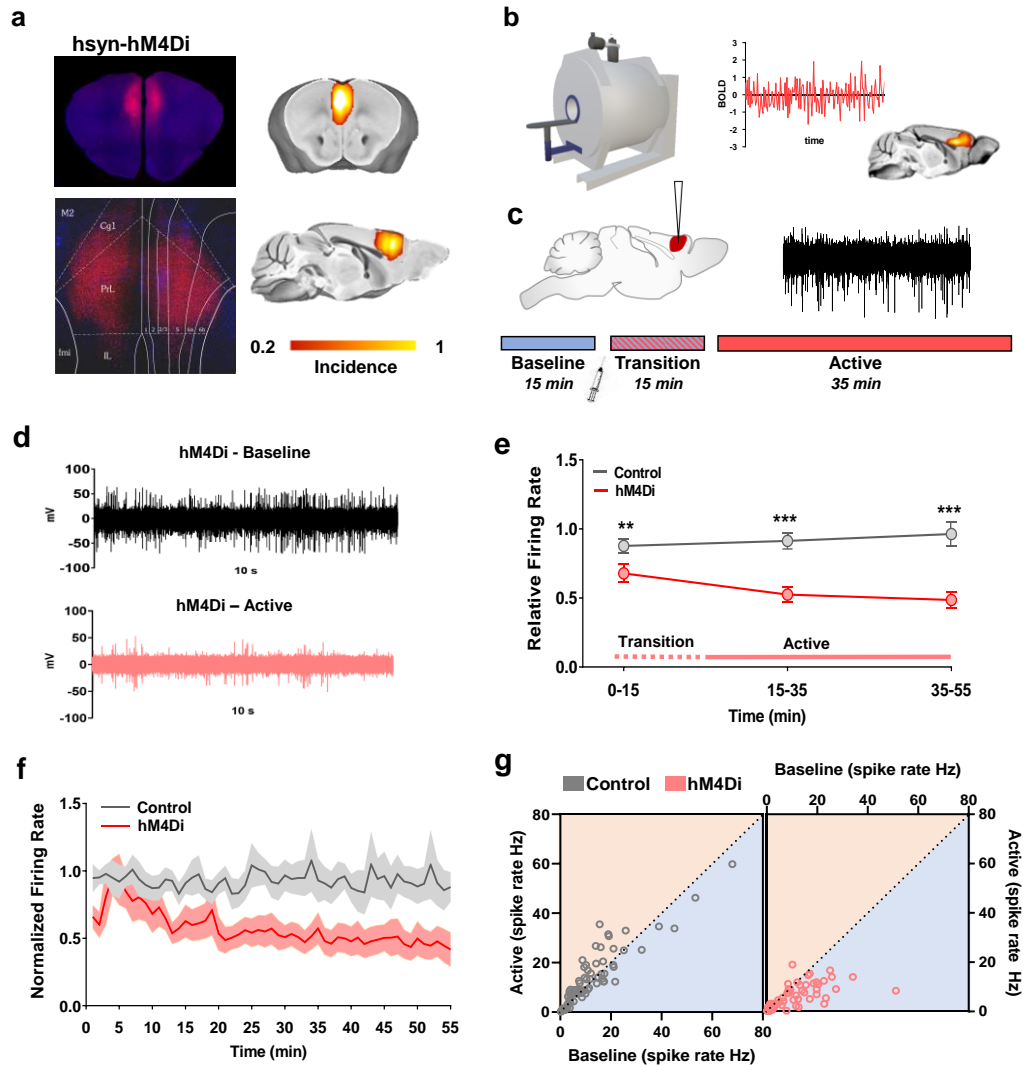


Figure 2.5 Chemogenetic inhibition of neural firing in the PFC. (a) Experimental design of chemo-fMRI experiments. AAV8-hSyn-hM4Di (n = 15) or AAV8-hSyn-GFP (control, n = 19) were bilaterally injected into the PFC of wild type. Left: Representative histology sample shown hM4Di (red) expression. Right: Heatmaps illustrate a qualitative regional assessment of viral expression across subjects. (b) Mice underwent chemo-fMRI scanning or (c) electrophysiological recordings to probe effectiveness of chemogenetic manipulations. A reference acquisition timeline is reported to depict timeseries binning into a 15 min pre-CNO reference baseline, a drug equilibration window (15 min, transition), and a 35 min CNO active time window (active). (d) Representative raw traces collected before and after CNO injection in representative recordings site of a hM4Di-expressing

mouse. **(e-f)** Reduced firing rate in hM4Di-expressing mice ($n = 5$) compared to GFP-transduced controls ($n = 5$, two-sided Wilcoxon rank-sum tests, FDR corrected $**q < 0.01$, $***q < 0.001$). Data are presented as mean values \pm SEM. **(g)** Scatterplot comparing the firing rate of individual PFC recording channels during baseline conditions (x axis) and the active phase (y axis) in control and DREADD-expressing animals (two-sided Wilcoxon rank-sum test FDR corrected, $**q < 0.01$, $***q < 0.001$).

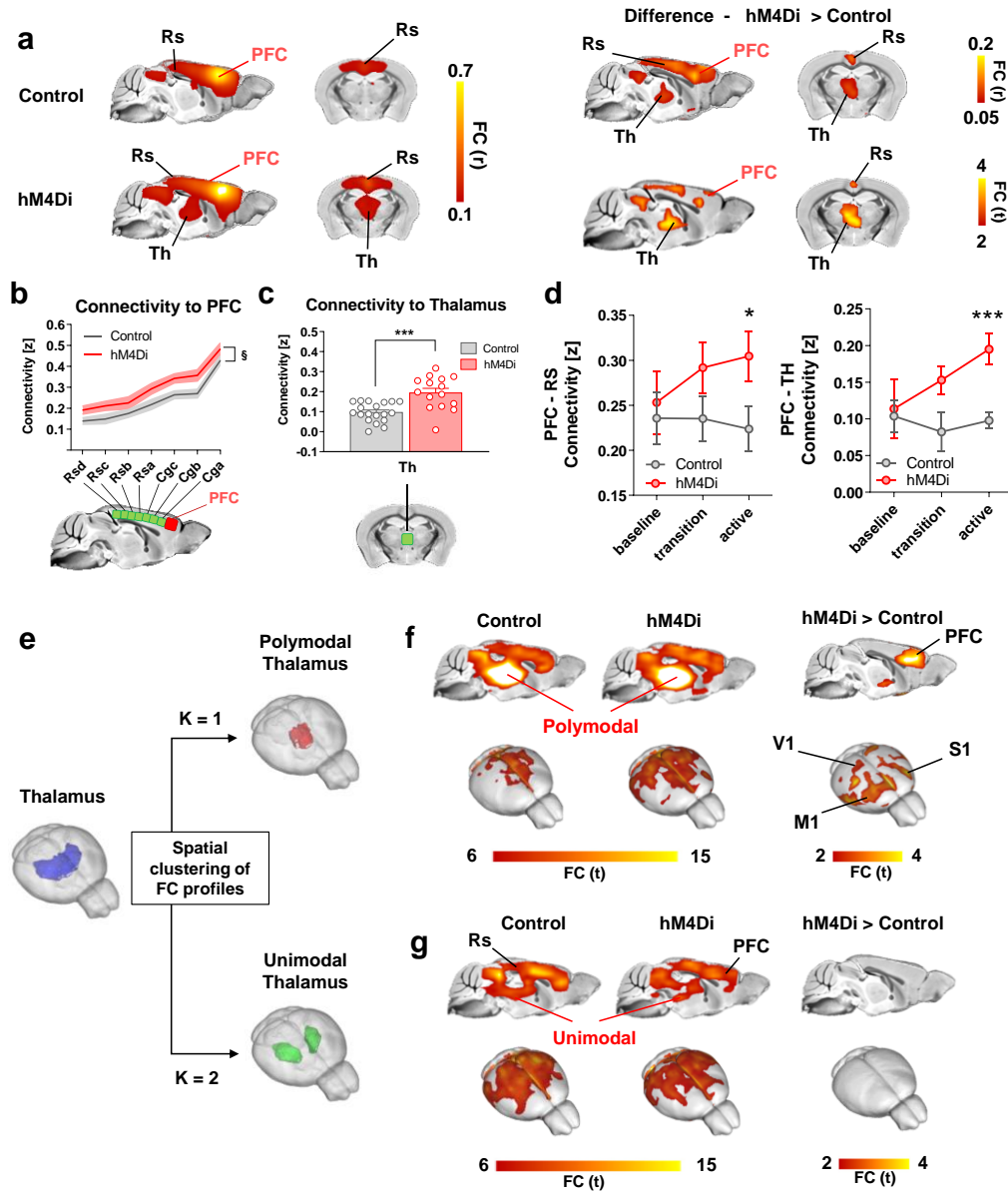


Figure 2.6 Chemogenetic inhibition of the mouse PFC results in rsfMRI overconnectivity. **(a)** Seed-based connectivity of the PFC and between group difference map revealed rsfMRI overconnectivity in the DMN of hM4Di expressing mice during the active phase. **(b)** Antero-posterior profiling of rsfMRI connectivity of the PFC along the midline axis of the mouse DMN in the two cohorts (§ $p = 0.106$, two-way ANOVA repeated measurements, genotype effect, $n = 15$ and $n = 19$ control or hM4Di-expressing animals, respectively). **(c)** Thalamo-cortical rsfMRI hyper synchronization in hM4Di expressing mice and **(d)** prefrontal-retrosplenial and prefrontal-thalamic connectivity timecourse (* $p = 0.039$, $***p < 0.001$, two-sided t test, $n = 15$ and $n = 19$ hM4Di or

GFP-expressing mice, respectively.) Data in **(b)**, **(c)** and **(d)** are presented as mean values \pm SEM. **(e)** k-means clustering of PFC-thalamic rsfMRI connectivity profiles (thalamus, blue; polymodal thalamus, red; unimodal thalamus, green) in Control (n= 19) and hM4Di (n= 15) animals. **(f-g)** Seed connectivity of sub-thalamic partitions **(f)**, polymodal thalamus; **(g)**, unimodal thalamus) and corresponding between group difference maps. FC: functional connectivity; Cg: cingulate cortex; M1: motor cortex; S1: Sensory cortex; PFC: prefrontal cortex, RS: retrosplenial cortex; Th: Thalamus; V1: visual cortex.

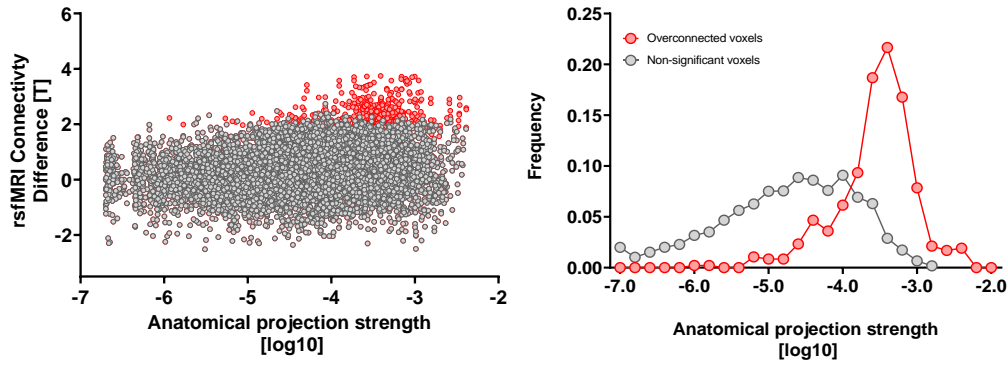


Figure 2.7 Voxels exhibiting rsfMRI overconnectivity upon chemogenetic inhibition of the PFC are robustly innervated by the PFC. Left: scatter plot illustrating intergroup differences in rsfMRI connectivity as a function of PFC structural connectivity strength. Note that all significantly overconnected voxels (red) contain robust axonal projections from the PFC. Right: distribution of voxels exhibiting the most significant rsfMRI connectivity (red) and those that are not affected (grey).

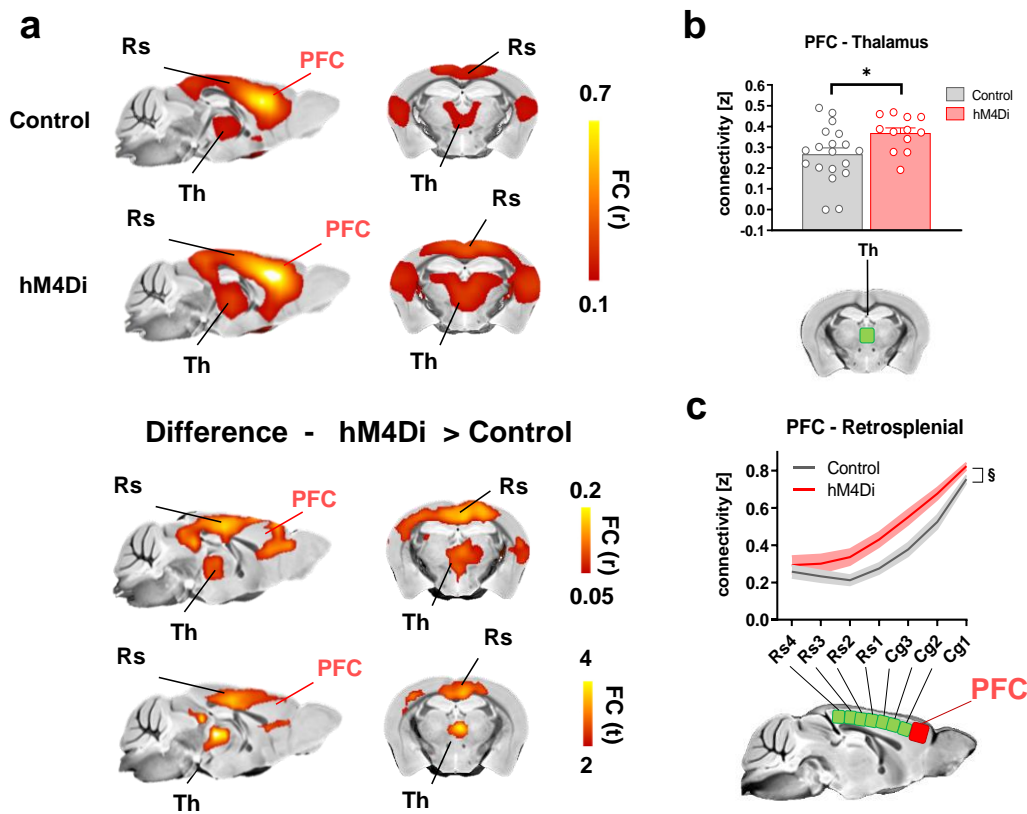


Figure 2.8 Chemogenetic inhibition of the mouse PFC under medetomidine-isoflurane anesthesia recapitulates the rsfMRI overconnectivity profile observed in halothane-anesthetized mice. (a) Seed-based connectivity of the PFC in control (hSyn-GFP $n = 19$) and experimental (hSyn-hM4Di, $n = 12$, top) animals (top) and corresponding between-group connectivity difference map (Pearson's r , and T stat, respectively, bottom). **(b)** Thalamo-cortical rsfMRI overconnectivity in hM4Di expressing mice ($*p = 0.03$, two-sided t test, $n = 12$ and $n = 19$ hM4Di or GFP-expressing mice, respectively). **(c)** Antero-posterior profiling of rsfMRI connectivity of the PFC along the midline axis of the DMN in the two cohorts (§ $p = 0.012$, 2-way ANOVA repeated measurements, genotype effect, $n = 12$ and $n = 19$ hM4Di or GFP-expressing mice, respectively). Data in **(b)** and **(c)** are presented as mean values \pm SEM. Cg: cingulate cortex; PFC: prefrontal cortex, RS: retrosplenial cortex; Th: Thalamus; FC: functional connectivity.

2.3.3 Chemogenetic inhibition of the prefrontal cortex leads to thalamo-cortical rsfMRI overconnectivity

Topographical mapping of rsfMRI connectivity upon chemogenetic inhibition of the PFC revealed foci of hyperconnectivity in polymodal medio-dorsal and centro-medial areas of the thalamus, a set of higher order nuclei densely innervated by the mouse PFC (Mitchell, 2015). We thus probed the rsfMRI connectivity of the thalamus to assess whether the observed foci of thalamic overconnectivity could underlie or involve the engagement of additional brain regions outside the DMN.

To obtain a regionally unbiased identification of polymodal (i.e. densely-PFC projecting) versus more unimodal lateral portions of the thalamus, we used k-means clustering to partition thalamic voxels based on their whole-brain rsfMRI connectivity profile, as previously described (Schleifer *et al.*, 2019). Consistent with the neuroanatomical organization of this region, our approach revealed two segregable thalamic sub-territories, one encompassing its centromedial and anterodorsal (PFC-innervated) polymodal components, and the second encompassing more lateral (unimodal/sensory) areas (Figure 2.6e). This anatomical segregation is also of potential mechanistic interest, as polymodal thalamic areas have been recently shown to serve as key generators and cortical propagators of slow neural rhythms (e.g. δ) relevant to rsfMRI coupling (Gent *et al.*, 2018; He *et al.*, 2008; Hughes *et al.*, 2002; Nir *et al.*, 2008).

Interestingly, seed-based probing of the unimodal thalamus did not reveal significant rsfMRI connectivity differences between hM4Di-expressing and control animals (Figure 2.6g), whereas seed-based probing of the polymodal thalamus revealed in hM4Di expressing-mice a widespread pattern of cortical overconnectivity, exceeding the boundaries of the PFC to encompass motor and somatosensory territories, including the retrosplenial cortex (Figure 2.6f, t test, $p < 0.05$, $t > 2.03$, FWE cluster-corrected, $p < 0.05$, Figure 2.9). To probe the network specificity of these effects, we next mapped whole-brain rsfMRI connectivity in hM4Di and control animals using a whole-brain parcellation scheme (Figure 2.10). This analysis revealed the presence of significant clusters of rsfMRI overconnectivity only in regions of the DMN and in polymodal thalamic areas of DREADD-expressing animals, the latter areas exhibiting overconnectivity with larger cortical regions. No meaningful clusters of rsfMRI over- or under-connectivity were otherwise observed in any of the areas probed. These results show that, upon acute suppression of fronto-cortical activity, PFC-innervated polymodal thalamic regions, but not unimodal areas, exhibit over-synchronous rsfMRI coupling with large cortical areas.

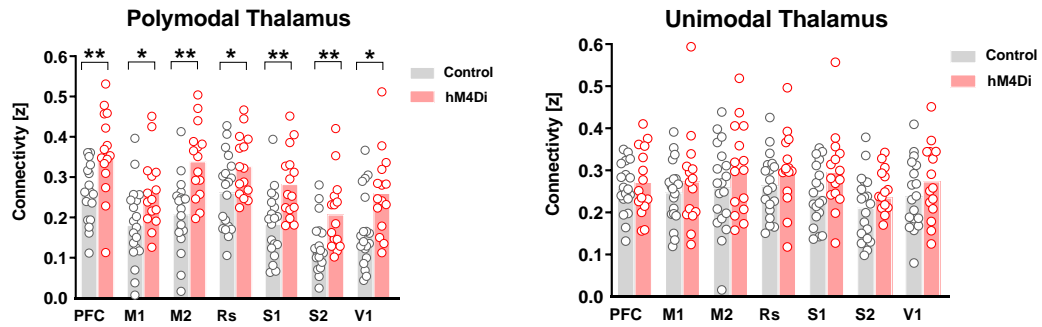


Figure 2.9 The polymodal thalamus is functionally overconnected to cortical areas. Quantification of thalamo-cortical connectivity extracted from polymodal (left) and unimodal (right) thalamic partitions (* $q < 0.05$, ** $q < 0.01$, two-sided t test, FDR corrected, $n = 15$ and $n = 19$ hM4Di or GFP-expressing mice, respectively). Source data are provided as a Source Data file. M1: primary motor cortex; M2: secondary motor cortex; S1: primary somatosensory cortex; S2: secondary somatosensory cortex; PFC: prefrontal cortex, RS: retrosplenial cortex; V1: primary visual cortex.

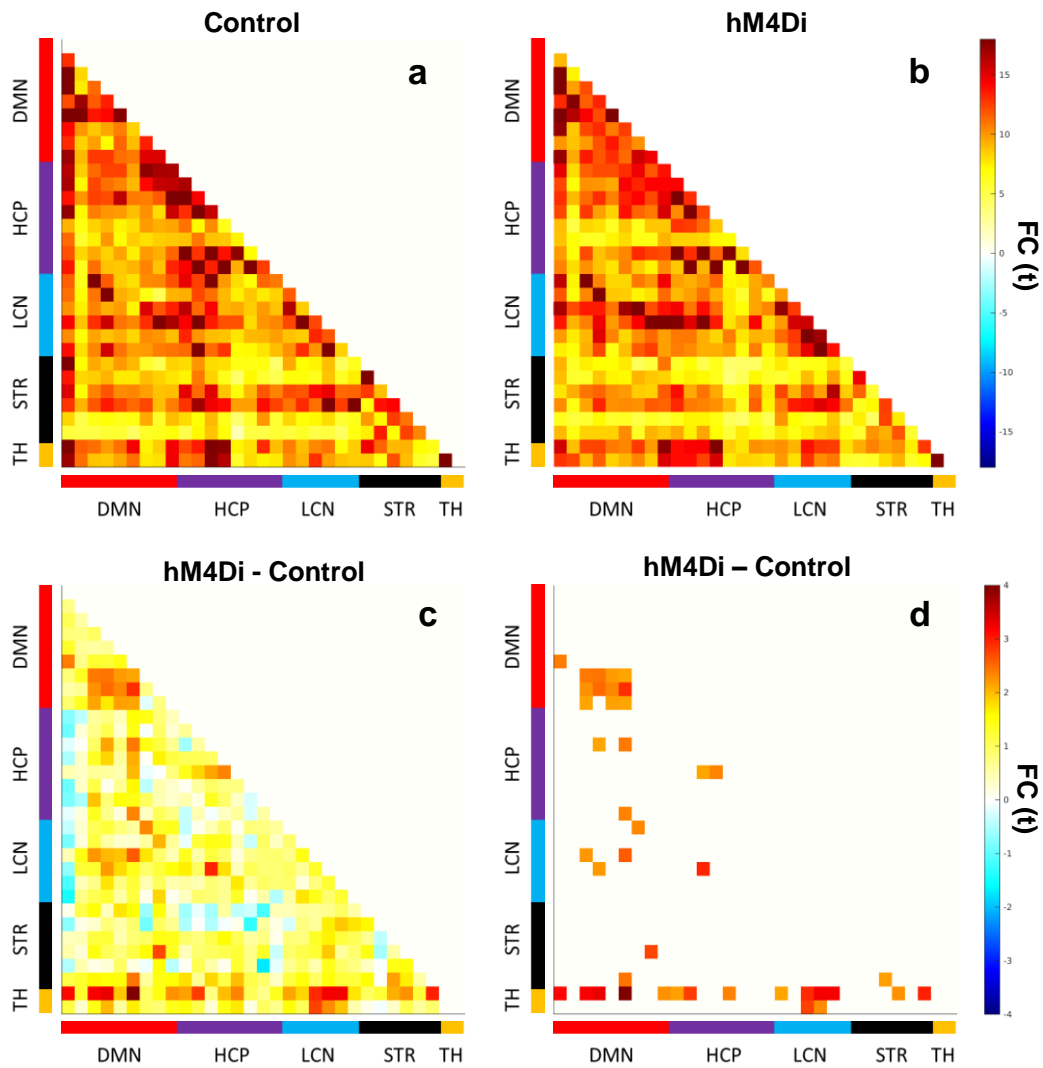


Figure 2.10 Whole-brain rsfMRI connectivity in control and hM4Di-expressing mice. Correlation matrices in (a) and (b) depict inter-areal connectivity in control and hM4Di mice respectively. (c) Mean difference map (t), and (d) regions exhibiting connectivity differences larger than $|t| > 2.1$, corresponding to $p < 0.05$, two-tailed t test (uncorrected). TH: thalamus; STR: striatum; LCN: lateral cortical network; HCP: hippocampus; DMN: default mode network; FC: functional connectivity.

2.3.4 Chemogenetic inactivation of the prefrontal cortex inhibits firing not locked to slow rhythms, resulting in increased slow oscillatory power

To obtain insight into the neural rhythms underlying the observed rsfMRI overconnectivity, we next analyzed local field potential (LFP) traces obtained from the same set of PFC electrophysiological recordings analyzed in Figure 2.5. Consistent with the observed firing rate reduction, LFP spectrograms from hM4Di-

transduced animals revealed an overall shift of LFP power towards lower frequencies, with a robust decrease in β - and γ -band power after CNO administration with respect to CNO treated controls ($F_{1,22} = 239.4$, $p < 0.1$ and $p < 0.001$, respectively, Figure 2.11a-b). Notably, the LFP power reduction in these frequency bands was also accompanied by a prominent increase in δ and slow-band (defined here as 0.1 – 1 Hz) LFP power in DREADD-expressing subjects (Figure 2.11b, slow $p < 0.001$, δ $p < 0.01$, θ $p = 0.77$; α $p = 0.34$; β $p = 0.01$; γ $p < 0.001$; Wilcoxon rank-sum tests, FDR corrected). Given that higher LFP frequencies typically reflect local neural interactions, while lower LFP frequencies are instead associated with larger scale phenomena (Einevoll *et al.*, 2013; Logothetis, 2008) these results suggest that chemogenetic inhibition of PFC suppresses local, rather than global, neural processes.

To investigate the relationship between DREADD-induced reduction in firing and the concomitant increase in local slow and δ oscillatory power, we next performed phase locking analyses of MUA firing in the PFC. Interestingly, our investigations revealed that in DREADD-expressing animals, the fewer residual spikes recorded after CNO injection exhibited strong phase locking to ongoing slow and δ LFP oscillations. Such strong phase locking was not observed in control animals or in baseline recordings, where spike distributions were instead more equally spread across δ and slow oscillation phases (Figure 2.11c-e). These observations suggest that chemogenetic inhibition of the PFC leads to a selective reduction of firing not locked to ongoing slow rhythms, resulting in a concomitant increased phase locking of residual firing to high-excitability phases of ongoing low frequency oscillations. The resulting spiking activity is therefore on average greatly reduced, but also considerably more periodic and phase-locked to underlying low frequency oscillatory rhythms.

To better illustrate the relationship between increased oscillation power and enhanced spike locking in the slow and δ bands, we performed a simple simulation. Specifically, we first simulated spike trains to have weak phase locking to a slow rhythm, with spikes happening almost equally across phase angles of the

oscillatory cycle as observed in control conditions. To mimic DREADD-induced effects, we next selectively removed spikes emitted at the non-preferred phases of slow oscillatory activity as observed in our recordings. To mimic DREADD-induced effects, we next selectively removed spikes emitted at the non-preferred phases of slow oscillatory activity as observed in our recordings. In keeping with our experimental results, this simple simulation showed that the removal of “asynchronous” off-preferred-phase firing reduces power of high frequency spiking activity, while simultaneously increasing the power of the low-frequency rhythm residual spikes are entrained to (Figure 2.12). This suggests that DREADD-induced increase in slow LFP power does not necessarily reflect the generation of a new, “artificial” rhythm, but can be simply explained by the emergence of increased phase locking to existing slow oscillatory activity.

Finally, to further probe the mechanistic specificity of our findings, we measured rsfMRI connectivity profiles produced by cell-type specific manipulations designed to increase local PFC firing. We found that chemogenetic inhibition of fast-spiking Parvalbumin (PV) GABAergic cells or hM3Dq-based excitation of pyramidal (CamkII-expressing) neurons both produced PFC underconnectivity with cortical terminals of the DMN (Figure 2.13). Notably, both manipulations produced neural signatures characterized by increased local firing rate and a robust shift of LFP power towards higher frequencies, effectively reversing the corresponding electrophysiological signature observed in our DREADD inhibition studies (Figure 2.11). These effects were far more prominent in mice undergoing DREADD-based stimulation of pyramidal neurons, a manipulation that was also associated with largely suppressed slow and δ -band LFP activity. Taken together, these new investigations suggest that the observed functional hyperconnectivity does not reflect an increased excitatory/inhibitory ratio in the PFC, or an unspecific functional inhibition of GABAergic neurons.

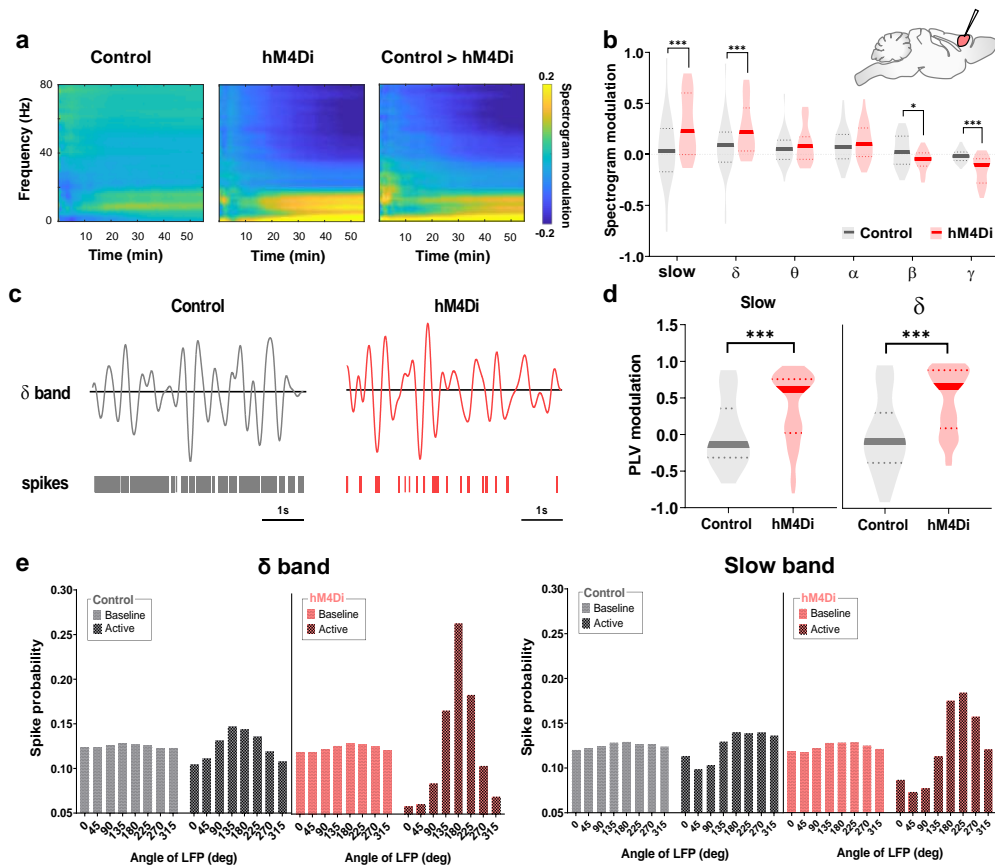


Figure 2.11 Chemogenetic inhibition of the PFC reduces γ activity but increases slow oscillatory power. (a) Mean post-injection spectrogram in control (Left), hM4Di-expressing animals (center), and mean between group difference (right). (b) Quantification of band-specific power spectrum changes upon CNO injection in both groups (* $q < 0.05$, *** $q < 0.001$, two-sided Wilcoxon rank-sum tests followed by FDR correction, for $n = 50$ and $n = 60$ statistically independent recordings from $n = 5$ hM4Di and $n = 5$ control mice, respectively). (c) Example traces of bandpassed δ -band LFPs and corresponding spiking activity (right) from a representative PFC recording channel during active phase in control and DREADD-expressing mice. Note the presence of greatly reduced, but more phase-locked firing in animals expressing hM4Di channel. (d) Violin plots depicting PLV of PFC spikes to slow and δ bands (*** $q < 0.001$, two-sided Wilcoxon rank-sum tests followed by FDR correction for $n = 79$ and $n = 80$ statistically independent recordings from $n = 5$ hM4Di and $n = 5$ control mice, respectively). (e) Probability of firing (all sessions and datapoints) as a function of the phase angle of δ (bottom) and slow (top) bands. Phase conventions are such that 0 and 180 deg represent the peak and trough of LFP, respectively. (Violin plots: thick lines represent median, dashed lines indicate 25th and 75th percentile, respectively). PLV: phase locking value.

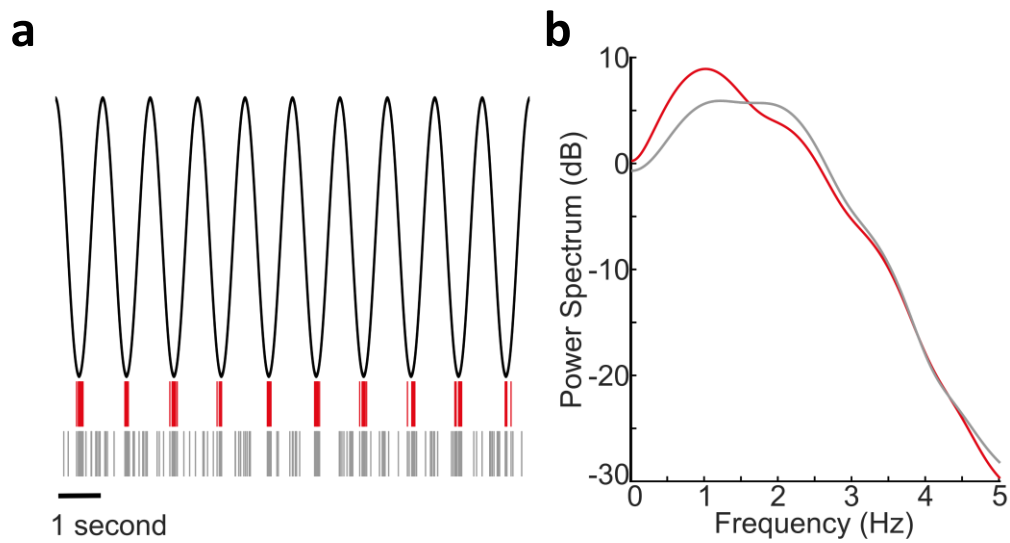


Figure 2.12 A simple simulation of the effect of suppressing neural firing not locked to slow rhythms. (a) Top (black line): 1 Hz simulated sinusoidal “LFP” wave to which spikes trains are locked. Middle (red lines): spike trains strongly locked to the LFP wave, conceptualizing firing during DREADD-induced manipulation. Bottom (red lines): spike trains obtained from the red ones but adding also an equal number of unlocked spikes, conceptualizing firing during control conditions. **(b)** Power spectra of the resulting spike trains.

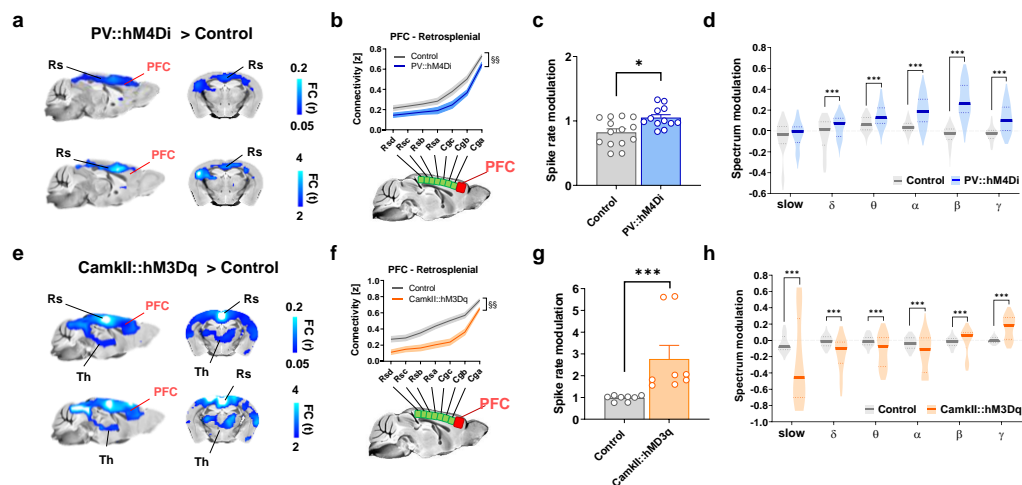


Figure 2.13 Chemogenetic inhibition of parvalbumin GABAergic cells (a-d) and stimulation of pyramidal neurons (e-h) produce rsfMRI underconnectivity. (a) Between group PFC seed-based connectivity difference maps revealed rsfMRI underconnectivity (blue) in the DMN of PV::hM4Di expressing mice during the active CNO phase. PV::Cre mice were bilaterally injected with hSyn-DIO-hM4Di ($n = 16$). Control PV::Cre animals underwent sham injections (control, $n = 17$). **(b)** Antero-posterior profiling of rsfMRI connectivity of the PFC along the midline axis of the mouse DMN (§§ $p = 0.008$, 2-way ANOVA repeated measurements, genotype effect, PV::hM4Di $n = 16$, sham $n = 17$). **(c)** Increased firing rate in PV::hM4Di mice upon CNO injection (two-sided Wilcoxon rank-sum test, $p = 0.019$, $n = 12$ and $n = 14$ statistically independent recordings in $n = 6$ PV::hM4Di and $n = 7$ control mice, respectively). **(d)** Quantification of the corresponding band - specific power spectrum changes in the PFC (*** $q < 0.001$, two-sided Wilcoxon rank-sum test followed by FDR correction, $n = 120$ and $n = 140$ statistically independent recordings in $n = 6$ PV::hM4Di and $n = 7$ control mice, respectively). **(e)** CamkII::hM3Dq > Control brain maps showing underconnectivity (blue) in the DMN. **(f)** Antero-posterior profiling of rsfMRI connectivity of the PFC. **(g)** Increased firing rate in CamkII::hM3Dq mice. **(h)** Quantification of power spectrum changes.

= 7 control mice, respectively). **(e)** Between group PFC seed-based connectivity difference map in mice expressing CamkII::hM3Dq (n = 20), or CamkII::cre mice subjected to sham viral injections (control, n = 17) during the CNO active phase. This analysis revealed the presence of robust rsfMRI underconnectivity (blue) in the DMN. **(f)** Antero-posterior profiling of rsfMRI connectivity of the PFC along the midline axis of the mouse DMN in the two cohorts (§§ p < 0.001, 2-way ANOVA repeated measurements, genotype effect, CamkII::hM3Dq n = 20, sham n = 17). **(g)** Largely increased firing rate in hM3Dq - expressing mice compared to controls (***) p < 0.001, two-sided Wilcoxon rank-sum test, n = 8 and n = 8 statistically independent recordings in n = 4 CamkII::hM3Dq and n = 4 sham mice, respectively). **(h)** Quantification of corresponding band - specific power spectrum changes upon CNO injection (***) q < 0.001, two-sided Wilcoxon rank-sum test followed by FDR correction, n = 80 statistically independent recordings in n = 4 CamkII::hM3Dq and n = 4 control mice, respectively). Data in barplots (c) and (g) are presented as mean values \pm SEM. Violin plots: thick lines represent median, dashed lines indicate 25th and 75th percentile, respectively. Cg: cingulate cortex; PFC: prefrontal cortex, RS: retrosplenial cortex; Th: Thalamus; FC: functional connectivity.

2.3.5 Chemogenetic inhibition of the prefrontal cortex increases interareal slow oscillatory coherence

The increase in slow and δ band LFP power observed in the chemogenetically-inhibited PFC led us to hypothesize that the resulting rsfMRI overconnectivity could be driven by enhanced low-frequency neural coherence, as opposed to direct interareal communication via higher frequency neural oscillations (Besserve *et al.*, 2010; Bosman *et al.*, 2012; van Kerkoerle *et al.*, 2014). To test this hypothesis, we carried out a new set of simultaneous multi-electrode LFP recordings in the PFC, retrosplenial, and centromedial (polymodal) thalamus of control and DREADD-transfected animals (Figure 2.14). We selected these region pairs because they exhibit the highest functional overconnectivity in our chemofMRI study. Spectral-power quantifications after CNO administration revealed a reduction of γ and β LFP power in all the three recording sites, together with increased slow and δ LFP power in the PFC, but not in the retrosplenial cortex or centromedial thalamus of DREADD-transfected animals (Figure 2.15a).

To explore the possible neural correlates of fMRI connectivity in terms of frequency-dependent neural communication, we next computed LFP power coherence between electrophysiological signals recorded at these electrode pairs and probed the presence of increased coupling between the recording sites. Notably, we found a clear CNO-induced increase in low-frequency LFP power

coherence in PFC-Rs and PFC-polymodal thalamic areas in hM4Di-transfected animals (Figure 2.15b). In keeping with rsfMRI evidence of increased thalamo-cortical connectivity upon PFC inhibition, enhanced low-frequency power coherence was also observed between the thalamus and retrosplenial cortex (Figure 2.15b). Quantification of these changes in canonical LFP frequency bands revealed significantly increased power coherence in the slow and δ bands for all the three electrode pairs (Figure 2.14a-c, $q < 0.05$, Wilcoxon rank-sum test, FDR corrected, all pairs). We next computed inter-areal coherence between the envelope of γ -band amplitude because ultra-slow (~ 0.1 Hz) variation in γ -band envelope has been linked to arteriole dynamics and suggested to be a contributing factor to rsfMRI coupling (Mateo *et al.*, 2017; Nir *et al.*, 2008). Mean coherence plots of γ -envelope over the ultra-slow frequency range (0.02-0.5 Hz (Mateo *et al.*, 2017)) revealed only marginally increased CNO-induced coherence in hM4Di expressing mice (Figure 2.15c). In keeping with this observation, we did not find evidence of significantly increased ultra-slow γ -envelope coherence (integrated between 0.02 to 0.5 Hz) between any electrode pairs ($q > 0.1$, Wilcoxon rank-sum test, FDR corrected).

To link these oscillatory changes to the observed rsfMRI patterns, following the procedure described in (Liang Wang *et al.*, 2012), we next compared the obtained electrophysiological coherence values with corresponding (separately-measured) interareal rsfMRI connectivity in hM4Di and control animals (Figure 2.14d-e). We first compared between-group band-specific LFP coherence differences across all electrode pairs with corresponding interareal rsfMRI connectivity changes measured during the active CNO phase (Figure 2.14d). These quantifications revealed that δ and slow LFP bands were the only frequency ranges exhibiting CNO-induced increased coherence between PFC-retrosplenial and PFC-thalamic electrode pairs, in agreement with the corresponding CNO-induced interareal rsfMRI connectivity increases (Figure 2.14d). While considerably smaller, between-group ultra-slow LFP gamma-envelope coherence also revealed CNO-induced increases in all the three electrode pairs (Figure 2.14d). Other LFP bands

did not show full concordance with rsfMRI findings: for example, β band coherence increased after CNO administration in PFC-retrosplenial but not in PFC-thalamus electrode pairs. Similarly, no meaningful between-group changes in power coherence upon DREADD stimulation was observed in the θ and γ LFP bands (Figure 2.14d). Further supporting a key contribution of slow and δ rhythms to the observed rsfMRI overconnectivity, we found that pairwise LFP coherence difference across all the recorded sites in these two bands exhibited a linear relationship with corresponding group-level pair-wise rsfMRI connectivity measured in both DREADD and control animals during the CNO active window (Figure 2.13e, δ $R^2 = 0.92$, $p = 0.002$; slow $R^2 = 0.73$, $p = 0.029$, uncorrected). Only δ LFP coupling however retained a significant correlation with rsfMRI connectivity upon FDR correction ($q=0.008$, FDR corrected). A much weaker correlation between band specific LFP coherence and pairwise rsfMRI connectivity was apparent for all the other bands (Figure 2.14e, $p > 0.11$ all bands). These findings were paralleled by the observation of similarly robust increased interareal δ - and slow-band LFP phase coherence, a widely used measure of functional synchronization in LFP/EEG studies (Bowyer, 2016) (Figure 2.14f). Taken together, these results corroborate a neural origin for our imaging findings and implicate increased slow and δ LFP coherence as a plausible neural driver of the observed rsfMRI over-synchronization.

Our findings can be summarized in a simple illustrative scheme (Figure 2.16) in which chemogenetic inhibition of the PFC (node A) reduces high-frequency local activity via a preferential suppression of spikes not locked to ongoing, global low frequency rhythms. This in turns produces a breakdown of high-frequency communication between the manipulated area and its targets (B and C). At the same time, the residual firing activity in the inhibited node becomes more entrained with ongoing low-frequency fluctuations, here depicted as a global slow rhythm. The observed functional overconnectivity may then reflect the resulting increase in interareal slow and δ LFP coherence, which we have empirically found, under our experimental conditions, to predict the direction and magnitude of

rsfMRI coupling better than the coherence of faster rhythms. Importantly, this model is also broadly consistent with examinations of LFP signatures of directionality of interactions between areas (Figure 2.17). Specifically, using phase-lag quantifications as a measure of information flow directionality, we found that in the δ band PFC activity preceded in phase retrosplenial cortex activity, a finding consistent with previous reports of antero-posteriorly travelling δ wave activity in the anesthetized mouse brain (Mitra *et al.*, 2018). Consistent with our hypothesis, after CNO administration the phase difference between PFC and retrosplenial cortex in DREADD-expressing animals was greatly reduced, implying that chemogenetic suppressions of local high frequency results in more synchronous and less phase-lagged δ activity. This finding suggests that after chemogenetic inhibition, PFC activity becomes more entrained with global, slow covarying rhythms.

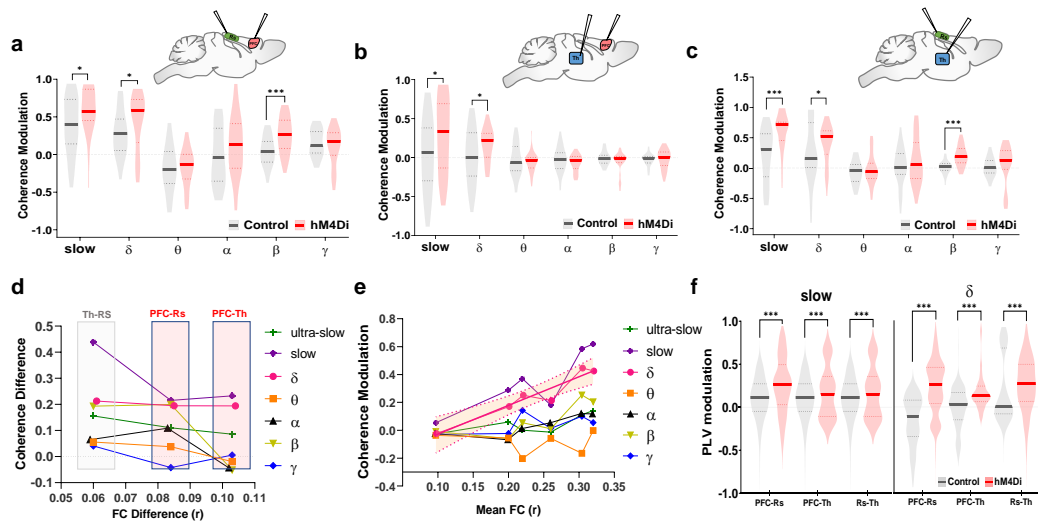


Figure 2.14 Chemogenetic inhibition of the PFC results in increased interareal slow oscillatory coherence. Baseline normalized power coherence at different frequency bands for PFC-retrosplenial (a), PFC-thalamus (b) and retrosplenial-thalamus (c) electrode pairs (* $q < 0.05$, *** $q < 0.001$, one-sided Wilcoxon rank-sum test, FDR corrected for $n = 50$ and $n = 40$ statistically independent recordings from $n = 5$ hM4Di and $n = 4$ control mice, respectively). (d) Band specific coherence and mean functional connectivity (FC) difference (hM4Di – Control) for all pairs of electrophysiologically-probed regions. Mean FC data were extracted for corresponding regional pairs during the CNO active time window in hM4Di and control animals. (e) Correlation between corresponding band specific coherence and mean functional connectivity for all pairs of electrophysiologically-probed regions (PFC-Rs; PFC-Th; Rs-Th). Shaded area indicates 95% CI for δ . (f) Baseline normalized phase coherence in slow and delta band between electrode pairs (Violin

plots: thick lines represent median, dashed lines indicate 25th and 75th percentile, respectively; *** $q < 0.001$, two-sided Wilcoxon rank-sum tests, FDR corrected). PLV: phase locking value.

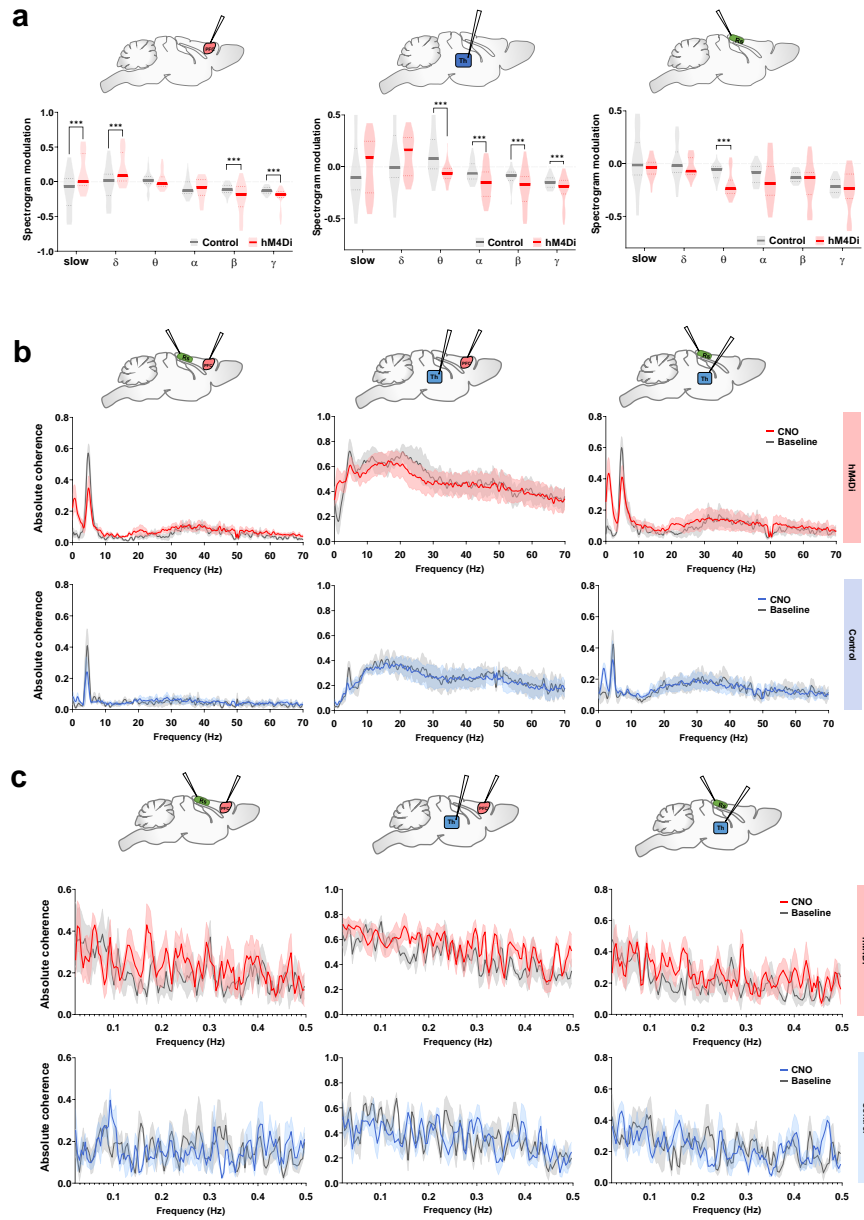


Figure 2.15 LFP power spectra and absolute coherence in multi-electrode recordings. (a) Quantification of band-specific power spectrum changes in LFPs recorded in the PFC (left), centromedial thalamus (Th; center) and retrosplenial cortex (Rs; right) upon systemic CNO administration. Power was quantified with respect to pre-injection baseline (violin plots: thick lines represent median, dashed lines indicate 25th and 75th percentile, respectively; two-sided Wilcoxon rank-sum tests, followed by FDR correction, *** $q < 0.001$, $n = 50$ and $n = 40$ statistically independent recordings in $n = 5$ hM4Di and $n = 4$ control mice, respectively). (b) Mean absolute power coherence for all pairs of electrophysiologically-probed regions (PFC-Rs; PFC-Th; Rs-Th) during both baseline and CNO active time window in hM4Di and control animals (mean \pm SEM). (c) Mean absolute power coherence of ultra-slow oscillation for all pairs of electrophysiologically-probed regions (PFC-Rs; PFC-Th; Rs-Th) computed for both baseline and CNO active time window in hM4Di and control animals (mean \pm SEM).

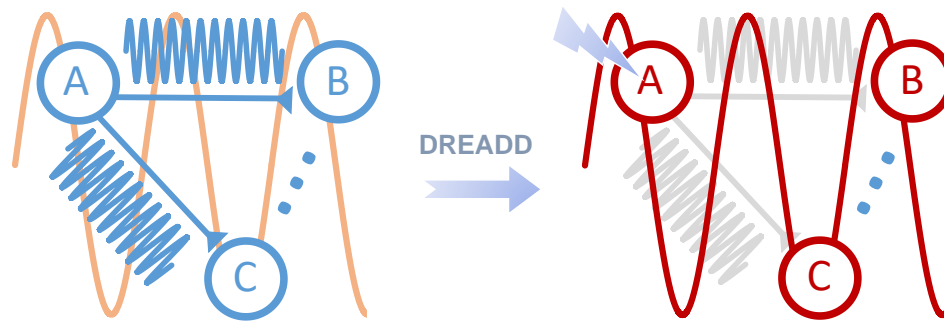


Figure 2.16 A schematic illustration of our findings. Chemogenetically inhibiting neural activity in cortical node A (i.e. PFC) reduces high-frequency direct interactions between the manipulated region and its targets (B and C), concomitantly producing higher entrainment of residual spiking activity with ongoing global low-frequency oscillations (node C). Under the assumption (supported by our data) that rsfMRI interareal connectivity is primarily driven by low-frequency neural synchronization, this interpretative framework predicts both the observed increase in interareal slow and δ LFP coherence, and the corresponding increase in interareal rsfMRI connectivity.

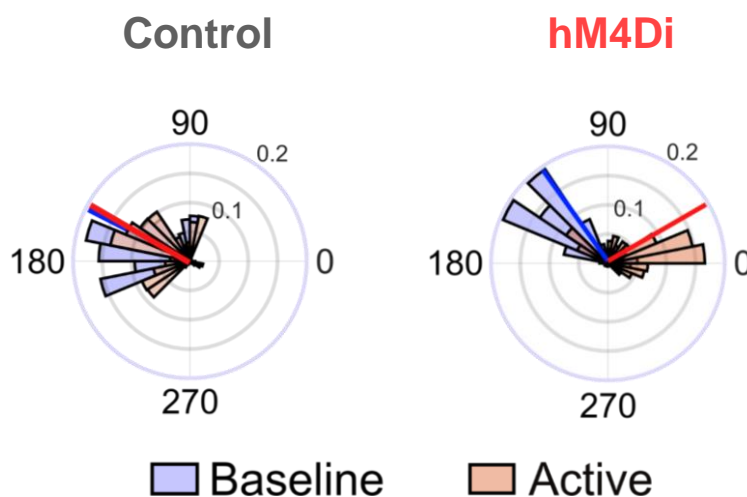


Figure 2.17 LFP δ -band phase difference between PFC and Rs cortices. Distribution of the difference in average instantaneous phase between PFC and Rs recording channels, before (baseline) and after CNO-administration (active) in control and hM4Di-expressing animals. Thick lines indicate the circular average across channels of the phase difference for baseline (blue) and active (red) phase, respectively.

2.4 Discussion

Here we combine neural perturbations and mouse rsfMRI to investigate how rsfMRI topography reconfigures in response to targeted cortical inactivation. We report that chronic and acute neural inactivation of the mouse PFC can counterintuitively increase rsfMRI connectivity with DMN targets directly

innervated by the inhibited area. Electrophysiological investigations revealed that chemogenetic inactivation of the PFC preferentially and robustly suppresses the firing activity that is not phased locked to highly excitable peaks of ongoing slow-oscillatory rhythms, leading to increased slow and δ band power, and enhanced interareal low-frequency coherence. These observations argue against a neural-independent origin for the observed hyper-connectivity, and implicate low-frequency neural rhythms in the establishment of the observed rsfMRI overconnectivity.

While critically shaped and constrained by underlying axonal connectivity (Coletta *et al.*, 2020; Hagmann *et al.*, 2008; Wang *et al.*, 2013), spatiotemporal correlations in spontaneous rsfMRI activity can dynamically reconfigure in response to local perturbations. In-depth investigations of the reconfiguration patterns resulting from regional suppression of neural activity are of special interest. These allow for a targeted deconstruction of rsfMRI coupling and may offer opportunities to mechanistically interpret aberrant rsfMRI connectivity patterns in neurological conditions characterized by loss of cortical function (Alstott *et al.*, 2009; Friston and Büchel, 2007; Grayson *et al.*, 2016). Leveraging the recent implementations of chemo-fMRI in the mouse (Giorgi *et al.*, 2017), we causally probed how neural suppression of cortical activity affects brain-wide rsfMRI coupling. In contrast to theoretical (Alstott *et al.*, 2009) and experimental (Grayson *et al.*, 2016) evidence predicting that regional inactivation of a neural node would result in reduced functional synchronization with its direct anatomical targets, we found that both chronic and acute inhibition of the PFC can counterintuitively increase rsfMRI connectivity within thalamo-cortical substrates of the mouse DMN.

Our results advance our understanding of the principles underlying brain-wide rsfMRI coupling in two directions. First, we provide causal evidence that regional suppressions of brain activity does not necessarily lead to reduced neural and functional coupling between the inactivated area and its direct anatomical projection targets, but can result in increased rsfMRI connectivity via enhanced, less-localized slow oscillatory coherence. These observations point at a highly

dynamic and non-monotonic relationship between structural and functional connectivity, underscoring a critical contribution of remote sources of large-scale neural covariation (e.g. δ and slow oscillations (He *et al.*, 2008; Pan *et al.*, 2013)) to the establishment of interareal rsfMRI coupling. This view is in keeping with correlational evidence of a dissociation between rsfMRI connectivity and underlying anatomical connections, such in the case of acallosal brains in which preserved bi-hemispheric connectivity has been repeatedly observed (O'Reilly *et al.*, 2013; Sforazzini *et al.*, 2016; Tyska *et al.*, 2011). It should be emphasized here that these results should not be intended as a refutation of the structural foundations of rsfMRI connectivity, but rather the basis of an updated framework in which reciprocal interareal rsfMRI coupling can be strongly biased, or even overridden, by slow synchronized input from global rhythm generators.

Second, our results also provide a novel reference framework for the interpretation and reverse engineering of rsfMRI overconnectivity observed in brain pathology, especially in degenerative or neurological states characterized by rsfMRI overconnectivity. Although sometimes compounded by pathophysiological rearrangements in synaptic activity (Busche and Konnerth, 2016), observations of unexpected early-stage increases in functional connectivity in degenerative or neurological conditions characterized by loss of or reduced cortical function such as Alzheimer's disease or stroke have been speculatively conceptualized as the result of compensatory rerouting of signal propagation along indirect structural paths, a neuroadaptive strategy aimed at maintaining task performance (Hillary and Grafman, 2017; Pusil *et al.*, 2019; Siegel *et al.*, 2016). Our findings offer an alternative, network-level physiological mechanism for these clinical observations, suggesting that rsfMRI overconnectivity may reflect reduced high frequency cortical activity of more local origin, and consequently enhanced phase locking of residual firing to the highly excitable phases of global low-frequency rhythms generated in subcortical modulatory centers (Reimann and Niendorf, 2020; Safaai *et al.*, 2015) and/or reflecting cortical-subcortical loops (Gent *et al.*, 2018). EEG and MEG studies in neurological populations are consistent with this hypothesis,

as rsfMRI overconnectivity and robust δ hyper-synchronization have been previously observed ipsilaterally to lesioned areas in stroke (Dubovik *et al.*, 2012; Siegel *et al.*, 2016). Similar findings have been reported in Alzheimer's disease patients, in which this effect appears to be especially prominent in polymodal cortical areas (Huth *et al.*, 2012; Ranasinghe *et al.*, 2020). Within such a framework, functional impairments in cortical activity following degenerative pathology could manifest as hyper-synchronization during pre-disease states, eventually reverting to hypotrophy-associated under-connectivity at advanced stages of brain pathology.

While a neural mass phenomenon like interareal rsfMRI coupling cannot be mechanistically dissected into discrete circuitual elements, our observation of foci of overconnectivity in polymodal thalamic areas and the increased synchronization of these with larger cortical territories is intriguing, as it points at a putative involvement of higher order thalamic relay in the generation (or propagation) of the observed overconnectivity. This hypothesis would be consistent with the observation that full expression of δ and slow oscillatory activity requires thalamic participation (David *et al.*, 2013; Hughes *et al.*, 2002), and with recent evidence pointing at the presence of a prefrontal-thalamic loop involved in the generation and propagation of δ synchronization (Gent *et al.*, 2018)). However, other modulatory mechanisms (Liu *et al.*, 2018; Safaai *et al.*, 2015) or subcortical substrates (Narikiyo *et al.*, 2020) may similarly (or alternatively) play a role in the observed overconnectivity, and the identification of neural generators of rsfMRI coupling and their involvement in the reconfiguration of rsfMRI topography in response to local perturbations remain an open issue.

The observed increases in slow and δ band coherence upon inhibition of the PFC is in excellent agreement with previous reports of a robust association between spontaneous fMRI activity and slow oscillatory activity (He *et al.*, 2008; Lu *et al.*, 2007; Neuner *et al.*, 2014; Pan *et al.*, 2013; Liang Wang *et al.*, 2012). Our findings corroborate and expand these investigations by showing that reconfiguration of

rsfMRI connectivity in response to local cortical inactivation is supported by increased interareal slow oscillatory coherence, a phenomenon reflecting DREADD-induced reduction of high frequency firing, and concomitantly increased phase locking of residual spiking activity with ongoing global low-frequency oscillations. Recent work has linked ultra-slow (~ 0.1 Hz) variation in gamma-band amplitude to the vasomotor activity underlying intrinsic rsfMRI connectivity (Mateo *et al.*, 2017; Nir *et al.*, 2008), suggesting that this rhythm may serve as a possible primary generator of interareal rsfMRI coupling. Interestingly, while we found evidence of ultra-slow γ envelope coherence across functionally connected areas under basal conditions (Figure 2.15c), the corresponding coherence increases upon chemogenetic manipulations were very small and did not correlate with corresponding pairwise rsfMRI overconnectivity. This finding suggests that, under the conditions of our manipulations, rsfMRI overconnectivity is most plausibly explained by increased canonical band (e.g. δ) low frequency inter-areal coherence.

Although the light sedation protocol used in our measurements enhances slow oscillatory rhythms (Franks, 2008), such a brain state is unlikely to be the primary reason for our observation of rsfMRI overconnectivity. Supporting this notion, increased rsfMRI connectivity between homotopic cortical regions has been observed in awake humans upon inhibitory transcranial magnetic stimulation (TMS) of the primary motor cortex (Strens *et al.*, 2002; Watanabe *et al.*, 2014). Analogously increased rsfMRI overconnectivity and δ hyper-synchronization have also been observed patients with stroke and in early stage Alzheimer's disease imaged in conscious conditions (Dubovik *et al.*, 2012; Huth *et al.*, 2012; Ranasinghe *et al.*, 2020; Siegel *et al.*, 2016). Given the highly dynamic nature of rsfMRI network activity, the sign and neurophysiological signatures identified in this study could however conceivably be affected by arousal levels. In this respect, a recent report of rsfMRI underconnectivity after chemogenetic inhibition of the rat postero-dorsal cingulate cortex is of interest in the light of a possible high-arousal state of these awake, restrained animals (Tu *et al.*, 2021). While the lack of

electrophysiological recordings in this study prevents a direct comparison with our findings, high-arousal conditions are characterized by a robust shift towards high frequency LFP activity and a possibly dominant contribution of direct feedforward interactions to interareal communication. Under these conditions, the synchronizing contribution of slow oscillatory activity may thus be largely reduced, and chemogenetic inhibition could thus produce qualitatively different effects. As robust methods for mapping rsfMRI activity in awake mice are becoming available (Gutierrez-Barragan *et al.*, 2022), systematic investigations of the effect of DREADD inhibition as a function of arousal state may help probe the plausibility of this model.

Interestingly, TMS investigations (Watanabe *et al.*, 2014) also show that excitatory pulse stimulations may produce rsfMRI de-synchronization, pointing at a possible general, inverse relationship between local cortical activity and interareal rsfMRI coupling. An analogous relationship might also be present in the mouse because, reconstituting the results of our control experiments, decreased rsfMRI connectivity has been recently observed with excitatory DREADD stimulation of somato-motor areas in lightly anesthetized animals (Markicevic *et al.*, 2020). This relationship however requires further corroboration, as KORD-based chemogenetic inhibition of the cingulate cortex was instead reported by others to produce rsfMRI underconnectivity in anesthetized mice (Peeters *et al.*, 2020). These inconsistencies reveal the critical need to couple perturbational rsfMRI studies with electrophysiological recordings to confirm the effect of the designated manipulation, and relate changes in rsfMRI connectivity to underlying neural rhythms.

A strength of our approach is the use of translationally-relevant fMRI-based readouts enabling a possible extrapolation of experimental findings to analogous human research. However, some limitations need to be recognized when assessing the generalizability of our results across species and conditions. First, the magnitude and direction of rsfMRI connectivity produced by neuronal inhibition could be manipulation specific (Wiegert *et al.*, 2017), an effect that in the case of

chemogenetics might also be compounded by possible off-target effects of commonly used chemogenetic actuators (Gomez *et al.*, 2017). By employing (unlike others, (Grayson *et al.*, 2016; Peeters *et al.*, 2020; Tu *et al.*, 2021)) a design in which CNO is administered under all conditions to all experimental groups, we were able to rigorously control any confounding effect of this actuator via a direct contrast of CNO-treated control and DREADD-expressing animals. As a result, the effects we report in the manuscript are to be attributed to the sole DREADD activation. The observation that chronic inhibition with Kir2.1 reconstitutes the overconnectivity obtained under DREADD manipulation increases our confidence in the validity of our mechanistic inferences. Second, it should be emphasized that the mechanisms that we report here may not be necessarily applicable to awake, behaving conditions, as task-dependent cognitive and sensory processing may strongly and dynamically bias brain rhythms and interregional coupling beyond what could be inferred in the resting, sedated brain. This aspect however does not diminish the translational impact of our findings, owing to the prominent use of resting-state fMRI to map functional network activity and our current inability to back-translate rsfMRI signatures of brain dysfunction into physiologically interpretable events.

In conclusion, the present work provides causal evidence that inhibition of a cortical region can lead to counterintuitively increased patterns of rsfMRI connectivity, an effect mediated by increased interareal slow-frequency coherence. These findings point at a non-monotonic relationship between regional cortical activity and network-wide rsfMRI connectivity, and define novel testable network-level mechanisms for the emergence of rsfMRI overconnectivity in clinical conditions characterized by loss of cortical function.

3 LOCUS COERULEUS AND CORTICAL STATES

In this chapter I reproduced the article published in PNAS entitled “Distinct ensembles in the noradrenergic locus coeruleus are associated with diverse cortical states” (Noei *et al.*, 2022). As in the previous study, this study too was the result of a large multi-disciplinary effort. The lab of Nelson Totah recorded all data. I performed all computational analyses. I am grateful to Nelson Totah and Stefano Panzeri for their extensive contribution of the text writing and interpretation of results.

3.1 Introduction

Flexible behavior is associated with transitions across diverse cortical states. For example, various states of wakefulness, perceptual ability, and behavioral activity are associated with different cortical local field potential (LFP) and EEG states each with its own clear spectro-temporal pattern of neural oscillations (Harris and Thiele, 2011; McCormick *et al.*, 2020; McGinley *et al.*, 2015). Behavioral state transitions, such as waking from sleep or entering a state of heightened stress and reacting more quickly to stimuli, are associated with cortical state transition. These changes are not necessarily driven by external stimuli. Instead, cortical state can be controlled by factors internal to the organism (e.g., sleep need, perceived stress) and therefore arise from self-organized neuronal interactions. It remains unclear exactly which interactions among neurons control cortical states.

Cortical states are mediated, at least in part, by the brainstem nucleus, locus coeruleus (LC). The LC releases norepinephrine to modulate neuronal excitability (Swanson and Hartman, 1975; Waterhouse and Woodward, 1980; McCormick, 1992). Noradrenergic neuromodulation of cortical state has been studied using electrical or optogenetic stimulation. Such stimulation evokes highly synchronous activation of many LC neurons because this brainstem nucleus (in rats) contains

~1,600 neurons tightly packed into a small volume of ~200 x 500 x 1000 μm (Devilbiss, 2004; Swanson, 1976). Even a low stimulation current (0.03 - 0.05 mA) pulse evokes spiking up to 400 μm from stimulation site in rat LC (Grzanna and Molliver, 1980) and thus synchronously activates many LC neurons. Such *en masse* LC population activation evokes an activated cortical state characterized by an increase in high-frequency power and a decrease in low-frequency power, regardless of whether the subject is anesthetized or not (Marzo, Nelson K Totah, *et al.*, 2014; M Steriade *et al.*, 1993; Carter *et al.*, 2010; Hayat *et al.*, 2020). Critically, it is still unknown how spontaneous population activity in the LC, as opposed to LC activity evoked by stimulation, relates to cortical states.

Although noradrenergic neuromodulation of cortical state has largely been studied using external stimulation of LC, cortical state emerges from spontaneously occurring, internal neuronal interactions. Spontaneous LC neuronal population activity has been traditionally thought to be highly synchronous (Alvarez *et al.*, 2002; Aston-Jones and Bloom, 1981a; Aston-Jones and Bloom, 1981b; Chen and Sara, 2007; Finlayson and Marshall, 1988; Ishimatsu and Williams, 1996), akin to the *en masse* population activity evoked by LC stimulation. However, this standard view might not describe spontaneous LC activity accurately. Graph-theoretic analysis of time-averaged cross-correlations among pairs of spontaneously active LC neurons in anesthetized rats showed sparse yet structured pairwise correlations that are not characteristic of highly synchronous population activity (Totah *et al.*, 2018). This suggests that LC population activity potentially consists of multi-cell ensembles that become active at different times. Importantly, however, pairwise graph-theoretic analyses were based upon time-averaged measures (Totah *et al.*, 2018) and could not detect multi-cell ensembles or resolve ensemble activity over time.

Here, we used non-negative matrix factorization (NMF) (Lee and Seung, 1999) to analyze large populations of simultaneously recorded single units in rat LC. NMF decomposes the time course of population activity into often-recurring population

firing patterns, from which ensembles of neurons that often fire together can be identified. Critically, NMF also quantifies how strongly a population firing pattern or an ensemble was active at any given time. We applied NMF to simulated synthetic spike trains and found that NMF detects the precise neuronal composition and activation time courses of each ensemble. In comparison, graph-theoretic analysis of time-averaged correlations could not detect ground truth ensemble activity in these synthetic spike trains. Importantly, unlike graph-theoretic analyses operating on time-averaged pairwise correlations of neuronal activity, NMF resolved the activity of discrete LC ensembles over time. This allowed us to demonstrate that LC population activity consists of discrete LC ensembles each with its own evolution of activity over time.

Given that LC neurons selectively project to specific forebrain regions, we investigated how individual LC ensembles are related to different cortical states. One possibility is that different ensembles may simply evoke the stereotypical activated state (as observed after LC stimulation) but with different ensembles being associated with variations in cortical activated state duration or power magnitude. A second and more intriguing possibility is that distinct LC ensembles activate during a wide range of cortical states that have different spectral signatures. This would support a new perspective that LC ensembles may contribute to the diverse set of cortical states that characterize flexible behavior. Since our methods allowed tracking the spontaneous temporal dynamics of individual LC ensembles, we could relate ongoing LC ensemble dynamics to cortical state dynamics. We calculated the cortical area 24a LFP band-limited power (BLP) and power spectra in a window aligned to the spontaneously occurring activation times of each LC ensemble. In contrast to the standard view that LC population activity evokes a stereotypical activated cortical state, we observed heterogeneous cortical states with different spectral and temporal properties that depended on which LC ensemble was active.

3.2 Materials and Methods

3.2.1 Rats and recording procedures

All experiments were carried out with approval from the local authorities and in compliance with the German Law for the Protection of Animals in experimental research and the European Community Guidelines for the Care and Use of Laboratory Animals. Male Sprague-Dawley rats (350 - 450 g) were used (specific pathogen free, Charles River Laboratories, Sulzfeld, Germany). They were pair housed. Experiments were carried out during the active period of the rats, which were housed on a light cycle of 08:00 to 20:00 darkness. A sub-set of the data were collected from rats used in a prior study (Totah *et al.*, 2018).

Neuronal recordings were made under urethane anesthesia, a widely used model for studying cortical state transitions evoked by LC stimulation (Marzo, Nelson K. Totah, *et al.*, 2014; Neves *et al.*, 2018). To date, recordings of many LC single units simultaneously in any awake organism with multi-electrode probes has been an intractable problem due to brainstem movement associated with body movement, thus necessitating the use of anesthesia to investigate the relationship between LC ensemble activity and cortical state.

Rats were anesthetized using an intra-peritoneal (i.p.) injection of urethane at a dose of 1.5 g/kg body weight (Sigma-Aldrich, U2500). Surgical procedures were as described in prior work (Totah *et al.*, 2018). Electrodes targeted the LC and the prelimbic division of the medial prefrontal cortex. The coordinates for LC were 4.0 mm posterior from lambda, 1.2 mm lateral from lambda, and approximately 6.0 mm ventral from the brain surface (implanted at a 15 deg posterior angle). The coordinates for the cortex were 3.0 mm anterior and 0.8 mm lateral from bregma and 3.0 mm ventral from the brain surface. The LC electrode was targeted based on standard electrophysiological criteria (Totah *et al.*, 2018). Briefly, we inserted a 32-electrode array and monitored the neural activity on all 32 channels during insertion. We advanced the array ventrally until the biphasic response (i.e., excitation, followed by auto-inhibition and lateral inhibition) to noxious foot shock

(5.0 mA biphasic square pulse, 0.5 msec duration) occurred clearly on all 32 channels. If the biphasic response was not observed on all channels, then the penetration was not the LC and was not included in the study. According to this criterion, we found that it was possible to have all electrodes (spanning 275 μ m in dorso-ventral axis) within the LC core, which spans 500 μ m dorso-ventrally. Our array was therefore advanced to the interior of the LC and could not span the entire extent of the LC. In addition to biphasic response to noxious stimuli, LC single units were characterized by a wide spike waveform, low firing rate, and long inter-spike intervals. At the end of the recording, we administered clonidine (0.05 mg/kg) i.p. (Sigma-Aldrich, product identification: C7897) to confirm cessation of noradrenergic neuron spiking across the entire recording array. We also verified LC targeting in most experiments using histological examination of coronal sections (50 μ m thick) that were stained for Cresyl violet or a DAB and horse radish peroxidase reaction with hydrogen peroxide to visualize an antibody against tyrosine hydroxylase, as shown in prior work (Totah *et al.*, 2018).

The LC was recorded using a multi-channel silicon probe (NeuroNexus, Model: A1x32-Poly3-10mm-25s-177-A32). The impedance of the electrodes was \sim 1.0 to 2.0 MOhm. Cortical local field potentials were recorded using a single tungsten electrode with an impedance of 200 – 800 kOhm (FHC). A chlorided silver wire inserted into the neck muscle was used as a ground. Electrodes were connected to a pre-amplifier (in-house constructed) via low noise cables. Analog signals were amplified (by 2000 for LC and 500 for cortex) and filtered (8 kHz low pass, DC high pass) using an Alpha-Omega multi-channel processor (Alpha-Omega, Model: MPC Plus). Signals were then digitized at 24 kHz using a data acquisition device (CED, Model: Power1401mkII).

3.2.2 NMF decomposition

We used NMF (Lee and Seung, 1999) to decompose a matrix of the spike counts of all simultaneously recorded single units across time intervals. NMF linearly decomposes the matrix of the spike counts of the population of single units at each

time interval as a sum across a set of non-negative basis functions (modules) using non-negative coefficients (Lee and Seung, 1999; Onken *et al.*, 2016; Williams *et al.*, 2018). Briefly, NMF as described in Figure 3.1 decomposes the population firing patterns across single units at each time interval (Onken *et al.*, 2016): $R = WH + residuals$. $R \in \mathbb{Z}_+^{T \times N}$ is the data matrix containing the spike counts of each of N single units binned into T time bins (with t being the index of each time bin). $H \in \mathbb{R}_+^{K \times N}$ is the matrix containing the basis function, which has K spatial modules. Each module captures a different pattern of coactivity of the single units and can, therefore, be used to identify which neurons are active together and thus form ensembles. $W \in \mathbb{R}_+^{T \times K}$ is the matrix containing the activation coefficients that describe the strength of recruitment of each module (and thus of each ensemble of coactive neurons) at each time interval. We binned spike counts at $\Delta T = 100$ ms. The time resolution was selected based on our previous work reporting that pairs of LC single units are predominantly synchronized on a timescale of approximately 100 ms or less (Totah *et al.*, 2018). We also used ranges of ΔT from very small values (a few ms) up to large values (a few seconds) and found that very small (≤ 20 ms) and very large (> 1 s) bin sizes artificially identify either many modules each containing only one single active unit or one large ensemble containing all single units, respectively. We chose K for each rat by computing the amount of the variance explained by the decomposition when varying K from its minimum possible value (one) to its maximum possible value (the number of simultaneously-recorded single units). after selecting K , we repeated the decomposition five times using this K and used randomly chosen initialization conditions on each repetition. The selected K was used if all solutions had a high degree of stability across these five random initializations. Stability was assessed by checking the repeatability of clustering in comparison to randomly assigning single units to ensembles. The degree of stability was computed as follows. We hard clustered the data to assign each single unit to one and only one ensemble by dividing each column of H by its maximum and removing the values below 1. From these data we then measured the stability across the five decompositions using the Rand Index (Rand, 1971). We

compared the average of the Rand index for each animal with 100 repetitions of the five random clustering. The average Rand Index was always greater than the top 5% of the distribution of mean Rand Indices resulting from random clustering. Therefore, NMF decomposition produced meaningful and repeatable ensembles. Among those random initializations, the final decomposition reported in the analyses was chosen as the one leading to the maximum variance explained.

The modules detected by NMF provide a pattern of coactivation of different single units and the activation coefficients measure the strength of recruitment of each module at any given time. From these data, we used a threshold-crossing of the coefficients to define when ensembles were active and which single units were active in the ensemble. In order to perform the thresholding, we first normalized the columns of H to the minimum and maximum and then set a threshold based on the distribution of coefficients. Single units within a module were defined as an ensemble of coactive single units if their corresponding element of H crossed the initial big peak of the histogram of the distribution of coefficient values for that rat (which usually corresponded to 95th percentile). Coefficients below this value were set to zero and values above the threshold were set to one. In the resulting binary version of the matrix, H , a value of 1 represented spatial modules corresponding to a single unit belonging to an ensemble.

The columns of the W matrix correspond to a set of activation coefficients representing the strength of recruitment of each module at any given time interval. We thresholded these continuous values into binary values using the same method explained above for the spatial modules. The binary version of the matrix, W , was used to determine whether an ensemble is active or not in each time bin.

3.2.3 The evaluation of physical clustering of ensembles according to location on the recording array

To assess whether single units within an ensemble tended to cluster on the recording array, we measured the pairwise distance between the units within each

ensemble. The location of each unit was assigned to the electrodes on which the maximal waveform was recorded. Euclidian pairwise distances of the units inside each ensemble were calculated.

3.2.4 Spike train simulation

We compared the NMF algorithm with previous work that used graph-theoretic community detection of subsets of co-active neurons from the time-averaged correlations between LC cell-pairs (Totah *et al.*, 2018), we generated three different sets of spike trains. Each set of spike trains had unique ensemble dynamics as a ground-truth. Spike trains were generated using Poisson Process, with time varying rate every 100 ms. The baseline rate was randomly sampled from a Gaussian distribution with a mean of 1 and standard deviation of 0.1. For the periods of co-activation, the rate was increased by a signal to noise ratio sampled from a Gaussian with a mean of 1.5 and standard deviation of 0.1. After the generation of the spike trains, we binned and counted the spikes every 100 ms. This matrix was fed to NMF for extraction of spatial and temporal modules. The analysis of (Totah *et al.*, 2018) was replicated as follows. Pairwise spike count correlation was calculated using Pearson correlation on the spike count matrix. A graph was made on the correlation matrix with each unit as a node and the links with the nodes was drawn only for significant correlations. The significance of the correlation was assessed by comparing to 1,000 surrogate correlations generated by shuffling spike counts randomly in time. The graph was then used as an input for the Louvain community detection which segregates nodes into groups that maximize the number of links within each group and minimizes the number of links between group by an iterative optimization procedure used to maximize a modularity score (Q) quantifying the degree to which groups separate. The degree of ensemble separation (Q) was compared to modularity scores from 1000 from shuffled networks. If Q was higher than the top 5% of the 1000 surrogate values, then adequate separation of units into ensembles was achieved (Totah *et al.*, 2018).

3.2.5 The assignment of single unit types in the ensembles

Single unit type was defined by waveform duration, as in prior work (Totah *et al.*, 2018). We determined if single units of the same type were more likely than chance to belong to an ensemble by computing the exact probability of having ensembles of the same single unit type under the null hypothesis of random assignment. These probabilities were computed by the means of repetition of random sampling (assembling) without replacement. The number of units in the sample was fixed to the number of single units in the ensemble. The number of repetitions for each rat was the number of ensembles that were empirically found by NMF to consist of only one type of single unit.

3.2.6 Auto- and cross-correlograms and permutation testing

Auto-correlograms were calculated in a 1000 ms time window using a 100 ms time bin. Cross-correlograms were calculated in a window of 2000 ms with a bin size of 100 ms. To assess significance, the correlograms were compared to the upper and lower 1% bounds of 1,000 surrogate correlograms, which were created by jittering the activation times uniformly between ± 1 s. These procedures are identical to those used in our prior work (Totah *et al.*, 2018).

3.2.7 Definition of the synchrony index

The degree of synchrony between ensemble-pairs that had a significant peak at time 0 in the cross-correlogram was measured using a synchrony index:

$$synch = \left(\frac{2 * c_{ij}}{\tau_i + \tau_j} \right) * 100$$

where c_{ij} is the number of times the two ensembles are coactive and τ_i, τ_j are the number of active times for each ensemble.

3.2.8 LC ensemble activation-aligned averaged LFP spectrogram and BLP modulations

For each detected ensemble activation event, we used for spectral analysis data comprising 400 ms before the beginning of ensemble activation, 100 ms of ensemble activation, and 400 ms after the end of ensemble activation. This window was chosen because it is the largest one, according to our data (Figure 3.3C, Figure 3.7B), for which it is unlikely that multiple ensembles were co-active during this window. Spectrograms were computed using the multitaper method with 3 tapers and time bandwidth product of 5 in a 200 ms window shifted in 10 ms steps. The spectral resolution obtained this way was ~ 4 Hz. The 200 ms sliding window size allows extracting from the analysis window an estimation of spectrograms in windows whose center falls between 300 ms before to 400 ms after ensemble activation onset, which were thus used as ranges for spectrogram plotting in Figure 3.9 and Figure 3.10. Band-limited power (BLP) was computed by filtering the LFP backward and forward to avoid phase shifts (filtfilt function, MATLAB) using a 3rd order Butterworth filter, then taking the absolute value of the Hilbert transform of the filtered signal, and finally smoothing them with a 200 ms Gaussian window (the value of the smoothing was chosen to match the size of the sliding time window used for spectrograms). For consistency, we plotted BLP and spectrograms using the same peri-event activation window ranges.

For each ensemble, we first averaged BLPs and spectrograms across all events. To compare spectrograms and BLPs across ensembles, we normalized them to a spectral modulation index defined by the ratio between the difference and sum of the spectral value at each time point and frequency bin and its time-average in the frequency bin over the entire peri-event window. This quantity at each time point and frequency bins can take values between -1 and 1 and quantifies the relative changes of power around the time-averaged power in each frequency bin.

3.2.9 Spectrogram clustering

The set of ensemble activation-triggered spectral modulations were clustered to recapitulate the main trends observed within the diversity of LC ensemble activation-triggered cortical spectrograms. The clustering was performed using the k-means algorithm (Arthur and Vassilvitskii, 2007). The k-means algorithm requires specifying a choice for the number of possible clusters and for the mathematical function used to compute the distance between the different spectrograms. We tried various definitions of distance functions (Pearson Correlation, Euclidean distance, cosine, and cityblock), and we chose Pearson correlation as distance function because it gave higher averaged silhouette values (Rousseeuw, 1987), which suggests cleaner clustering. Clustering was done on the spectrogram modulation values. We clustered the spectral modulation into $k=4$ clusters. This number of clusters was selected because it corresponded to the elbow point (defined as the first point in which the error drops below 5%) of the curve quantifying the normalized clustering error (error divided by the maximum error) as a function of the selected number of clusters. The error in the k-means clustering was computed as sum of the distances of each data point to their respective cluster centroid. We assessed the significance of the clustered spectral modulations at each time and frequency shown in Figure 3.9 by pooling the spectral modulations of all ensembles in each cluster by comparing the median of the population at each point against zero using a two-tailed Wilcoxon signed rank test. The p-values were corrected for multiple comparisons using Benjamini's & Hochberg's method for false discovery rate at $q=0.05$ (Benjamini and Hochberg, 1995).

The above analysis was done taking for clustering all spectral modulations obtained in correspondence of a detected activation of one or more ensembles. We performed a further control analyses in which we clustered only the subset of the spectral modulations during coactivation of ensemble-pairs. The clustering procedure for this control analysis was identical to the one reported above but

selected a number of clusters (corresponding to the elbow point of the error curve) equal to 2 clusters.

3.3 Results

We recorded many LC single units simultaneously (range: 5 to 34 units; average: 19 units; N = 15 male rats) under urethane anesthesia using a 32-electrode silicon probe confined to the core of the LC nucleus. Probe location was verified histologically in coronal tissue sections. Neuronal identity was confirmed at the end of the experiments using intra-peritoneal injection of the alpha-2 agonist, clonidine, which inhibited spiking on all electrodes. Spikes recorded from outside the LC core would not have been inhibited due to the lack of alpha-2 adrenergic receptors in nearby brain structures (McCune *et al.*, 1993). We simultaneously recorded cortical LFP (8 kHz lowpass filtered) from cortical area 24a (anterior cingulate cortex) (Paxinos and Watson, 2017) using a tungsten electrode in 9 of the 15 rats.

3.3.1 NMF detects the neuronal composition and activation times of ensembles

It is currently unknown whether the spontaneous LC population activity that we recorded is composed of ensembles (subsets of simultaneously active neurons) and how ensemble activity changes over time. A graph-theoretic community detection analysis of time-averaged pairwise correlations in the LC demonstrated groups of units linked by pairwise time-averaged correlations (Totah *et al.*, 2018). This result is compatible with the possibility that spontaneous LC activity consists of ensembles. However, this analysis may fail to detect ensembles if their interaction is based on higher-order interactions between larger groups of neurons that cannot be linearly decomposed into pairwise correlations (Battiston *et al.*, 2021). Moreover, such time-averaged analysis cannot identify the times at which individual ensembles are active, which is needed for studying the

relationship between spontaneous LC ensemble activity and ongoing cortical state. Thus, we need a methodology to detect ensembles and measure their activation times. Among available alternatives (Cunningham and Yu, 2014), we chose to use NMF because it offers several advantages given the nature of spike trains (Williams *et al.*, 2018; Onken *et al.*, 2016). First, NMF linearly decomposes spike trains based only on non-negative constraints on the detected firing patterns and their strength of activation over time. This non-negativity constraint is a minimal and biologically grounded assumption for spike trains. Second, unlike decompositions that are based on orthogonality constraints (Carrillo-Reid *et al.*, 2019), NMF has been designed and proven to work well even when different ensembles are non-orthogonal because they activate partly overlapping in time or because some neurons participate in multiple ensembles. We first use synthetic spike trains with ground-truth ensemble activity patterns to demonstrate how NMF goes deeper than the graph theory analysis previously applied to LC data (Totah *et al.*, 2018) to identify recurring firing patterns, extract ensembles from these firing patterns, and determine the ensemble activation dynamics over time. Figure 3.1 illustrates how NMF works using three different hypothetical scenarios of simulated spike trains. Each scenario consisted of simulated spike trains from 10 single neurons. The ground-truth ensemble dynamics were different in each scenario. In the first scenario (Figure 3.1A), two ensembles (ensemble #1: units 2-7; ensemble #2: units 9-10) were strongly activated at distinct times. In the second scenario (Figure 3.1B), the same two ensembles were strongly activated at distinct times in the first and third part of the simulation, were inactive in the second part, and then were simultaneously co-activated in the last part of the simulation. Finally, in the third scenario (Figure 3.1C), we simulated three distinct ensembles (ensemble #1: units 2-4; ensemble #2: units 5-7; and ensemble #3: units 9-10). Ensembles 1 and 2 had different temporal activation patterns with often only one of the two ensembles being active, but they also had a period in which they were both strongly coactive.

NMF decomposes the rate matrix containing the population vectors at all time points into a sum of K non-negative spatial modules, each of which is multiplied by a non-negative activation coefficient. Formally, a spatial module is a vector (one entry per neuron) specifying the relative strength of firing of each neuron (Williams *et al.*, 2018; Onken *et al.*, 2016). A spatial module may be thought of as an often-recurring, population firing pattern. Thresholding these spatial module values defines the ensemble of specific single units that were significantly active within each module. For example, in Figure 3.1A and Figure 3.1B, NMF identifies spatial module #1 as a population firing pattern consisting of high activity of units 2-7 and low activity for the other units. The high (thresholding-crossing) module values identify units 2-7 as the ensemble #1 that was activated in module #1. For each spatial module, its activation coefficient at any given time describes how strongly the spatial module (and thus the ensemble of co-active units within it) is recruited. By thresholding the activation coefficients, we detected the times of occurrence of each spatial module (population firing pattern) and of the associated ensemble. These will be referred to as “ensemble activation times.”

The number of spatial modules (K) was determined, both for these synthetic data and for actual LC population recordings, based on two criteria. First, the chosen K explained a high amount of variance in the data with the fewest possible spatial modules. K was in the “elbow” region of the reconstruction error, which when plotted as a function of the possible number of spatial modules (Figure 3.2), such that a higher K would have given diminishing returns in data reconstruction accuracy. Second, the selected K yielded stable spatial modules regardless of the random initialization of the procedure.

We previously used graph-theoretic analysis of time-averaged cross-correlations to detect correlated activity among multiple pairs of LC neurons (Totah *et al.*, 2018). To understand how it compares with NMF, we performed this previous analysis on the synthetic spike trains. Despite the difference in ensemble dynamics, ensemble composition, and number of ensembles across scenarios, graph theory detected the same two groups of strongly correlated units in each

scenario (Figure 3.1). The temporal activation patterns of these neuronal groups cannot be obtained because graph-theoretic analysis uses time-averaged activity. Therefore, while graph-theoretic analysis could not identify the precise neuronal composition of ensembles or their activation dynamics, NMF identified these ensemble properties correctly in all three simulated scenarios.

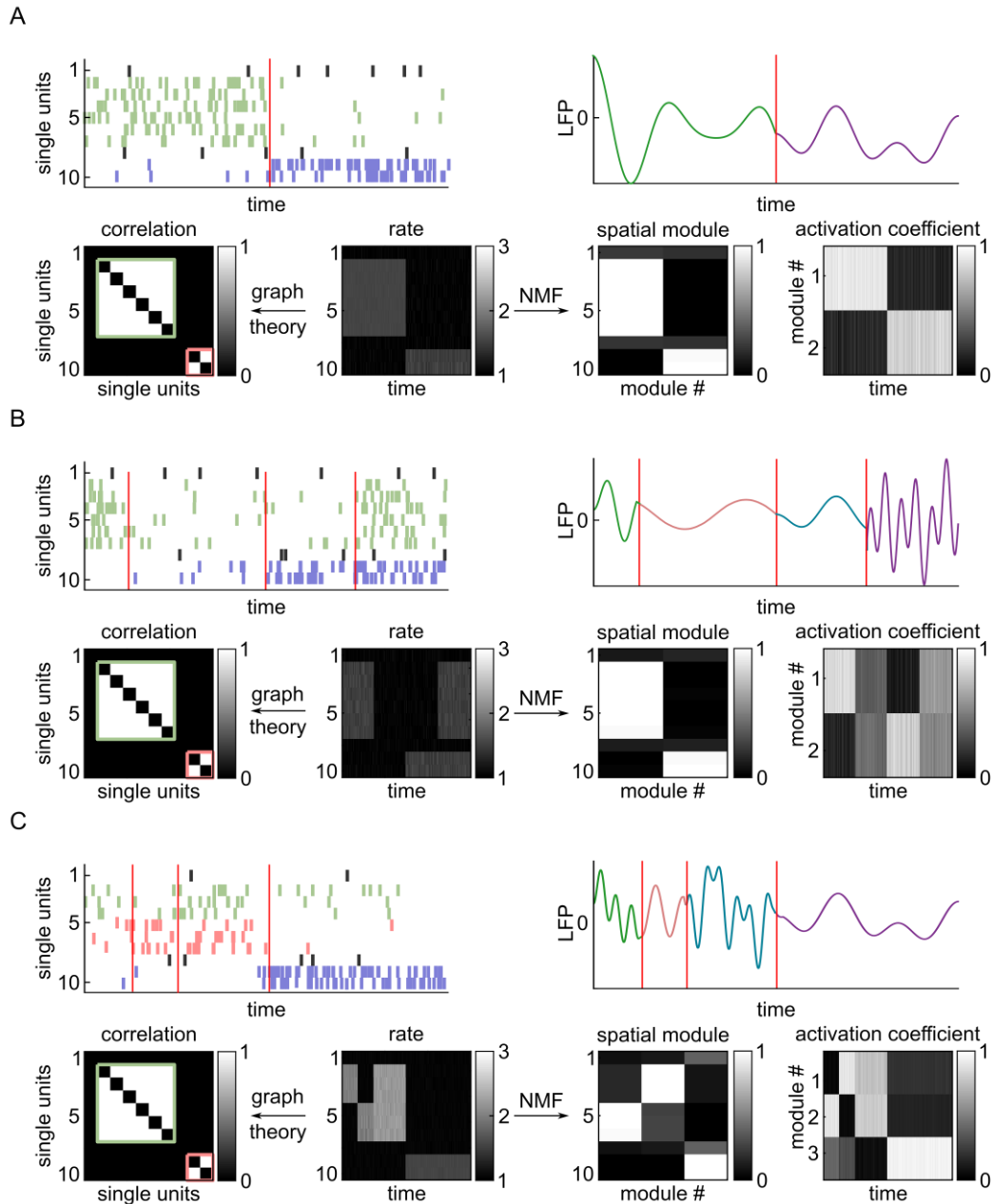


Figure 3.1 Comparison of NMF versus graph-theoretic analysis for detecting ground-truth ensemble dynamics from synthetic spike trains. Three different simulated spike rasters were generated to compare the NMF method with the graph-theoretic method. **(A)** Scenario #1 (2 ensembles active at distinct times). **(B)** Scenario #2 (2 ensembles active at distinct and overlapping times). **(C)** Scenario #3 (3 ensembles active at distinct and overlapping times). In all panels, the upper left plots depict the simulated spike rasters of 10 single units. The spikes belonging to

different ground-truth ensembles are in different colors. The red lines indicate transitions in the population activity. The top right plots show the simulated ongoing cortical LFP with different cortical states plotted in different colors. Lower panels show the binned spike rates of each unit in the middle and neuronal groups detected by graph-theoretic analysis of time-averaged pairwise correlations on the left. White indicates a significant time-averaged correlation for the pair defined by each axis. Groups of co-active neurons are indicated by the green and red boxes (see SI Appendix for graph-theoretic algorithm). Panels on the right show the NMF decomposition into the spatial modules and their activation time courses (right).

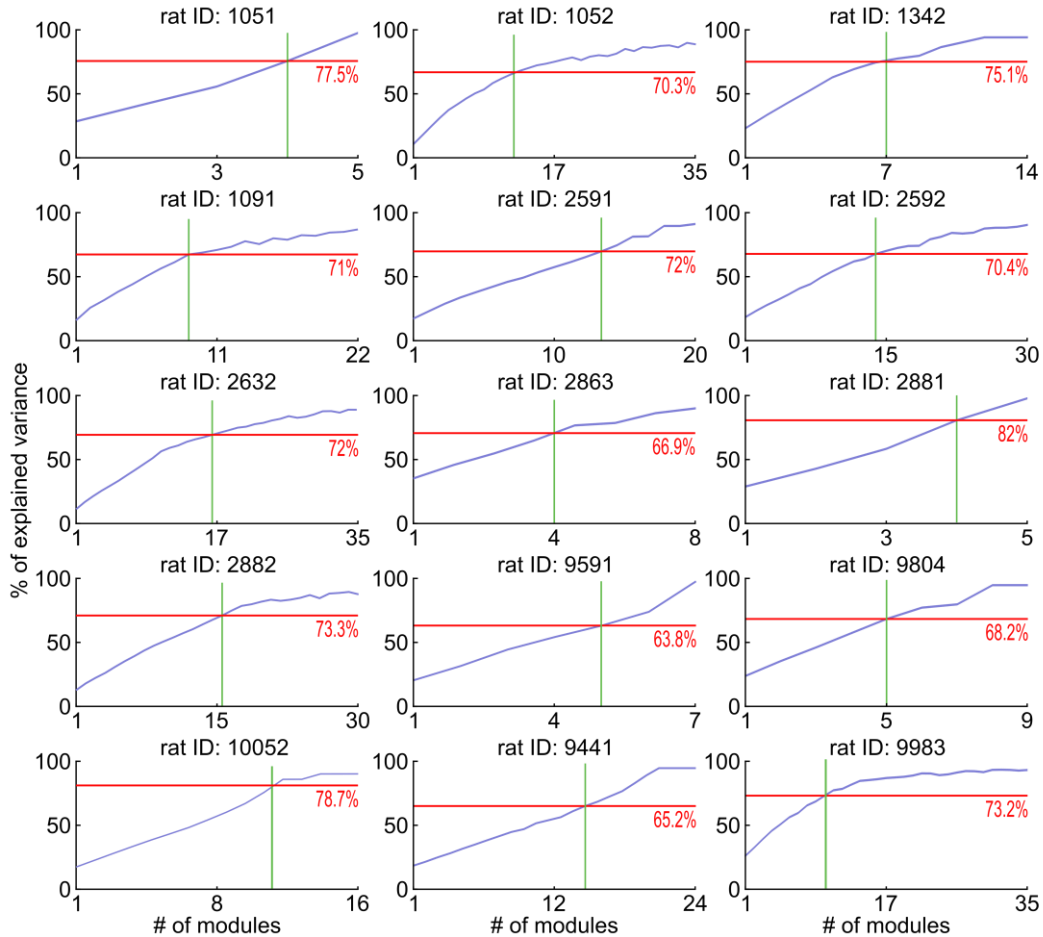


Figure 3.2 Data underlying the choice of the optimal number of modules (K) in each rat. Each panel depicts the percentage of explained variance versus the number of the modules for each rat. Solid green lines show the number of selected modules based on the criteria of first elbow after at least 60% of variance is explained. The dotted red lines show the amount of the explained variance at the selected number of modules.

3.3.2 Spontaneous LC population activity consists of distinct ensembles with largely non-overlapping activation dynamics

We assessed whether LC population activity consists of ensembles using NMF on the population matrix containing the time-dependent binned spike count vectors

of simultaneously recorded single units independently for each rat. We binned activity in 100 ms sliding windows, which is the time scale capturing most of the synchrony among LC single unit pairs (Totah *et al.*, 2018).

NMF found 146 ensembles of co-active LC single units from 15 rats. Figure 3.3A shows an example ensemble from a recording of 24 single units. The rasters show 7 single units that spontaneously co-activated as an ensemble for a transient period of ~ 100 ms, as well as the unchanging baseline-level activity of the remaining 17 units not assigned to that ensemble. The corresponding peri-event time histograms (PETHs) describe the time course of average spike rate for single units within the ensemble and the single units not assigned to that ensemble. Around the time of ensemble activation (at $t = 0$ s), units assigned to this example ensemble co-activated, whereas the activity of units outside the ensemble did not change. We verified over the entire dataset that single units not assigned to an ensemble did not increase their spike rate when the ensemble was active, whereas units assigned to the ensemble did (Figure 3.4).

Figure 3.3B shows an example in which LC population activity was decomposed into 5 distinct ensembles. The ensembles were active in most cases at different times, but occasionally more than one ensemble was simultaneously active (e.g., brown and red lines at $t = 0.5$ s). Reconstructing the total population firing rate as function of time through NMF decomposition (i.e., essentially summing up the activation time courses across the 5 ensembles) returned a close approximation of the pooled population spike rate. This example suggests that LC neuronal population activity is composed of distinct ensembles that activate at largely non-overlapping times.

Most ensembles were only transiently active for 100 ms (Figure 3.3C). The median \pm standard error of the median activation duration over all ensembles was 114 ± 8 ms ($N = 146$ ensembles). The average PETH across all ensembles showed that activation decayed sharply around 100 ms after activation onset (Figure 3.4). However, distinct ensembles were quiet for a wide variety of durations between these brief activations (Figure 3.3C). The duration of the inactive periods was

highly variable across ensembles (median \pm standard error of the median = 611 ± 295 ms). These findings are compatible with the view that distinct ensembles have different spontaneous dynamics.

LC neurons spontaneously fire bursts of action potentials, typically with an inter-spike interval of < 100 ms (Tung *et al.*, 1989; Rajkowski *et al.*, 1994; Foote *et al.*, 1980; Cedarbaum and Aghajanian, 1978; Hervé-Minvielle and Sara, 1995); therefore, as also assessed whether LC ensemble activation times could occur in a burst pattern. We calculated auto-correlograms of the time course of the ensemble activation coefficients (Figure 3.5). We found almost no inter-activation intervals in the 100 ms after ensemble activation. The most prominent characteristic of ensemble activity dynamics was a tendency for rhythmic ensemble activation at 500 to 700 ms. Thus, burst patterns did not occur in LC ensemble activation dynamics.

Ensembles were comprised of relatively small subsets of single units. On average, 27% of single units were active in ensembles relative to the total number of simultaneously recorded single units in each rat (Figure 3.3D). Ensemble size ranged from 6% - 62% of the simultaneously recorded single units (Figure 3.3E). We assessed whether ensembles consisted of disjoint sets of single units or overlapping single units. Out of 285 single units, 115 participated in multiple ensembles (40.4%), 149 participated in only ensemble (52.3%), and 21 did not participate in any ensemble (Figure 3.3F).

Ensembles preferentially consist of one type of LC single unit (narrow or wide (Totah *et al.*, 2018)), defined by their extracellular waveform shape (Figure 3.3G). We assessed if the proportion of each unit type participating in each ensemble was statistically different from what would be expected if ensembles were formed by units taken by random resampling regardless of type. For all rats, the hypothesis that ensembles are formed by combining units regardless of their type was rejected ($p < 0.05$).

We examined the spatial distribution of units within the ensembles. We assessed (by randomly shuffling the recorded location of units) whether the median

distance between unit-pairs within the ensemble differed from a random spatial organization. Location was defined as the electrode on the array that recorded the maximal spike amplitude (averaged across all spikes). Only a small proportion of ensembles (18 out of 121 ensembles with more than 2 units) had a median distance between unit-pairs that differed from the one expected by a random spatial organization (at $p < 0.05$ with the null hypothesis distribution, computed with 100 shuffles) (Figure 3.3H). Finally, for each ensemble there was no difference in the distribution of distances between unit-pairs belonging or not belonging to the same ensemble (Wilcoxon's rank sum test with FDR correction for 121 ensembles; lowest p-value was $p = 0.1434$). These results are consistent with a non-topographical, diffuse arrangement of LC neurons spontaneously firing as an ensemble.

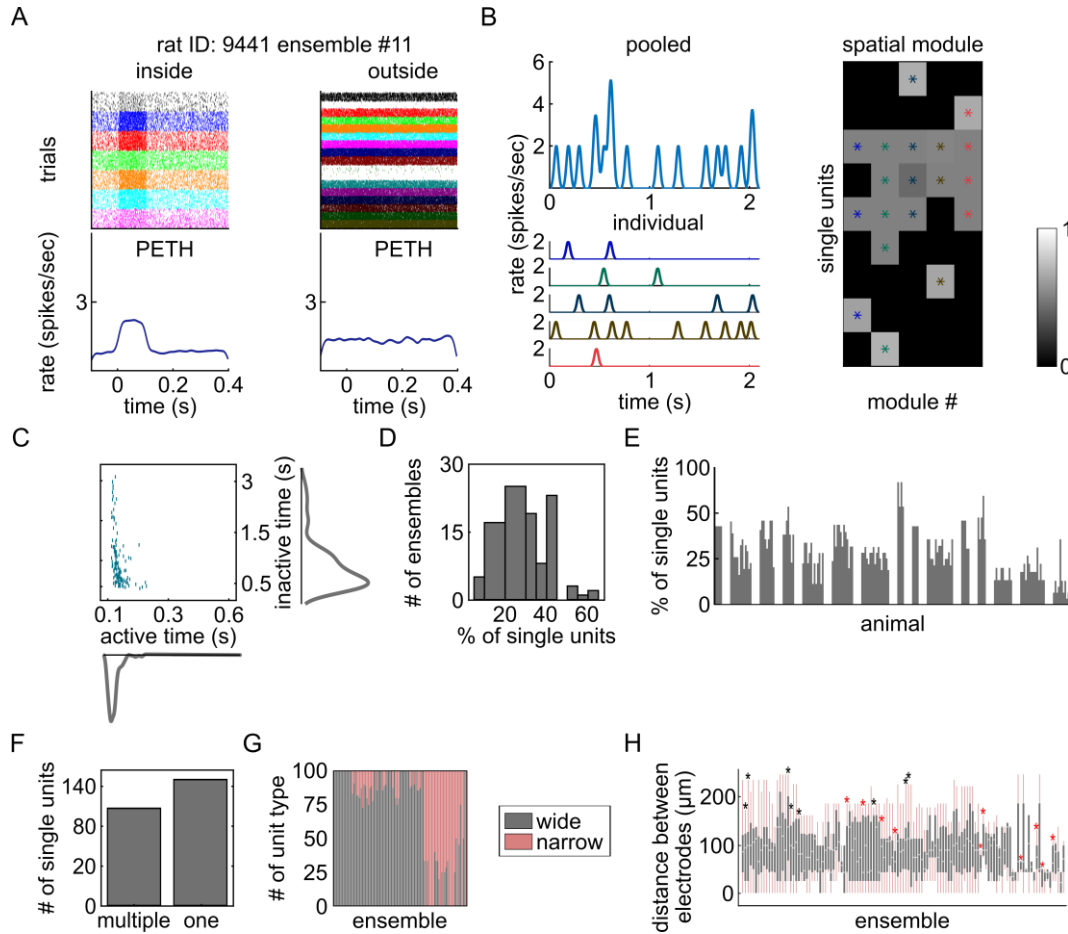


Figure 3.3 The characteristics of LC ensembles. (A) The spike rasters and PETHs are shown for one exemplar ensemble. The left panel shows spike rasters of the single units inside the ensemble aligned to the ensemble activation times ($t = 0$ sec). The right panel shows the same for other simultaneously recorded single units that were not assigned to this ensemble. Each ensemble activation event is a “trial” in the spike raster. The PETHs show the of spike rate averaged over units in the ensemble and then averaged over all detected ensemble activation events. (B) An example LC recording in which NMF found 5 ensembles among 9 single units. The upper left panel plots the population activity pooled by summing spike rate across all simultaneously recorded single units. The lower left panel plots the activation coefficients of 5 individual ensembles in different colors. The right panel plots the spatial module values for each single unit. A threshold was applied to these values to identify which single units were significantly active in each spatial module firing pattern. Units that crossed the threshold are marked with an asterisk and form an ensemble (each color is an ensemble). (C) The scatter plot shows the average ensemble active times versus inactive times along with the corresponding histograms. (D) The distribution of ensemble sizes is plotted. The values are the percentage of simultaneously recorded single units that were assigned to an ensemble. (E) Each bar reports the percentage of single units assigned to one ensemble. Bars are grouped by rat. Note that a single unit can be part of more than one ensemble. (F) The number of single units participating in one ensemble or multiple ensembles. (G) The percent of each unit type (wide or narrow) making up each ensemble is plotted across ensembles. Rats in which only one single unit type was recorded are not included in this plot. (H) Boxplots show the distribution of the distances between each pair of single units within each ensemble. Ensembles with only two single units were excluded. The light grey line shows the median, the gray box shows the interquartile range, and the pink line shows the full range of the data. Asterisks indicate the ensembles with pairwise distances between units within the ensemble having a more diffuse (black asterisks) or more constrained (red asterisks) spatial organization than expected from a random spatial distribution.

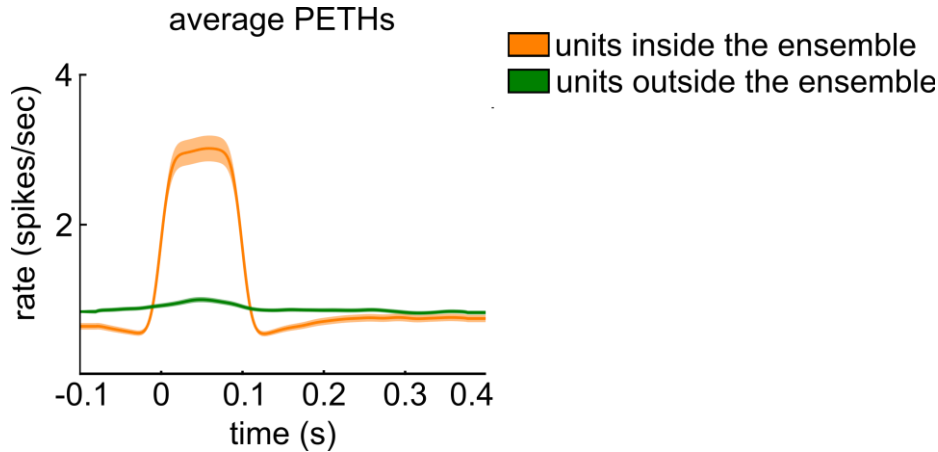


Figure 3.4 Spike rates of units inside and outside LC ensembles around the time of spontaneous LC ensemble activation. Average PETHs over all the ensembles ($N = 146$). The zero time on the x-axis is the ensemble active time. Line and shaded area report the mean and SEM across ensembles, respectively.

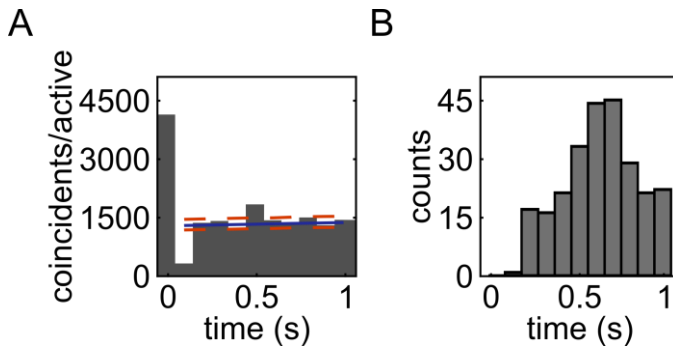


Figure 3.5 Ensemble auto-correlogram peaks. (A) The histogram plots the auto-correlogram (time binning of 100 ms) of the activation time course of an example ensemble (#3 from rat 1091). Significant peaks were defined as those that had auto-correlogram values above the 99th percentile (upper dashed orange line) of the surrogate distributions of correlogram values computed by randomly jittering ensemble activation times. The solid blue line shows the average of the surrogate correlograms. (B) Histogram of the number of significant auto-correlogram peaks as a function of time lag. 117 out of 146 ensembles had a significant peak.

3.3.3 LC ensembles are temporally distinct and are sparsely active

Before considering how the activation of LC ensembles relates to cortical states, it is important to further characterize the relative dynamics across ensembles in order to form hypotheses about whether different ensembles have a sufficiently distinct dynamics to potentially produce ensemble-specific cortical states. We first characterized when the activation of an ensemble makes it less likely that the same or another ensemble is active at some other time. We computed auto-correlogram and cross-correlograms of the time course of the ensemble activation

coefficients and detected significant troughs in the correlograms (Figure 3.6A, B). A trough in the auto-correlogram occurred in 62% of the ensembles (90 out of 146). For these ensembles, the decreased spiking was most frequent at a 100 ms delay after ensemble activation but could occur as late as 300 ms after ensemble activation (Figure 3.6C). We found that 44% of ensemble-pairs (348 out of 790) had a significant cross-correlogram trough. Cross-correlogram troughs were most frequent after a delay of at ± 300 ms, but covered a wide range of times lasting up to 1 s (Figure 3.6D). The times at which troughs were observed match well the wide range of pauses apparent in ensemble activity shown in Figure 3.3C. These pauses in the activity of single ensembles and in the relative timing between ensemble-pairs produce sparse activations of distinct LC ensembles and provide evidence that different ensembles have distinct activation dynamics.

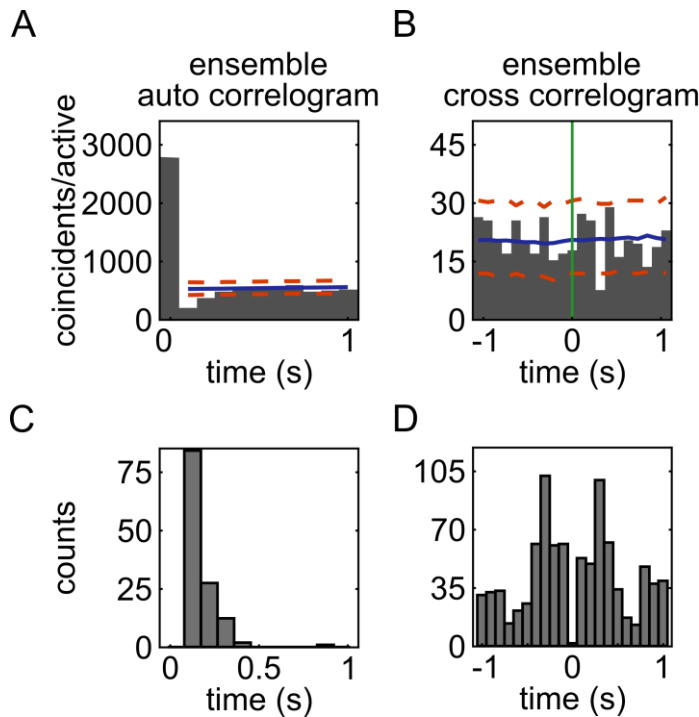


Figure 3.6 Ensemble auto-correlogram and ensemble-pair cross-correlogram troughs. (A) The histogram plots the auto-correlogram (time binning of 100 ms) of the activation time course of an example ensemble (ensemble #5 from rat 2591). A trough in the auto-correlogram denotes post-activation inhibition. Significant troughs were defined as those that had auto-correlogram values below the 1st percentile (lower dashed orange line) of the surrogate distributions of correlogram values computed by randomly jittering ensemble activation times. The solid blue line shows the average of the surrogate correlograms. (B) The histogram plots the cross-correlogram of the activation time course of an example ensemble-pair (ensembles #9 and #11 from rat 2632). The activation time of the reference ensemble is at $t = 0$ s (green line). A frequent silence of one ensemble 400 ms after the other spontaneously activated is shown by the significant trough. Plotting conventions are as in panel A. Significant troughs of cross-correlograms were computed

with the same method used for the auto-correlograms. **(C)** Histogram of the number of significant auto-correlogram troughs as function of the time lag. **(D)** Histogram of the number of significant cross-correlogram troughs across time lags.

3.3.4 LC ensembles can be synchronously active

Although our results demonstrate that LC ensembles are distinct from one another and activate with largely non-overlapping time courses that contain numerous highly variable firing pauses, it does not preclude the possibility that LC ensembles co-activate. Examples of this in LC data can be seen in Figure 3.3B (e.g., brown and red lines at $t = 0.5$ s). The occurrence of ensemble co-activation is important to quantify because such ensemble population activations would be more like the en masse firing evoked in LC stimulation studies that have been used to define the role of the LC in modulating cortical state (Marzo, Nelson K Totah, *et al.*, 2014; M Steriade *et al.*, 1993; Carter *et al.*, 2010; Hayat *et al.*, 2020).

We computed the cross-correlograms between the activation time courses of each ensemble-pair and quantified both the number of ensemble-pairs with significant (positive) peaks of cross-correlation and the lag of the cross-correlogram highest peak for those ensembles. We found that 506 of 790 ensemble-pairs (64%) had significant cross-correlogram peaks. An example significant peak at zero-lag is shown in Figure 3.7A. We found that most of the significant peaks occurred at zero-lag (Figure 3.7B). Out of 506 ensemble-pairs with significant cross-correlation peaks, 420 (83%) had a zero-lag peak. In the overall population of 790 ensemble-pairs, synchronous co-activation was observed among 53% of ensemble-pairs. This result suggests that although ensembles are distinct, a large proportion of ensemble-pairs can co-activate.

To measure how frequently ensemble-pairs synchronously co-activate, we calculated a zero-lag synchronization index for each of the 420 ensemble-pairs with a significant zero-lag cross-correlogram peak. This index quantifies the percentage of activation instances of an ensemble that were zero-lag co-activations with another ensemble. The average synchronization index was 28% with a range of 3% to 59% (Figure 3.7B, inset, $N = 420$ ensemble-pairs). Importantly, the remaining 47% of ensemble-pairs (370 out of 790) never co-

activated (no zero-lag peak in the cross-correlogram). Overall, and contrary to the standard view that the LC neuronal population fires en masse with a high level of synchrony, these analyses show that LC ensembles have ensemble synchronous co-activations, but this happens only approximately for half of the ensembles which synchronously co-activate on average approximately one-quarter of times. Overall, for the most part, ensembles dynamics are non-overlapping.

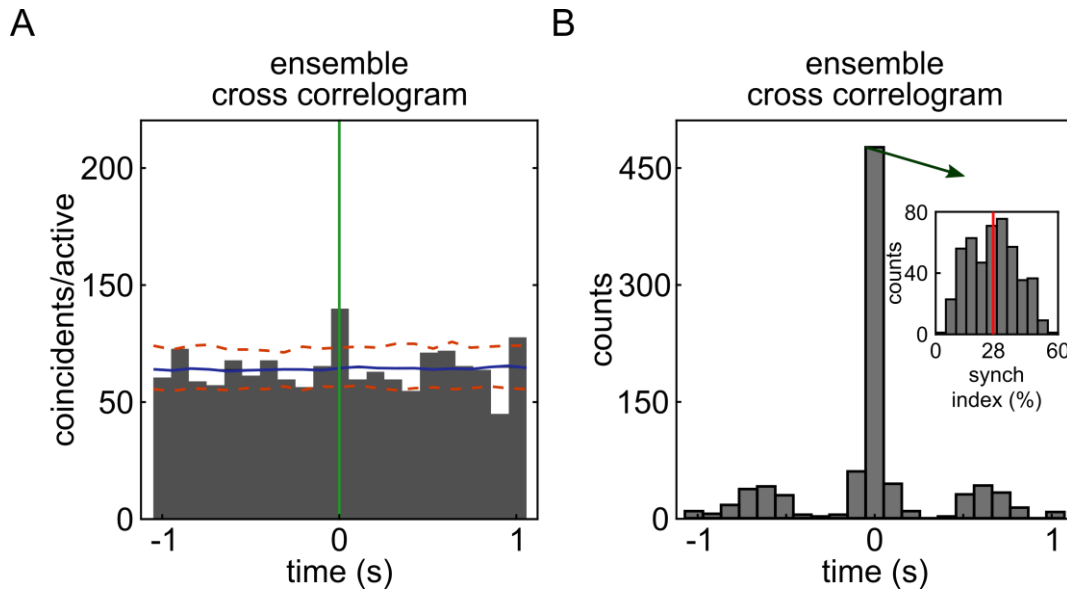


Figure 3.7 Peaks of cross-correlograms between the activation times of ensemble-pairs. (A) Histogram of the cross-correlogram (time bin 100 ms) of the activation time course of an example ensemble-pair (ensembles #1 and #2 from rat 1052) with a significant zero-lag cross-correlation peak. The activation time of the reference ensemble is at $t = 0$ s (green line). Significant peaks were defined as those that had cross-correlogram values above the 99th percentile (upper dashed orange line) of the surrogate distributions of correlogram values computed by randomly jittering ensemble activation times. The solid blue line shows the average of the surrogate correlograms. **(B)** The histogram shows the number of ensemble-pairs with a significant cross-correlogram peak as a function of time lag. Most peaks occur at zero-lag. The inset presents a histogram of synchrony index values for the 420 ensemble-pairs that had significant zero-lag cross-correlogram peaks.

3.3.5 Spontaneous activation of distinct LC ensembles is associated with different cortical states

The largely non-overlapping dynamics of individual LC ensembles may enable distinct ensembles to evoke different cortical states. Alternatively, all ensembles may promote the stereotypical activated state often imputed to LC activation (Harris and Thiele, 2011; McCormick *et al.*, 2020; McGinley *et al.*, 2015; Marzo, Nelson K Totah, *et al.*, 2014; Hayat *et al.*, 2020; Carter *et al.*, 2010). We

disambiguated between these two possibilities by characterizing cortical state around the time of spontaneous LC ensemble activations.

We aligned the cortical area 24a LFP to the times of spontaneous activation of individual LC ensembles. For this analysis, NMF identified 89 ensembles in 9 rats from which cortical LFPs and LC population activity were simultaneously recorded. We calculated both the LFP spectrogram and the band-limited power (BLP) in five canonical frequency bands (θ , 4-8 Hz; α , 8-12 Hz; β , 12-30 Hz; γ , 30-70 Hz; high γ , 70-150 Hz) analyzing data from a 900 ms window aligned to spontaneous activation of each LC ensemble. This window comprised 400 ms before the beginning of ensemble activation, 100 ms of ensemble activation, and 400 ms after the end of ensemble activation. This window was chosen for two reasons. First, it provided a good tradeoff between temporal and spectral resolution. Second, our previous analyses of cross-correlations and durations of activation and activity pauses show that it is unlikely that multiple ensembles were co-active during this window (Figure 3.3C, Figure 3.7B). Therefore, this window ensured that changes in the cortical LFP spectrum were predominantly related to activation of an individual ensemble in the LC. We averaged the BLP and the spectrogram for each ensemble over all instances of its activation. To compare spectrograms and BLP across ensembles, we normalized them using a spectral modulation index, which quantifies the relative changes of power around the time-averaged power in each frequency bin.

Visual inspection of individual examples of BLP aligned to LC ensemble activation revealed diverse patterns of modulations in cortical BLP around the ensemble activation time, depending on which ensemble was active (Figure 3.8A). Importantly, BLP modulations averaged over the 400 ms after spontaneous activation of each ensemble were larger than those obtained when recomputing surrogate BLP modulations after randomly shuffling the ensemble activation times (Figure 3.8B). The scatter plots showing the changes in BLP revealed a structure within the large diversity of power changes associated with individual ensembles (Figure 3.8B). After spontaneous activation of approximately half of the ensembles

there was a relative decrease a cortical power both in the low (θ) and in the high (γ , high γ) frequencies with respect to pre-activation power. On the other hand, for approximately one quarter of the ensembles, there was a relative decrease of low-frequency power and an increase of high-frequency power, similar to the cortical activated state observed after external stimulation of the LC. Relative increases of both low-frequency and high-frequency power as well as relative increases of low-frequency power but decreased high-frequency power were also observed after activation of smaller proportions of ensembles.

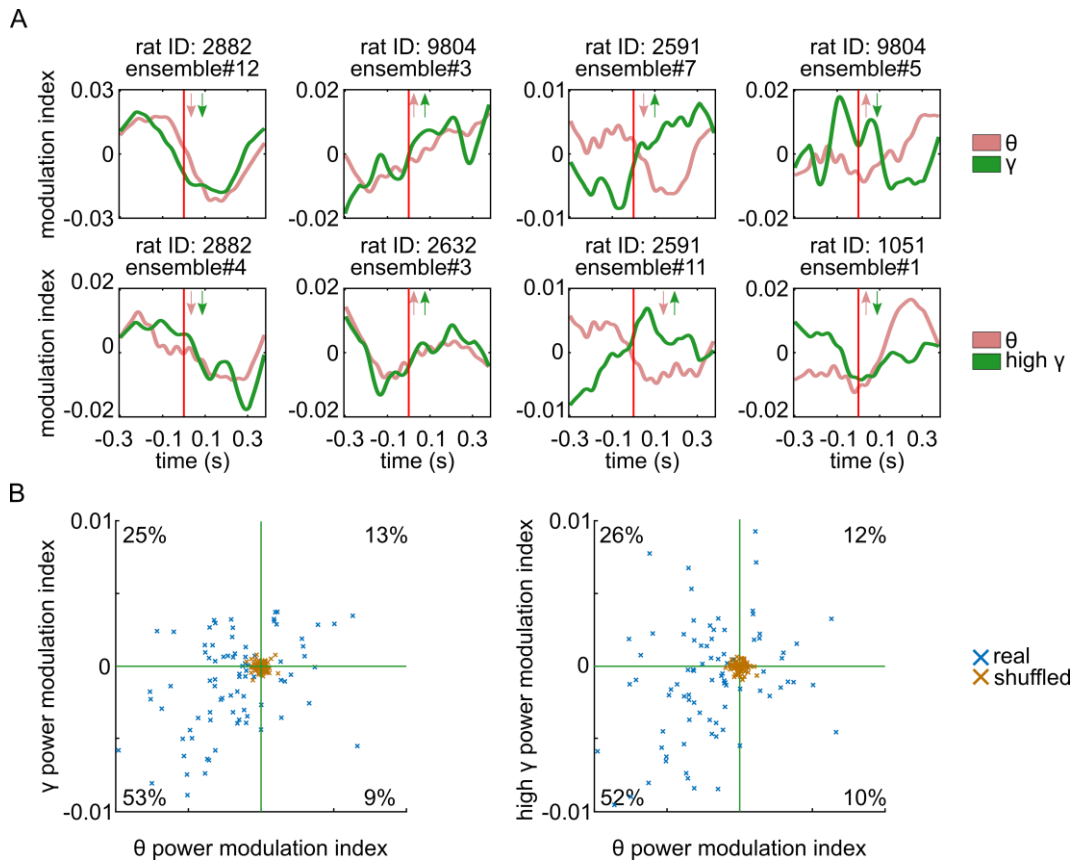


Figure 3.8 Modulations of cortical LFP BLP aligned to spontaneous activation of LC ensembles.

(A) Examples of BLP (calculated using the spectrogram modulation index) for different ensembles. The upper row shows θ band (red) and γ band (green) cortical BLP in a window around ensemble activation onset (marked by a vertical red line) for 4 example ensembles. Inset arrows indicate whether time-averaged power each band increased or decreased after the ensemble was active relative to the pre-ensemble-activation window. The lower row shows the θ band (red) and high γ band (green). Plotting conventions are identical to upper panel. **(B)** Scatter plots show the time-averaged BLP 400 ms after spontaneous ensemble activation. Each blue data point is an ensemble ($N = 89$). The left plot shows θ band versus γ band. The right plot shows θ band versus high γ band. The percentages indicate the percent of ensembles (blue crosses) in each quadrant. The green line indicates 0 on each axis. Brown crosses represent surrogate (shuffled) BLP modulations obtained by recomputing BLPs after randomly shuffling the times of ensemble activations.

Similar trends were found when considering individual examples of spectrograms computed around ensemble event activations (Figure 3.9, Figure 3.10). Considering spectrograms is useful because it gives more detailed spectral information than BLP. To capture typical trends in the cortical spectrograms (from 4 Hz to 150 Hz) across LC ensembles (N = 89), we clustered the spectrograms calculated in the same peri-ensemble-activation window considered above for BLP. This analysis found 4 predominant spectrogram types with different trends in spectrotemporal modulations. We chose 4 clusters by first varying the putative number of clusters from 1 to 22 and quantifying the diminishing returns of adding each additional cluster (Figure 3.11). Critically, only one of these spectrogram types (cluster 1, Figure 3.9A, associated with activation of 28% of the ensembles) had a spectral change characterized by a relative increase in high-frequency power and a relative decrease of low-frequency power, from before to after LC ensemble activation, which resembled the stereotypical activated cortical state observed after electrical or optogenetic stimulation of the LC (Marzo, Nelson K Totah, *et al.*, 2014; M Steriade *et al.*, 1993; Carter *et al.*, 2010; Hayat *et al.*, 2020).

Another spectrogram type (cluster 2, associated with activation of 23% of the ensembles) was characterized by an overall relative increase in oscillatory power across all frequencies after ensemble activation, as well as broadband decrease just prior to and during ensemble activation. Two others (clusters 3 and 4, associated with activation of 24% and 25% of the ensembles, respectively) showed a relative decrease of power across all frequencies above the θ band. Cluster 3 was also accompanied by a brief increase in high-frequency power during ensemble activation.

The patterns seen with the clustering of the spectrograms in Figure 3.9A recapitulate reasonably well the major different behaviors found across all individual ensembles as shown by the distribution of relative modulations of BLP in Figure 3.8. For instance, half of ensembles show a relative decrease of BLP power across all frequencies after ensemble activation (lower left quadrants in Figure 3.8B), matching well the finding of 2 out of 4 spectrogram clusters with a

generalized relative power decrease after ensemble activation (Figure 3.9A). It is important to note that the four spectrogram clusters do not indicate that those were the only kind of state transitions happening, rather they represent the centroids of the most common trends recapitulating predominant behaviors.

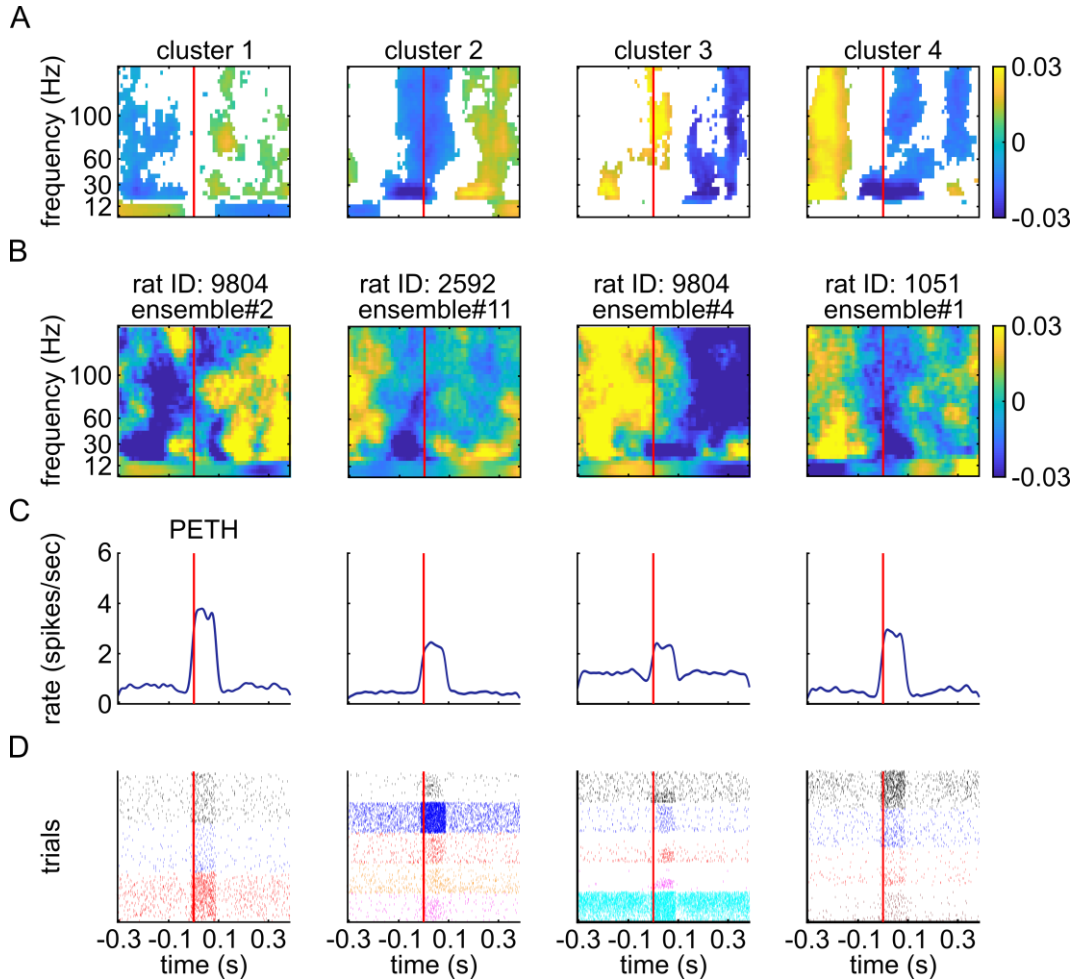


Figure 3.9 Modulations of cortical LFP spectrograms aligned to spontaneous activation of LC ensembles. (A) The average across all spectrograms within each cluster aligned to ensemble activation time (red line). Significant modulations are in color and non-significant values are white. Significance of spectrogram modulations of cluster centers was computed as described in Methods. (B) The ensemble activation-aligned spectrogram for an example ensemble from each cluster. Plotting conventions are the same as in A. (C, D) For each example ensemble in B, the PETH of its population spike rate panel C and the spike rasters of single units in the ensemble are plotted around spontaneous activation of the ensemble (red lines). In all panels, we plotted data in a peri-ensemble activation window from 300 ms before to 400 ms after ensemble activation onset because the spectrograms were estimated in sliding windows whose center all fell within this window.

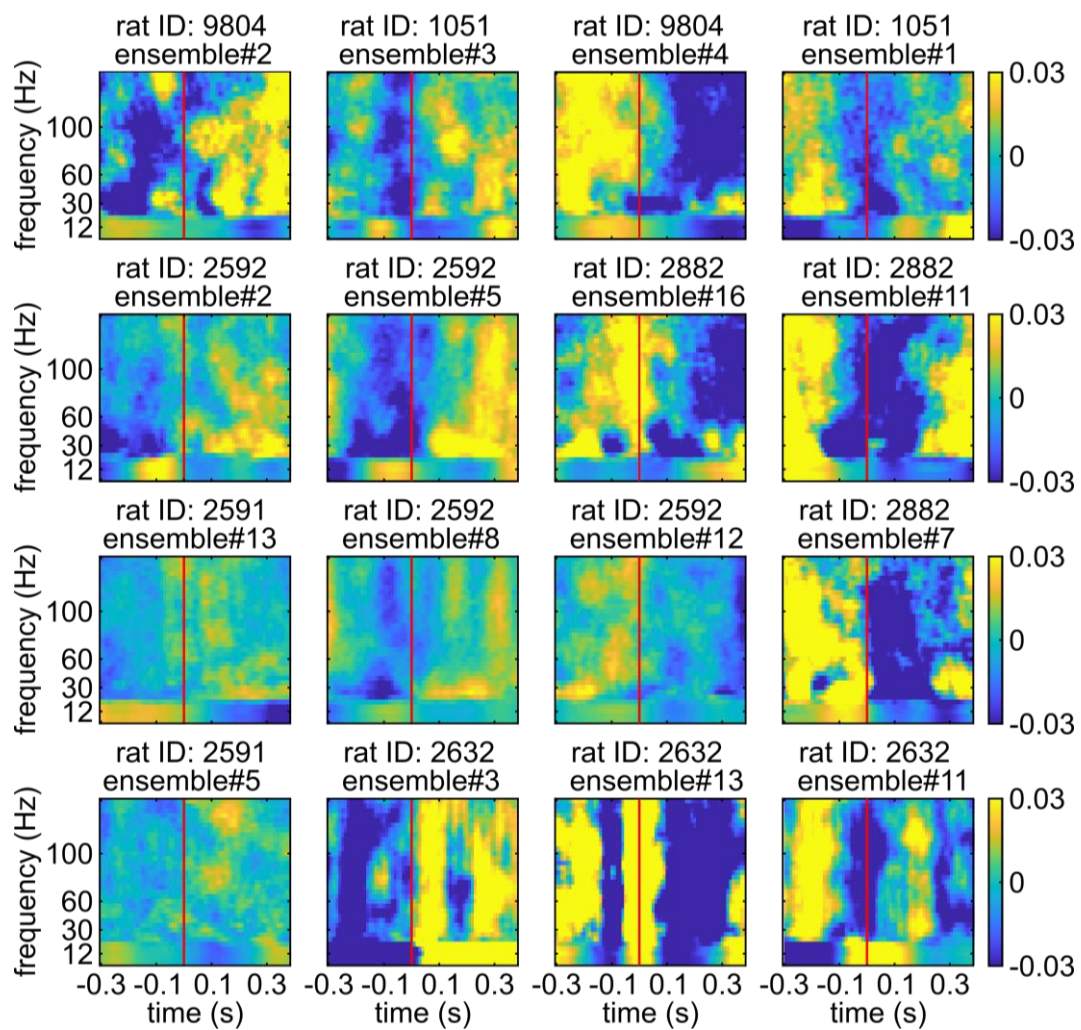


Figure 3.10 Examples of cortical LFP power spectrograms aligned to spontaneous activations of individual LC ensembles. Examples from 12 different ensembles illustrate the diverse cortical states which occur around the time of ensemble activation. The examples are shown in 4 columns, with each column reporting spectrograms that were assigned respectively to the clusters 1, 2, 3, and 4 shown in the Figure 3.9

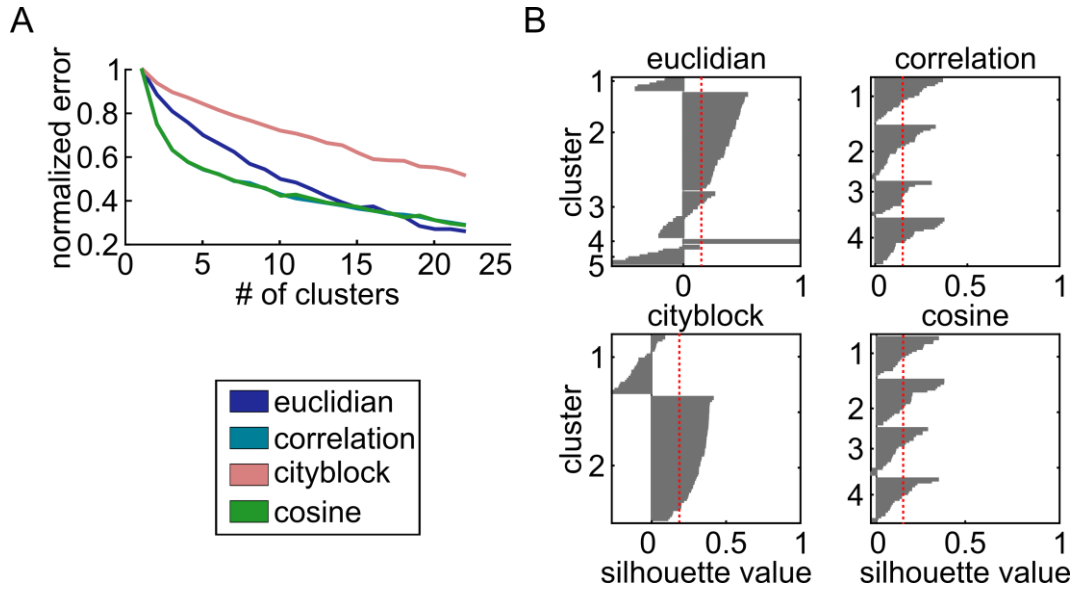


Figure 3.11 The result of analyses supporting the determination of the best criteria for spectral clustering. (A) The normalized error (error divided by the maximum error) of the k-means clustering of the ensemble activation-aligned spectra versus the number of clusters. Four different distance measures were assessed and each is plotted in a different color. (B) Each panel shows the result of the silhouette analyses on the chosen number of clusters for four different distance measures. The optimal distance was selected based on both the uniformity in each cluster (the width of the bar plots) and the average silhouette value (the dashed red line).

We next assessed whether firing properties differed between distinct groups of ensembles associated with the 4 cortical spectrogram clusters (Figure 3.12). We first characterized the strength of ensemble activation and found that it differed across the ensembles associated with the 4 spectrogram clusters. The population spike rate was averaged across all ensemble activation events and all single units in the ensemble. The peak of the resulting population spike rate PETH was used to characterize the activation strength of the ensemble. We found that the median activation strength across ensembles associated with each cortical spectral cluster differed (Kruskal-Wallis test, $p = 0.0003$, $\omega^2 = 0.9634$, $\chi^2 = 18.8899$, $N = 89$ ensembles). Post-hoc tests showed that cluster 1 differed from clusters 2 and 3 (Figure 3.12A). We also examined the ensemble activation strength by first averaging across ensemble activation times to obtain a PETH for each single unit separately, and then averaging across single units. Activation strength of the ensemble was the peak of the single unit averaged PETH. The median activation strength across ensembles in each cortical spectral cluster type again differed (Kruskal-Wallis test, $p = 0.0008$, $\omega^2 = 0.9869$, $\chi^2 = 16.8530$, $N = 89$ ensembles).

Activation strength differed between clusters 1 and 3 and clusters 1 and 4 (Figure 3.12B). Regardless of how ensemble activation strength was assessed (Figure 3.12 A, B), ensembles associated with spectral cluster 1 were more strongly active than ensembles associated with other clusters. Finally, we examined whether the size of the ensemble differed across cortical spectral clusters. The median number of units across ensembles differed across clusters (Kruskal-Wallis test, $p = 0.0012$, $\omega^2 = 0.9618$, $\chi^2 = 15.8187$). Post-hoc tests showed that cluster 1 had fewer units than cluster 3 (Figure 3.12C). In summary, ensembles associated with cluster 1 spectra (“activated state”) had smaller size and stronger spontaneous activations than other ensembles.

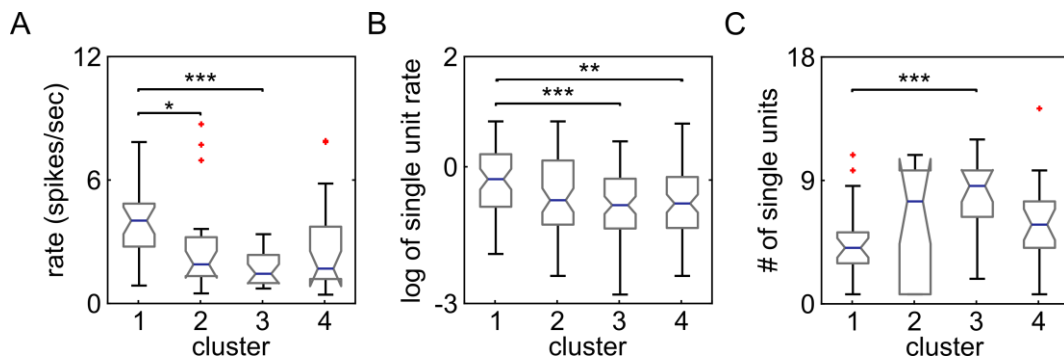


Figure 3.12 The firing properties of LC ensembles associated with each cortical spectrogram cluster. (A) Boxplots of ensemble activation strength in each spectrogram cluster calculated using the peak of the ensemble population firing rate PETH. (B) Boxplots of ensemble activation strength in each spectrogram cluster calculated using the single unit averaged firing rate PETH. Due to the skewness of the single unit firing rate distributions, we plot log-transformed data. (C) Boxplots of the number of single units within the ensembles for the different spectrogram clusters. In all panels, significance is indicated by post-hoc tests: * - $p < 0.05$, ** - $p < 0.01$, *** - $p < 0.001$.

3.3.6 Synchronous spontaneous activation of a larger pool of LC ensembles results in a more homogeneous cortical state

These data demonstrate a relationship between distinct LC ensembles and cortical states. This finding stands in marked contrast to the stereotypical activated state evoked by electrical or optogenetic stimulation that synchronously activates LC neurons. Therefore, we predicted that when several LC ensembles are co-active (a situation that may resemble more the stimulation-evoked en masse LC activation than when considering only the activation of an individual ensembles), the associated cortical states should include more frequently the activated state and

become more homogenous. We took advantage of our observation that ensemble-pairs can sometimes become co-active (Figure 3.7B). We assessed the cortical LFP spectrograms, as in Figure 3.9A and B, but aligned spectrograms to spontaneously occurring co-activation times of ensemble-pairs. A total of 199 ensemble-pairs, which had a significant zero-lag cross-correlogram peak, were simultaneously recorded with cortical LFP. In contrast to the 4 spectrogram types observed around the time of spontaneous activation of individual LC ensembles, clustering now revealed only 2 spectrogram types at the time points when ensemble-pairs became synchronously co-active, suggesting a reduced diversity with respect to the individual ensemble analysis (Figure 3.13). One cluster is the stereotypical activated cortical state (cluster 2), which included more than half (101 of 199) of the ensemble-pairs, suggesting a larger proportion of activated states associated with spontaneously occurring co-activation of different ensembles in comparison to when individual ensembles were active. The other cluster is characterized by a relative decrease of spectral power across all bands (98 of 199 ensemble-pairs). In sum, when two LC ensembles are co-active, such that LC population activity becomes more similar to en masse LC activation, the modulation of cortical state is more homogenous and presents a higher proportion of relative cortical power changes that are similar to the LC stimulation-evoked cortical state change (Marzo, Nelson K Totah, *et al.*, 2014; Hayat *et al.*, 2020; Carter *et al.*, 2010; M Steriade *et al.*, 1993).

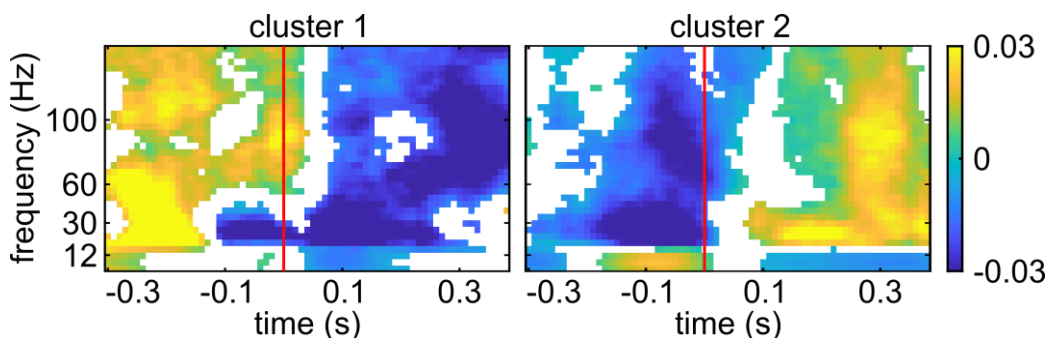


Figure 3.13 Modulations of cortical LFP spectrograms aligned to spontaneous co-activation of LC ensemble-pairs. The spectrograms are aligned to the co-activation times of ensemble-pairs that had a significant zero-lag cross-correlation peak. The onset of ensemble-pair co-activation is indicated by the red line. The resulting spectra clustered into 2 types. Each plot shows the average spectrogram across all ensemble-pairs associated with each cluster. Only significant changes in the power spectrum are plotted in color and non-significant modulations are white.

3.4 Discussion

Cortical states vary over a wide range and are in a tight relationship with many functions that are relevant to psychiatric disorders, such as sleep, arousal, perceptual ability, and reaction times. It is thus no surprise that there have been long-standing efforts to understand the neural factors contributing to cortical state fluctuations (Harris and Thiele, 2011; McGinley *et al.*, 2015; McCormick *et al.*, 2020). However, the neuronal interactions that control cortical states remain largely elusive. Blocking out the effect of the external world (e.g., slow wave sleep or anesthesia) has proven to be a successful approach for dissecting the spontaneous brain-internal neuronal interactions that control cortical state (Haider and McCormick, 2009). These approaches have been used to demonstrate that the LC evokes transitions to, and maintenance of, a single and unitary activated state in the cortex (Marzo, Nelson K Totah, *et al.*, 2014; Hayat *et al.*, 2020; Carter *et al.*, 2010; M Steriade *et al.*, 1993). However, rather than studying the spontaneous emergence of cortical states due to LC activity, these studies have used electrical or optogenetic stimulation of the LC, which evokes en masse LC population activity.

Here, we considered the effect of spontaneously occurring events of LC ensemble activations. Using synthetic spike trains with different ground truth patterns of ensemble activity, we illustrate that NMF can detect the precise composition of ensembles, even when multiple ensembles occasionally co-activate or when neurons participate in multiple ensembles. By applying this methodology to LC population activity, we decomposed this spontaneous activity into multiple, separate neuronal ensembles. This enabled us to study quantitatively the spontaneous interactions between LC neurons and cortical states and contribute to long-standing efforts to understand the how cortical state might be generated (Harris and Thiele, 2011; McGinley *et al.*, 2015; McCormick *et al.*, 2020). We demonstrated that ongoing cortical state differs depending upon which LC ensemble was spontaneously active. We observed significant power variations

around the activation times of LC ensembles. This result is consistent with the broad afferent input that the LC receives from the forebrain, which predicts that cortical states may affect individual LC ensembles and be affected by them. Importantly, these findings establish that LC ensembles do not simply evoke a stereotypical activated state in the cortex. Thus, the temporally diverse and largely non-overlapping nature of spontaneous LC ensemble activations correspond to a diversity of cortical states. When LC ensemble-pairs become synchronously co-active, which is a situation more similar to the highly synchronized and en masse LC population activation driven by LC stimulation (Marzo, Nelson K Totah, *et al.*, 2014; Hayat *et al.*, 2020; Carter *et al.*, 2010; M Steriade *et al.*, 1993), the diverse set of cortical states had a higher proportion of the stereotypical activated state that has been uniformly observed across these prior studies using LC stimulation. Co-activation of ensemble-pairs, or multi-ensemble ‘collectives’, may provide transient global norepinephrine release. These global events may occur in response to specific, structured afferent input in specific moments during anesthesia, sleep, or wakefulness that demand more homogenous noradrenergic neuromodulation.

The types of cortical states modulations on a sub-second scale around spontaneous activations of LC ensembles that we documented here happened within the broader context of two longer (minutes) cortical states that occur during urethane anesthesia (Clement *et al.*, 2008; Neves *et al.*, 2018). The predominant urethane-associated cortical state consists of slow waves and an LFP power spectrum that strongly resembles that of non-REM slow wave sleep. This slow wave state is punctuated by continuously ‘activated’ epochs that are devoid of slow waves, enriched with beta and gamma oscillations, and thus loosely resemble cortical activity during wakefulness. Our findings show that, even in the context of these continuous states, there are multiple sub-states that emerge when one examines cortical activity around brain-internal neuronal events, such as spontaneous LC ensemble activations. Employing our analytic methodology during sleep or wakeful behavior may reveal many diverse cortical sub-states

associated with LC ensemble activations. These studies will require novel tools for recording LC ensembles in non-anesthetized animals.

3.4.1 Potential neurophysiological causes of the diversity in cortical state

Neuromodulation of different forebrain regions may alter the brain-internal neuronal interactions that produce various cortical states. LC neurons are broadly-projecting, but also have localized projections to the forebrain and release a range of neurotransmitters (Totah *et al.*, 2019; Chandler *et al.*, 2019); therefore, LC ensembles that project to different forebrain neuronal networks could affect how those networks self-organize cortical states. When considering how distinct LC ensembles could promote different cortical states, two potential factors for future study are the diversity of ensemble neurochemical make-up and/or its projection profile. Given that the region in which we assessed cortical state (area 24a) receives projections from approximately 61 to 65% of LC neurons in the rat (Chandler *et al.*, 2014; Chandler *et al.*, 2013), it seems likely that most ensembles project to area 24a and they should, therefore, produce a similar state change. Our finding to the contrary could be explained by the possibility that the neurochemical make-up of the LC neurons differs across ensembles and results in cortical state diversity. Another possibility is that despite most ensembles presumably sharing area 24a as a projection target, it is the other targets that are potentially not shared across ensembles, which leads to LC ensemble-specific cortical states in 24a. According to this forebrain ‘network’ perspective, LC ensembles associated with different cortical states could have divergent axon collaterals which enable the ensembles to modulate distinct forebrain neuronal networks that are associated with different cortical states. Ensembles associated with the activated cortical state were smaller and fired more strongly. Smaller ensembles may have less diffuse projections and, with a higher spike rate, they may release larger amounts of norepinephrine or have increased likelihood of

releasing other neurotransmitters that could be associated specifically with the activated cortical state.

3.4.2 An LC ensemble code enables greater diversity in neuromodulatory functions

Behavioral and mental states fluctuate widely from moment to moment and it has been known since the advent of EEG recordings that such diverse cognitive-behavioral states are associated with a multitude of cortical states (Harris and Thiele, 2011; McGinley *et al.*, 2015; McCormick *et al.*, 2020). The brain-internal interactions that generate this large state-space are still largely unknown. LC neurons were classically thought to modulate cortical and thalamic neuronal excitability level using noradrenergic “tone” (Waterhouse and Woodward, 1980; McCormick, 1992; Devilbiss, 2004), whereas the neuronal interactions that produce the cortical state are contained within the cortex and thalamus (Hay *et al.*, 2021; Mircea Steriade *et al.*, 1993). According to this standard view, the role of the LC has been to modulate or predispose cortico-thalamic circuits toward the activated cortical state (and predispose the organism toward wakefulness), but the actual neuronal interactions that select cortical state are between cortex and thalamus. However, this standard view of cortical state generation was developed using methods that artificially activated the LC neuronal population en masse using external stimulation. Here, we studied the spontaneously self-organized neuronal interactions which are internal to the brain to reveal that, in contrast to this classical thinking, distinct LC ensembles can promote diverse cortical states. Each ensemble in this small population of ~1,600 brainstem noradrenergic neurons may individually be a key player in selecting ongoing cortical state from a multitude of possibilities. Thus, our findings shift the role of the LC from ‘modulator / promoter’ of a single cortical state toward a ‘selector / controller’ from a large subset of cortical states.

Our results imply that a single brainstem nucleus can perform different neuromodulatory functions by simply changing the groups of neurons that fire.

Critically, these neuromodulatory dynamics can rapidly change on timescales relevant to flexible and ever-changing cognitive-behavioral states. The distinct LC ensembles with nuanced activation dynamics shown here substantially enrich the kind of functions that are currently attributed to brainstem nuclei.

4 GENERAL DISCUSSION

In this final chapter, we consider more implications and perspectives about the research I performed in this Thesis. Since a thorough discussion of each specific project has been given in their respective chapter, here we focus more on concluding and explaining potential ways to further our research and on synthesizing the concepts arising from these two studies.

In the first study (Rocchi *et al.*, 2022), we demonstrated that chemogenetic silencing of the PFC removed the spiking activity that was not phase-locked to the peak of slower oscillatory rhythms (<4 Hz) which resulted in an increase of power in such bands. Similarly, we observed an increase of coherency in these rhythms between areas in the default mode network that demonstrated overconnectivity in the rs-fMRI.

One interesting result was the observed relation between the strength of rs-fMRI functional connectivity and interareal coherency in low frequencies. This can advance our knowledge of understanding how rs-fMRI functional connectivity is reflected in brain electrical oscillatory rhythms and additionally provide some insights into how different brain regions communicate. Several other studies (He *et al.*, 2008; Pan *et al.*, 2013; Lu *et al.*, 2007; Lu *et al.*, 2014) have also found a strong relation between slow rhythms and rs-fMRI activity (Rocchi *et al.*, 2022). Since (Rocchi *et al.*, 2022) demonstrates the ability to causally manipulate rs-fMRI functional connectivity, we can investigate this link even further by correlating the coherency in different LFP bands and rs-fMRI connectivity under multiple different experimental conditions. The first step can be achieved by expanding the experiments demonstrated in Figure 2.13, by performing simultaneous electrophysiological recordings in the areas that demonstrated rs-fMRI underconnectivities and investigating how these underconnectivities are reflected in the oscillatory signals. Understanding the neural mechanisms underlying these phenomena will bring us one step closer to finding a unified theory that explains the role of electrical oscillations in shaping rs-fMRI connectivity.

A second specific advance that could be made in this regard is to consider directional, rather than non-directional, measures of functional interactions between oscillatory signals or rs-fMRI signals at different locations. Our previous work (Rocchi *et al.*, 2022) used only non-directional measures of functional interactions, such as Pearson correlations of spectral coherence, which cannot reveal the principal direction of interaction between sites. The main reason why we could not explore systematically directional measures of functional interactions was that these measures require longer stretches of stationary data, which were not available in our previous datasets due to the complications of the DREADD experiments. As these experimental techniques, will get perfected, it is reasonable to envisage that it would be possible to obtain in the near future longer stretches of data or larger datasets under more stationary conditions. When these new data become available, would also enable us to take advantage of directed communication methods such as Granger causality in the frequency domain (Chen *et al.*, 2006) or Transfer Entropy (Schreiber, 2000). These methods often require more samples to build a firm conclusion compared to coherency. Specifically, using frequency decomposition of conditional Granger causality can provide us with a wider picture of what is the dominant direction of communication in each specific frequency band during baseline (rest), how these directed communications of brain electrical oscillations between regions at each band are changed in each direction due to chemogenetic manipulations, and which of these changes mirrors the changes in the rs-fMRI connectivity. For example, we observed in our data that coherency was strong between the prefrontal cortex and the retrosplenial in slower frequencies and was increased due to manipulation. Applying directional methods, we can gain information about first the dominant directionality of communication (from PFC to Rs or in the opposite direction) and second, how this communication changes with the drug, does it get stronger in both directions, does it increase in the dominant direction only or the opposite?

One limitation in our first study is that they were conducted under anesthesia. It remains of interest to speculate whether the relationship found here between low frequency electrophysiological coherence and fMRI connectivity would hold also in the awake brain. Experiments in Gozzi's lab are ongoing to determine the differences between rs-fMRI dynamics in awake vs anaesthetized mice (Gutierrez-Barragan *et al.*, 2022). One possible difference may arise from the fact that in some regions the power of gamma-band electrophysiological activity is suppressed by anesthesia. While correlations between low frequency electrophysiological coherence and rs-fMRI connectivity has been robustly observed across awake preparations in monkeys (Wang *et al.*, 2012) and mice (Mateo *et al.*, 2017), it is possible that under conditions that evoke higher gamma band activity, rs-fMRI connectivity exhibits a stronger correspondence with the correlation between the low frequency envelopes of electrophysiological gamma band activity. This prediction will be tested in future studies by Gozzi lab.

Recent works have demonstrated the ability to provide detailed mechanistic models of brain electrical oscillations (LFP/EEG) using point-neuron network models (see (Martínez-Cañada *et al.*, 2021) for a full review). These models have provided us with knowledge of methods to infer many neural circuit interactions from electrical oscillations (Martínez-Cañada *et al.*, 2021). Among those interactions, one which is particularly of interest is the ratio between excitation and inhibition (E/I ratio) because it has been suggested that changes in the E/I ratio play a role in some psychiatric disorders such as Autism Spectrum Disorder (ASD) (Sohal and Rubenstein, 2019; Nelson and Valakh, 2015). Some attempts to infer the changes in the E/I ratio from brain electrical oscillations have pointed 1/f slope of the power spectrum as the biomarker that reflects the changes in the E/I ratio (Gao *et al.*, 2017; Trakoshis *et al.*, 2020). However, more recent studies suggest that the changes in the E/I ratio change the spectral properties of the brain oscillations in more than one way (i.e. change in the 1/f slope) (Martínez-Cañada *et al.*, 2021). Given that the manipulations in (Rocchi *et al.*, 2022), especially the ones presented in Figure 2.13 disrupts the natural E/I balance, they can be used

to validate and further develop a model to infer more biomarkers of change in the E/I ratio. Having a model that can predict the changes in the E/I ratio from the power spectrum of brain electrical oscillations can be used on EEG (or LFP) recordings which consist of control typical subjects (or animals) and ASD subjects (or animal models of ASD) to check whether these models can be used for classifications between two groups. This is of great interest because the EEG signal has already demonstrated the potential for the detection of ASD (Bosl *et al.*, 2018; Eldridge *et al.*, 2014; Gabard-Durnam *et al.*, 2019). Having a more sophisticated method to infer parameters such as E/I ratio from mass oscillatory signals would enable us to study in more detail and more systematically neural changes during the development of illnesses such as ASD. Ongoing work is now being made in our laboratory to address these issues (check FENS 2022 abstract named Model-Based inference of changes in cortical circuit parameters using recordings of neural mass activity, <https://kenesvm.azureedge.net/public/general/FENS2022.pdf>).

Our first study (Rocchi *et al.*, 2022) concluded by proposing a hypothesis trying to explain our observations (Figure 2.16). A simple explanation can be that the administration of the drug suppressed the contributions from fast local processes but kept the contributions that arise from slow global fluctuations. This resulted in decreased interactions in the high frequency while increasing its low-frequency part. Since the rs-fMRI connectivity has been suggested to also reflect slow covariations of brain electrical oscillations (He *et al.*, 2008; Pan *et al.*, 2013; Lu *et al.*, 2007; Lu *et al.*, 2014), this simple explanation can justify our findings. However, this is puzzling, due to the fact that gamma oscillations have been suggested to modulate both within/between brain areas (Siegel *et al.*, 2012; Belitski *et al.*, 2008; Donner and Siegel, 2011; Mazzoni *et al.*, 2011; Kayser and König, 2004; Frien *et al.*, 2000; Pesaran *et al.*, 2002; Martínez-Cañada *et al.*, 2021). Biophysical simulations also validate the role of gamma in neuronal communication (Martínez-Cañada *et al.*, 2021). In addition, a significant number of studies have demonstrated that local BOLD fluctuations correlate strongly with the gamma band (Logothetis *et al.*, 2001; Kayser, 2004; Niessing *et al.*, 2005; Goense and Logothetis, 2008; Murayama

et al., 2010; Schölvinck *et al.*, 2010; Magri *et al.*, 2012; Scheeringa *et al.*, 2009) supported by simulation studies (Martínez-Cañada *et al.*, 2021; Trakoshis *et al.*, 2020). However, why covariations of rs-fMRI between different sites reflect covariations of slow brain electrical oscillations is largely unexplained. This requires new simulations of interacting networks that manage somehow to introduce these slow global covariations.

Brain states occur and change on multiple time scales. The exact neural mechanisms which control these fluctuations are not yet fully understood. However, much research has been dedicated to understanding them (Harris and Thiele, 2011; McCormick *et al.*, 2020). Here, in our second study (Noei *et al.*, 2022) we explored the relation of LC as a part of the neuromodulatory systems with fluctuations of cortical states in the PFC of rats under anesthesia. Instead of looking at the stimulated activity of LC due to manipulations, we decomposed the ongoing LC population activity using NMF that in addition to the detection of ensembles, can resolve their activity over time. This enabled us to relate the activity of different ensembles with the ongoing rhythms of the PFC. Our findings demonstrated that cortical states differ depending on which ensemble is active and thus this can provide evidence for LC to potentially be able to modulate the cortical state in more than one way. The advantage of studying LC activity under electric/optogenetic stimulation is that it can establish a causal link between LC activity and observed brain/behavior state changes. For example in (Breton-Provencher *et al.*, 2022) the authors have demonstrated that optogenetic inactivation of noradrenaline neurons in LC would cause impairments in task execution. However, the disadvantage is that the elicited patterns of activity may be unnatural and they can point to misleading results such as the perceived belief of LC activation causes only an activated state in the brain. The advantage of our results is that it shows nuanced patterns of LC activity and several possible cortical states associated with them. However, we lack any causal proof about the role they play. A study using 2-photon optogenetics with single-cell resolution (Panzeri *et al.*, 2017; Gill *et al.*, 2020) can potentially bridge that gap by creating similar

ensemble patterns in LC artificially and causally probing their effect on brain state and even behavior. Methods such as NMF would be a necessity for the online detection of ensembles and resolving their activity over time.

PFC (area 24a) receives projections from ~65% of LC cells in rats (Chandler *et al.*, 2014; Chandler *et al.*, 2013), and thus, is an appropriate area to examine the relation between LC ensembles and forebrain. It has been demonstrated that different subregions of the PFC such as Orbitofrontal Cortex (OFC), medial PFC and anterior cingulate cortex (ACC) receive dense, yet largely non-overlapping input from the LC (Chandler *et al.*, 2014). Aside from the PFC, LC units project to many different brain regions. Although not as dense as PFC, M1 also receives input from ~ 40% of LC cells which are largely non-overlapping with the prefrontal projecting ones (Chandler *et al.*, 2014). Viral-genetic tracing of the LC units, has also revealed that other areas such as olfactory bulb, somatosensory cortex, auditory cortex and hypothalamus all receive significant dense input from LC (Schwarz *et al.*, 2015). Given different local connectivity and different functions of these regions, studying LC ensemble relation to the activity of these regions can unveil a lot about the role of LC. However, fluctuations of ongoing cortical activity are more complicated to be captured by recordings only from a single site. Studies have tried to capture the dynamics of these fluctuations using fMRI in anesthetized (Gutierrez-Barragan *et al.*, 2019) and awake (Gutierrez-Barragan *et al.*, 2022) mice and using calcium imaging data in anesthetized mice (Saxena *et al.*, 2020; MacDowell and Buschman, 2020). All these studies propose that spontaneous activity can be described using a few recurring states. We can expand our work by trying to apply similar methods to identify these states in spontaneous brain activity of rats under the similar experimental conditions of our study using whole-brain EEG/ECOG recordings. Since it has been demonstrated that spontaneous behaviors are reflected in the brain's ongoing activity (Stringer *et al.*, 2019), identifying these states enables us to correlate them with behavior. Some of these behaviors (such as a change in pupil diameter) can work as a proxy for LC activity (Reimer *et al.*, 2016), and thus can link LC activity to more thoroughly investigated

brain states. Additionally, possible simultaneous recording of LC single cells and whole-brain EEG/ECOG would allow us to move from matrix to tensor decomposition methods by creating artificial trials aligning LC single-unit activity to these states. Tensor decomposition methods such as tensor component analyses (Williams *et al.*, 2018) or non-negative tensor decomposition (Onken *et al.*, 2016) can outperform matrix decompositions, especially in cases of flat matrices (for example when the recording time is much longer than the number of units). Using this procedure can empower us with the knowledge of not only decomposing the spatiotemporal pattern of LC population activity but also knowledge about how these patterns change across different cortical states in a wider sense.

A previous study has demonstrated that including firing properties of LC, can increase the capability of dynamical models in predicting cortical state dynamics (Safaai *et al.*, 2015). However, this study has utilized the multi-unit activity of LC as an input to a self-exciting/inhibiting dynamical system. Their results can be potentially enhanced by including the firing rate of different ensembles as inputs to the model. Given that our results demonstrated that different ensemble activities can be associated with different cortical states, including different LC ensembles separately in the model will probably increase the capability of the model in predicting the ongoing activity of the cortex. This is particularly of interest since the results of (Safaai *et al.*, 2015) demonstrated strong relation between LC activity and the cortical delta rhythm, and our results in (Rocchi *et al.*, 2022) demonstrated a strong relationship between delta coherency and rs-fMRI connectivity. There is growing evidence pointing toward the fact that rs-fMRI functional connectivity is not only reflecting direct anatomical connections but can be caused through subcortical pathways such as the thalamus (Gent *et al.*, 2018) or changes in neuromodulatory systems (Munn *et al.*, 2021; Liu *et al.*, 2018). For example, studies have reported that changes in the brain state (from anesthesia to awake (Gutierrez-Barragan *et al.*, 2022) or changes in arousal (Liu *et al.*, 2018)), can shape the spatiotemporal configurations of the rs-fMRI. Since LC is believed

to play a role in controlling the levels of arousal (Carter *et al.*, 2010), having a more sophisticated model that considers different LC ensembles' activity for predicting ongoing cortical rhythms, can significantly enhance our knowledge of understanding the origin of oscillations in the cortex and how it can be related to other measures such as rs-fMRI.

Ever since Caton and subsequently Berger managed to record electrical signals from animals and humans, studying neural oscillations has been of interest. Recent advancements have additionally made it possible to record simultaneously from multiple areas of the brain with good spatial and temporal resolutions. This has enabled researchers to investigate these rhythms, hypothesize their role in brain mechanisms, and design methodology and experiments to validate them. Here, we presented our contributions to studying oscillations and we hope that we have managed to further strengthen our understanding of how the brain works.

LIST OF FIGURES

| | |
|--|----|
| Figure 2.1 Histological validation of electrode placement | 18 |
| Figure 2.2 Chronic inhibition of the mouse PFC results in rsfMRI overconnectivity | 26 |
| Figure 2.3 Overexpression of the potassium channel Kir2.1 in the PFC reduces spontaneous neural activity | 27 |
| Figure 2.4 rsfMRI overconnectivity in Kir2.1 and DREADD-expressing mice persists after global fMRI signal regression. | 27 |
| Figure 2.5 Chemogenetic inhibition of neural firing in the PFC | 31 |
| Figure 2.6 Chemogenetic inhibition of the mouse PFC results in rsfMRI overconnectivity | 32 |
| Figure 2.7 Voxels exhibiting rsfMRI overconnectivity upon chemogenetic inhibition of the PFC are robustly innervated by the PFC..... | 33 |
| Figure 2.8 Chemogenetic inhibition of the mouse PFC under medetomidine-isoflurane anesthesia recapitulates the rsfMRI overconnectivity profile observed in halothane-anesthetized mice | 34 |
| Figure 2.9 The polymodal thalamus is functionally overconnected to cortical areas | 36 |
| Figure 2.10 Whole-brain rsfMRI connectivity in control and hM4Di-expressing mice | 37 |
| Figure 2.11 Chemogenetic inhibition of the PFC reduces γ activity but increases slow oscillatory power | 40 |
| Figure 2.12 A simple simulation of the effect of suppressing neural firing not locked to slow rhythms | 41 |
| Figure 2.13 Chemogenetic inhibition of parvalbumin GABAergic cells and stimulation of pyramidal neurons produce rsfMRI underconnectivity..... | 41 |
| Figure 2.14 Chemogenetic inhibition of the PFC results in increased interareal slow oscillatory coherence..... | 45 |
| Figure 2.15 LFP power spectra and absolute coherence in multi-electrode recordings | 46 |

| | |
|--|----|
| Figure 2.16 A schematic illustration of our findings..... | 47 |
| Figure 2.17 LFP δ -band phase difference between PFC and Rs cortices..... | 47 |
| Figure 3.1 Comparison of NMF versus graph-theoretic analysis for detecting ground-truth ensemble dynamics from synthetic spike trains | 68 |
| Figure 3.2 Data underlying the choice of the optimal number of modules (K) in each rat | 69 |
| Figure 3.3 The characteristics of LC ensembles..... | 73 |
| Figure 3.4 Spike rates of units inside and outside LC ensembles around the time of spontaneous LC ensemble activation.. | 74 |
| Figure 3.5 Ensemble auto-correlogram and ensemble-pair cross-correlogram troughs..... | 75 |
| Figure 3.6 Peaks of cross-correlograms between the activation times of ensemble- pairs..... | 77 |
| Figure 3.7 Modulations of cortical LFP BLP aligned to spontaneous activation of LC ensembles. | 79 |
| Figure 3.8 Modulations of cortical LFP spectrograms aligned to spontaneous activation of LC ensembles. | 81 |
| Figure 3.9 The firing properties of LC ensembles associated with each cortical spectrogram cluster | 84 |
| Figure 3.10 Modulations of cortical LFP spectrograms aligned to spontaneous co- activation of LC ensemble-pairs..... | 85 |

BIBLIOGRAPHY

- Alstott, J., Breakspear, M., Hagmann, P., Cammoun, L., Sporns, O. (2009) Modeling the Impact of Lesions in the Human Brain K. J. Friston, ed. *PLoS Computational Biology*. **5**(6), e1000408.
- Alvarez, V.A., Chow, C.C., Van Bockstaele, E.J., Williams, J.T. (2002) Frequency-dependent synchrony in locus ceruleus: Role of electrotonic coupling. *Proceedings of the National Academy of Sciences of the United States of America*. **99**(6), 4032–4036.
- Arthur, D., Vassilvitskii, S. (2007) K-means++: The advantages of careful seeding. *Proceedings of the Annual ACM-SIAM Symposium on Discrete Algorithms*. **07–09–Janu**, 1027–1035.
- Aston-Jones, G., Bloom, F. (1981a) Activity of norepinephrine-containing locus coeruleus neurons in behaving rats anticipates fluctuations in the sleep-waking cycle. *The Journal of Neuroscience*. **1**(8), 876–886.
- Aston-Jones, G., Bloom, F. (1981b) Nonrepinephrine-containing locus coeruleus neurons in behaving rats exhibit pronounced responses to non-noxious environmental stimuli. *The Journal of Neuroscience*. **1**(8), 887–900.
- Aston-Jones, G., Rajkowski, J., Kubiak, P., Alexinsky, T. (1994) Locus coeruleus neurons in monkey are selectively activated by attended cues in a vigilance task. *The Journal of Neuroscience*. **14**(7), 4467–4480.
- Bastos, A.M., Vezoli, J., Bosman, C.A., Schoffelen, J.-M., Oostenveld, R., Dowdall, J.R., De Weerd, P., Kennedy, H., Fries, P. (2015) Visual Areas Exert Feedforward and Feedback Influences through Distinct Frequency Channels. *Neuron*. **85**(2), 390–401.
- Battiston, F., Amico, E., Barrat, A., Bianconi, G., Ferraz de Arruda, G., Franceschiello, B., Iacopini, I., Kéfi, S., Latora, V., Moreno, Y., Murray, M.M., Peixoto, T.P., Vaccarino, F., Petri, G. (2021) The physics of higher-order interactions in complex systems. *Nature Physics*. **17**(10), 1093–1098.
- Beier, K.T., Kim, C.K., Hoerbelt, P., Hung, L.W., Heifets, B.D., DeLoach, K.E., Mosca, T.J., Neuner, S., Deisseroth, K., Luo, L., Malenka, R.C. (2017) Rabies screen reveals GPe control of cocaine-triggered plasticity. *Nature*. **549**(7672), 345–350.
- Belitski, A., Gretton, A., Magri, C., Murayama, Y., Montemurro, M.A., Logothetis, N.K., Panzeri, S. (2008) Low-Frequency Local Field Potentials and Spikes in Primary Visual Cortex Convey Independent Visual Information. *Journal of Neuroscience*. **28**(22), 5696–5709.
- Benjamini, Y., Hochberg, Y. (1995) Controlling the False Discovery Rate: A Practical and Powerful Approach to Multiple Testing. *Journal of the Royal Statistical Society: Series B (Methodological)*. **57**(1), 289–300.
- Berens, P. (2009) CircStat : A MATLAB Toolbox for Circular Statistics. *Journal of Statistical Software*. **31**(10).
- Bertero, A., Liska, A., Pagani, M., Parolisi, R., Masferrer, M.E., Gritti, M., Pedrazzoli, M., Galbusera, A., Sarica, A., Cerasa, A., Buffelli, M., Tonini, R., Buffo, A., Gross, C., Pasqualetti, M., Gozzi, A. (2018) Autism-associated 16p11.2 microdeletion impairs prefrontal functional connectivity in mouse and human. *Brain*. **141**(7), 2055–2065.
- Besserve, M., Schölkopf, B., Logothetis, N.K., Panzeri, S. (2010) Causal relationships

between frequency bands of extracellular signals in visual cortex revealed by an information theoretic analysis. *Journal of Computational Neuroscience*. **29**(3), 547–566.

Bosl, W.J., Tager-Flusberg, H., Nelson, C.A. (2018) EEG Analytics for Early Detection of Autism Spectrum Disorder: A data-driven approach. *Scientific Reports*. **8**(1), 6828.

Bosman, C.A., Schoffelen, J.-M., Brunet, N., Oostenveld, R., Bastos, A.M., Womelsdorf, T., Rubehn, B., Stieglitz, T., De Weerd, P., Fries, P. (2012) Attentional Stimulus Selection through Selective Synchronization between Monkey Visual Areas. *Neuron*. **75**(5), 875–888.

Bowyer, S.M. (2016) Coherence a measure of the brain networks: past and present. *Neuropsychiatric Electrophysiology*. **2**(1), 1.

Breton-Provencher, V., Drummond, G.T., Feng, J., Li, Y., Sur, M. (2022) Spatiotemporal dynamics of noradrenaline during learned behaviour. *Nature*. **606**(7915), 732–738.

Brooks, J.C.W., Davies, W.-E., Pickering, A.E. (2017) Resolving the Brainstem Contributions to Attentional Analgesia. *The Journal of Neuroscience*. **37**(9), 2279–2291.

Brovelli, A., Ding, M., Ledberg, A., Chen, Y., Nakamura, R., Bressler, S.L. (2004) Beta oscillations in a large-scale sensorimotor cortical network: Directional influences revealed by Granger causality. *Proceedings of the National Academy of Sciences*. **101**(26), 9849–9854.

Busche, M.A., Konnerth, A. (2016) Impairments of neural circuit function in Alzheimer’s disease. *Philosophical Transactions of the Royal Society B: Biological Sciences*. **371**(1700), 20150429.

Buzsáki, G. (2004) Neuronal Oscillations in Cortical Networks. *Science*. **304**(5679), 1926–1929.

Buzsáki, G., Anastassiou, C.A., Koch, C. (2012) The origin of extracellular fields and currents-EEG, ECoG, LFP and spikes. *Nature Reviews Neuroscience*. **13**(6), 407–420.

Cardin, J.A., Carlén, M., Meletis, K., Knoblich, U., Zhang, F., Deisseroth, K., Tsai, L.-H., Moore, C.I. (2009) Driving fast-spiking cells induces gamma rhythm and controls sensory responses. *Nature*. **459**(7247), 663–667.

Carlén, M. (2017) What constitutes the prefrontal cortex? *Science*. **358**(6362), 478–482.

Carrillo-Reid, L., Han, S., Yang, W., Akrouh, A., Yuste, R. (2019) Controlling Visually Guided Behavior by Holographic Recalling of Cortical Ensembles. *Cell*. **178**(2), 447–457.e5.

Carter, M.E., Yizhar, O., Chikahisa, S., Nguyen, H., Adamantidis, A., Nishino, S., Deisseroth, K., de Lecea, L. (2010) Tuning arousal with optogenetic modulation of locus coeruleus neurons. *Nature Neuroscience*. **13**(12), 1526–1533.

Cedarbaum, J.M., Aghajanian, G.K. (1978) Activation of locus coeruleus neurons by peripheral stimuli: Modulation by a collateral inhibitory mechanism. *Life Sciences*. **23**(13), 1383–1392.

Chan, R.W., Leong, A.T.L., Ho, L.C., Gao, P.P., Wong, E.C., Dong, C.M., Wang, X., He, J., Chan, Y.-S., Lim, L.W., Wu, E.X. (2017) Low-frequency hippocampal–cortical activity drives brain-wide resting-state functional MRI connectivity. *Proceedings of the National Academy of Sciences*. **114**(33).

Chandler, D.J., Gao, W.-J., Waterhouse, B.D. (2014) Heterogeneous organization of the

locus coeruleus projections to prefrontal and motor cortices. *Proceedings of the National Academy of Sciences*. **111**(18), 6816–6821.

Chandler, D.J., Jensen, P., McCall, J.G., Pickering, A.E., Schwarz, L.A., Totah, N.K. (2019) Redefining Noradrenergic Neuromodulation of Behavior: Impacts of a Modular Locus Coeruleus Architecture. *The Journal of Neuroscience*. **39**(42), 8239–8249.

Chandler, D.J., Lamperski, C.S., Waterhouse, B.D. (2013) Identification and distribution of projections from monoaminergic and cholinergic nuclei to functionally differentiated subregions of prefrontal cortex. *Brain Research*. **1522**, 38–58.

Chen, F.-J., Sara, S.J. (2007) Locus coeruleus activation by foot shock or electrical stimulation inhibits amygdala neurons. *Neuroscience*. **144**(2), 472–481.

Chen, Y., Bressler, S.L., Ding, M. (2006) Frequency decomposition of conditional Granger causality and application to multivariate neural field potential data. *Journal of Neuroscience Methods*. **150**(2), 228–237.

Clement, E.A., Richard, A., Thwaites, M., Ailon, J., Peters, S., Dickson, C.T. (2008) Cyclic and Sleep-Like Spontaneous Alternations of Brain State Under Urethane Anaesthesia E. Greene, ed. *PLoS ONE*. **3**(4), e2004.

Coletta, L., Pagani, M., Whitesell, J.D., Harris, J.A., Bernhardt, B., Gozzi, A. (2020) Network structure of the mouse brain connectome with voxel resolution. *Science Advances*. **6**(51).

Cunningham, J.P., Yu, B.M. (2014) Dimensionality reduction for large-scale neural recordings. *Nature Neuroscience*. **17**(11), 1500–1509.

David, F., Schmiedt, J.T., Taylor, H.L., Orban, G., Di Giovanni, G., Uebele, V.N., Renger, J.J., Lambert, R.C., Leresche, N., Crunelli, V. (2013) Essential Thalamic Contribution to Slow Waves of Natural Sleep. *Journal of Neuroscience*. **33**(50), 19599–19610.

Devilbiss, D.M. (2004) The Effects of Tonic Locus Coeruleus Output on Sensory-Evoked Responses of Ventral Posterior Medial Thalamic and Barrel Field Cortical Neurons in the Awake Rat. *Journal of Neuroscience*. **24**(48), 10773–10785.

Donner, T.H., Siegel, M. (2011) A framework for local cortical oscillation patterns. *Trends in Cognitive Sciences*. **15**(5), 191–199.

Dubovik, S., Pignat, J.-M., Ptak, R., Aboulafia, T., Allet, L., Gillabert, N., Magnin, C., Albert, F., Momjian-Mayor, I., Nahum, L., Lascano, A.M., Michel, C.M., Schnider, A., Guggisberg, A.G. (2012) The behavioral significance of coherent resting-state oscillations after stroke. *NeuroImage*. **61**(1), 249–257.

Eggermann, E., Kremer, Y., Crochet, S., Petersen, C.C.H. (2014) Cholinergic Signals in Mouse Barrel Cortex during Active Whisker Sensing. *Cell Reports*. **9**(5), 1654–1660.

Einevoll, G.T., Kayser, C., Logothetis, N.K., Panzeri, S. (2013) Modelling and analysis of local field potentials for studying the function of cortical circuits. *Nature Reviews Neuroscience*. **14**(11), 770–785.

Eldaief, M.C., Halko, M.A., Buckner, R.L., Pascual-Leone, A. (2011) Transcranial magnetic stimulation modulates the brain's intrinsic activity in a frequency-dependent manner. *Proceedings of the National Academy of Sciences*. **108**(52), 21229–21234.

Eldridge, J., Lane, A.E., Belkin, M., Dennis, S. (2014) Robust features for the automatic identification of autism spectrum disorder in children. *Journal of Neurodevelopmental Disorders*. **6**(1), 12.

- Ferrari, L., Turrini, G., Crestan, V., Bertani, S., Cristofori, P., Bifone, A., Gozzi, A. (2012) A robust experimental protocol for pharmacological fMRI in rats and mice. *Journal of Neuroscience Methods*. **204**(1), 9–18.
- Ferro, D., van Kempen, J., Boyd, M., Panzeri, S., Thiele, A. (2021) Directed information exchange between cortical layers in macaque V1 and V4 and its modulation by selective attention. *Proceedings of the National Academy of Sciences*. **118**(12).
- Finlayson, P.G., Marshall, K.C. (1988) Synchronous bursting of locus coeruleus neurons in tissue culture. *Neuroscience*. **24**(1), 217–225.
- Foot, S.L., Aston-Jones, G., Bloom, F.E. (1980) Impulse activity of locus coeruleus neurons in awake rats and monkeys is a function of sensory stimulation and arousal. *Proceedings of the National Academy of Sciences*. **77**(5), 3033–3037.
- Franks, N.P. (2008) General anaesthesia: from molecular targets to neuronal pathways of sleep and arousal. *Nature Reviews Neuroscience*. **9**(5), 370–386.
- Frien, A., Eckhorn, R., Bauer, R., Woelbern, T., Gabriel, A. (2000) Fast oscillations display sharper orientation tuning than slower components of the same recordings in striate cortex of the awake monkey. *European Journal of Neuroscience*. **12**(4), 1453–1465.
- Fries, P. (2015) Rhythms for Cognition: Communication through Coherence. *Neuron*. **88**(1), 220–235.
- Friston, K., Büchel, C. (2007) Functional connectivity: eigenimages and multivariate analyses. In *Statistical Parametric Mapping*. Elsevier, pp. 492–507.
- Friston, K.J. (2011) Functional and Effective Connectivity: A Review. *Brain Connectivity*. **1**(1), 13–36.
- Gabard-Durnam, L.J., Wilkinson, C., Kapur, K., Tager-Flusberg, H., Levin, A.R., Nelson, C.A. (2019) Longitudinal EEG power in the first postnatal year differentiates autism outcomes. *Nature Communications*. **10**(1), 4188.
- Gao, R., Peterson, E.J., Voytek, B. (2017) Inferring synaptic excitation/inhibition balance from field potentials. *NeuroImage*. **158**, 70–78.
- Gent, T.C., Bandarabadi, M., Herrera, C.G., Adamantidis, A.R. (2018) Thalamic dual control of sleep and wakefulness. *Nature Neuroscience*. **21**(7), 974–984.
- Gill, J. V., Lerman, G.M., Zhao, H., Stetler, B.J., Rinberg, D., Shoham, S. (2020) Precise Holographic Manipulation of Olfactory Circuits Reveals Coding Features Determining Perceptual Detection. *Neuron*. **108**(2), 382–393.e5.
- Giorgi, A., Migliarini, S., Galbusera, A., Maddaloni, G., Mereu, M., Margiani, G., Gritti, M., Landi, S., Trovato, F., Bertozzi, S.M., Armirotti, A., Ratto, G.M., De Luca, M.A., Tonini, R., Gozzi, A., Pasqualetti, M. (2017) Brain-wide Mapping of Endogenous Serotonergic Transmission via Chemogenetic fMRI. *Cell Reports*. **21**(4), 910–918.
- Goense, J.B.M., Logothetis, N.K. (2008) Neurophysiology of the BOLD fMRI Signal in Awake Monkeys. *Current Biology*. **18**(9), 631–640.
- Gomez, J.L., Bonaventura, J., Lesniak, W., Mathews, W.B., Sysa-Shah, P., Rodriguez, L.A., Ellis, R.J., Richie, C.T., Harvey, B.K., Dannals, R.F., Pomper, M.G., Bonci, A., Michaelides, M. (2017) Chemogenetics revealed: DREADD occupancy and activation via converted clozapine. *Science*. **357**(6350), 503–507.

- Goñi, J., van den Heuvel, M.P., Avena-Koenigsberger, A., Velez de Mendizabal, N., Betzel, R.F., Griffa, A., Hagmann, P., Corominas-Murtra, B., Thiran, J.-P., Sporns, O. (2014) Resting-brain functional connectivity predicted by analytic measures of network communication. *Proceedings of the National Academy of Sciences*. **111**(2), 833–838.
- Gozzi, A., Ceolin, L., Schwarz, A., Reese, T., Bertani, S., Crestan, V., Bifone, A. (2007) A multimodality investigation of cerebral hemodynamics and autoregulation in pharmacological MRI. *Magnetic Resonance Imaging*. **25**(6), 826–833.
- Grandjean, J., Canella, C., Anckaerts, C., Ayrancı, G., Bougacha, S., Bienert, T., Buehlmann, D., Coletta, L., Gallino, D., Gass, N., Garin, C.M., Nadkarni, N.A., Hübner, N.S., Karatas, M., Komaki, Y., Kreitz, S., Mandino, F., Mechling, A.E., Sato, C., Sauer, K., Shah, D., Strobel, S., Takata, N., Wank, I., Wu, T., Yahata, N., Yeow, L.Y., Yee, Y., Aoki, I., Chakravarty, M.M., Chang, W.-T., Dhenain, M., von Elverfeldt, D., Harsan, L.-A., Hess, A., Jiang, T., Keliris, G.A., Lerch, J.P., Meyer-Lindenberg, A., Okano, H., Rudin, M., Sartorius, A., Van der Linden, A., Verhoye, M., Weber-Fahr, W., Wenderoth, N., Zerbi, V., Gozzi, A. (2020) Common functional networks in the mouse brain revealed by multi-centre resting-state fMRI analysis. *NeuroImage*. **205**, 116278.
- Grayson, D.S., Bliss-Moreau, E., Machado, C.J., Bennett, J., Shen, K., Grant, K.A., Fair, D.A., Amaral, D.G. (2016) The Rhesus Monkey Connectome Predicts Disrupted Functional Networks Resulting from Pharmacogenetic Inactivation of the Amygdala. *Neuron*. **91**(2), 453–466.
- Grzanna, R., Molliver, M.E. (1980) The locus coeruleus in the rat: An immunohistochemical delineation. *Neuroscience*. **5**(1), 21–40.
- Gutierrez-Barragan, D., Basson, M.A., Panzeri, S., Gozzi, A. (2019) Infralow State Fluctuations Govern Spontaneous fMRI Network Dynamics. *Current Biology*. **29**(14), 2295–2306.e5.
- Gutierrez-Barragan, D., Singh, N.A., Alvino, F.G., Coletta, L., Rocchi, F., De Guzman, E., Galbusera, A., Uboldi, M., Panzeri, S., Gozzi, A. (2022) Unique spatiotemporal fMRI dynamics in the awake mouse brain. *Current Biology*. **32**(3), 631–644.e6.
- Hagmann, P., Cammoun, L., Gigandet, X., Meuli, R., Honey, C.J., Wedeen, V.J., Sporns, O. (2008) Mapping the Structural Core of Human Cerebral Cortex K. J. Friston, ed. *PLoS Biology*. **6**(7), e159.
- Haider, B., McCormick, D.A. (2009) Rapid Neocortical Dynamics: Cellular and Network Mechanisms. *Neuron*. **62**(2), 171–189.
- Harris, K.D., Thiele, A. (2011) Cortical state and attention. *Nature Reviews Neuroscience*. **12**(9), 509–523.
- Hay, Y.A., Deperrois, N., Fuchsberger, T., Quarrell, T.M., Koerling, A.-L., Paulsen, O. (2021) Thalamus mediates neocortical Down state transition via GABAB-receptor-targeting interneurons. *Neuron*. **109**(17), 2682–2690.e5.
- Hayat, H., Regev, N., Matosevich, N., Sales, A., Paredes-Rodriguez, E., Krom, A.J., Bergman, L., Li, Y., Lavigne, M., Kremer, E.J., Yizhar, O., Pickering, A.E., Nir, Y. (2020) Locus coeruleus norepinephrine activity mediates sensory-evoked awakenings from sleep. *Science Advances*. **6**(15).
- He, B.J., Snyder, A.Z., Zempel, J.M., Smyth, M.D., Raichle, M.E. (2008) Electrophysiological correlates of the brain's intrinsic large-scale functional architecture. *Proceedings of the*

National Academy of Sciences. **105**(41), 16039–16044.

Hervé-Minvielle, A., Sara, S.J. (1995) Rapid habituation of auditory responses of locus coeruleus cells in anaesthetized and awake rats. *NeuroReport*. **6**(10), 1363–1368.

van den Heuvel, M.P., Hulshoff Pol, H.E. (2010) Exploring the brain network: A review on resting-state fMRI functional connectivity. *European Neuropsychopharmacology*. **20**(8), 519–534.

Hickey, L., Li, Y., Fyson, S.J., Watson, T.C., Perrins, R., Hewinson, J., Teschemacher, A.G., Furue, H., Lumb, B.M., Pickering, A.E. (2014) Optoactivation of Locus Coeruleus Neurons Evokes Bidirectional Changes in Thermal Nociception in Rats. *Journal of Neuroscience*. **34**(12), 4148–4160.

Hillary, F.G., Grafman, J.H. (2017) Injured Brains and Adaptive Networks: The Benefits and Costs of Hyperconnectivity. *Trends in Cognitive Sciences*. **21**(5), 385–401.

Hipp, J.F., Hawellek, D.J., Corbetta, M., Siegel, M., Engel, A.K. (2012) Large-scale cortical correlation structure of spontaneous oscillatory activity. *Nature Neuroscience*. **15**(6), 884–890.

Hirschberg, S., Li, Y., Randall, A., Kremer, E.J., Pickering, A.E. (2017) Functional dichotomy in spinal- vs prefrontal-projecting locus coeruleus modules splits descending noradrenergic analgesia from ascending aversion and anxiety in rats. *eLife*. **6**.

Holiga, Š., Hipp, J.F., Chatham, C.H., Garces, P., Spooren, W., D’Ardhuy, X.L., Bertolino, A., Bouquet, C., Buitelaar, J.K., Bours, C., Rausch, A., Oldehinkel, M., Bouvard, M., Amestoy, A., Caralp, M., Gueguen, S., Ly-Le Moal, M., Houenou, J., Beckmann, C.F., Loth, E., Murphy, D., Charman, T., Tillmann, J., Laidi, C., Delorme, R., Beggiato, A., Gaman, A., Scheid, I., Leboyer, M., D’Albis, M.-A., Sevigny, J., Czech, C., Bolognani, F., Honey, G.D., Dukart, J. (2019) Patients with autism spectrum disorders display reproducible functional connectivity alterations. *Science Translational Medicine*. **11**(481).

Honey, C.J., Sporns, O., Cammoun, L., Gigandet, X., Thiran, J.P., Meuli, R., Hagmann, P. (2009) Predicting human resting-state functional connectivity from structural connectivity. *Proceedings of the National Academy of Sciences*. **106**(6), 2035–2040.

Huang, X.-Q., Lui, S., Deng, W., Chan, R.C.K., Wu, Q.-Z., Jiang, L.-J., Zhang, J.-R., Jia, Z.-Y., Li, X.-L., Li, F., Chen, L., Li, T., Gong, Q.-Y. (2010) Localization of cerebral functional deficits in treatment-naïve, first-episode schizophrenia using resting-state fMRI. *NeuroImage*. **49**(4), 2901–2906.

Hughes, S.W., Cope, D.W., Blethyn, K.L., Crunelli, V. (2002) Cellular Mechanisms of the Slow (<1 Hz) Oscillation in Thalamocortical Neurons In Vitro. *Neuron*. **33**(6), 947–958.

Hull, J. V., Dokovna, L.B., Jacokes, Z.J., Torgerson, C.M., Irimia, A., Van Horn, J.D. (2017) Resting-State Functional Connectivity in Autism Spectrum Disorders: A Review. *Frontiers in Psychiatry*. **7**.

Huth, A.G., Nishimoto, S., Vu, A.T., Gallant, J.L. (2012) A Continuous Semantic Space Describes the Representation of Thousands of Object and Action Categories across the Human Brain. *Neuron*. **76**(6), 1210–1224.

Ishimatsu, M., Williams, J.T. (1996) Synchronous Activity in Locus Coeruleus Results from Dendritic Interactions in Pericoerulear Regions. *The Journal of Neuroscience*. **16**(16), 5196–5204.

- Jendryka, M., Palchadhuri, M., Ursu, D., van der Veen, B., Liss, B., Kätzel, D., Nissen, W., Pekcec, A. (2019) Pharmacokinetic and pharmacodynamic actions of clozapine-N-oxide, clozapine, and compound 21 in DREADD-based chemogenetics in mice. *Scientific Reports*. **9**(1), 4522.
- Jensen, O., Mazaheri, A. (2010) Shaping Functional Architecture by Oscillatory Alpha Activity: Gating by Inhibition. *Frontiers in Human Neuroscience*. **4**.
- Jones, B.E. (2020) Arousal and sleep circuits. *Neuropsychopharmacology*. **45**(1), 6–20.
- Kayser, C. (2004) A Comparison of Hemodynamic and Neural Responses in Cat Visual Cortex Using Complex Stimuli. *Cerebral Cortex*. **14**(8), 881–891.
- Kayser, C., König, P. (2004) Stimulus locking and feature selectivity prevail in complementary frequency ranges of V1 local field potentials. *European Journal of Neuroscience*. **19**(2), 485–489.
- van Kerkoerle, T., Self, M.W., Dagnino, B., Gariel-Mathis, M.-A., Poort, J., van der Togt, C., Roelfsema, P.R. (2014) Alpha and gamma oscillations characterize feedback and feedforward processing in monkey visual cortex. *Proceedings of the National Academy of Sciences*. **111**(40), 14332–14341.
- Lakatos, P., Karmos, G., Mehta, A.D., Ulbert, I., Schroeder, C.E. (2008) Entrainment of Neuronal Oscillations as a Mechanism of Attentional Selection. *Science*. **320**(5872), 110–113.
- Lee, A.M., Hoy, J.L., Bonci, A., Wilbrecht, L., Stryker, M.P., Niell, C.M. (2014) Identification of a Brainstem Circuit Regulating Visual Cortical State in Parallel with Locomotion. *Neuron*. **83**(2), 455–466.
- Lee, D.D., Seung, H.S. (1999) Learning the parts of objects by non-negative matrix factorization. *Nature*. **401**(6755), 788–791.
- Lee, S.-H., Broadwater, M.A., Ban, W., Wang, T.-W.W., Kim, H.-J., Dumas, J.S., Vetreno, R.P., Herman, M.A., Morrow, A.L., Besheer, J., Kash, T.L., Boettiger, C.A., Robinson, D.L., Crews, F.T., Shih, Y.-Y.I. (2021) An isotropic EPI database and analytical pipelines for rat brain resting-state fMRI. *NeuroImage*. **243**, 118541.
- Leichsenring, F., Leibing, E., Kruse, J., New, A.S., Leweke, F. (2011) Borderline personality disorder. *The Lancet*. **377**(9759), 74–84.
- Li, J., Kong, R., Liégeois, R., Orban, C., Tan, Y., Sun, N., Holmes, A.J., Sabuncu, M.R., Ge, T., Yeo, B.T.T. (2019) Global signal regression strengthens association between resting-state functional connectivity and behavior. *NeuroImage*. **196**, 126–141.
- Liska, A., Galbusera, A., Schwarz, A.J., Gozzi, A. (2015) Functional connectivity hubs of the mouse brain. *NeuroImage*. **115**, 281–291.
- Liu, X., de Zwart, J.A., Schölvinck, M.L., Chang, C., Ye, F.Q., Leopold, D.A., Duyn, J.H. (2018) Subcortical evidence for a contribution of arousal to fMRI studies of brain activity. *Nature Communications*. **9**(1), 395.
- Logothetis, N.K. (2008) What we can do and what we cannot do with fMRI. *Nature*. **453**(7197), 869–878.
- Logothetis, N.K., Pauls, J., Augath, M., Trinath, T., Oeltermann, A. (2001) Neurophysiological investigation of the basis of the fMRI signal. *Nature*. **412**(6843), 150–157.

- Lu, H., Wang, L., Rea, W.W., Brynildsen, J.K., Jaime, S., Zuo, Y., Stein, E.A., Yang, Y. (2014) Low- but Not High-Frequency LFP Correlates with Spontaneous BOLD Fluctuations in Rat Whisker Barrel Cortex. *Cerebral Cortex*, bhu248.
- Lu, H., Zuo, Y., Gu, H., Waltz, J.A., Zhan, W., Scholl, C.A., Rea, W., Yang, Y., Stein, E.A. (2007) Synchronized delta oscillations correlate with the resting-state functional MRI signal. *Proceedings of the National Academy of Sciences*. **104**(46), 18265–18269.
- Lynall, M.-E., Bassett, D.S., Kerwin, R., McKenna, P.J., Kitzbichler, M., Muller, U., Bullmore, E. (2010) Functional Connectivity and Brain Networks in Schizophrenia. *Journal of Neuroscience*. **30**(28), 9477–9487.
- MacDowell, C.J., Buschman, T.J. (2020) Low-Dimensional Spatiotemporal Dynamics Underlie Cortex-wide Neural Activity. *Current Biology*. **30**(14), 2665–2680.e8.
- Magri, C., Schridde, U., Murayama, Y., Panzeri, S., Logothetis, N.K. (2012) The Amplitude and Timing of the BOLD Signal Reflects the Relationship between Local Field Potential Power at Different Frequencies. *Journal of Neuroscience*. **32**(4), 1395–1407.
- Mahmud, M., Vassanelli, S. (2016) Processing and Analysis of Multichannel Extracellular Neuronal Signals: State-of-the-Art and Challenges. *Frontiers in Neuroscience*. **10**.
- Markicevic, M., Fulcher, B.D., Lewis, C., Helmchen, F., Rudin, M., Zerbi, V., Wenderoth, N. (2020) Cortical Excitation:Inhibition Imbalance Causes Abnormal Brain Network Dynamics as Observed in Neurodevelopmental Disorders. *Cerebral Cortex*. **30**(9), 4922–4937.
- Martínez-Cañada, P., Noei, S., Panzeri, S. (2021) Methods for inferring neural circuit interactions and neuromodulation from local field potential and electroencephalogram measures. *Brain Informatics*. **8**(1), 27.
- Di Martino, A., Yan, C.-G., Li, Q., Denio, E., Castellanos, F.X., Alaerts, K., Anderson, J.S., Assaf, M., Bookheimer, S.Y., Dapretto, M., Deen, B., Delmonte, S., Dinstein, I., Ertl-Wagner, B., Fair, D.A., Gallagher, L., Kennedy, D.P., Keown, C.L., Keyzers, C., Lainhart, J.E., Lord, C., Luna, B., Menon, V., Minshew, N.J., Monk, C.S., Mueller, S., Müller, R.-A., Nebel, M.B., Nigg, J.T., O’Hearn, K., Pelphrey, K.A., Peltier, S.J., Rudie, J.D., Sunaert, S., Thioux, M., Tyszka, J.M., Uddin, L.Q., Verhoeven, J.S., Wenderoth, N., Wiggins, J.L., Mostofsky, S.H., Milham, M.P. (2014) The autism brain imaging data exchange: towards a large-scale evaluation of the intrinsic brain architecture in autism. *Molecular Psychiatry*. **19**(6), 659–667.
- Marzo, A., Totah, N.K., Neves, R.M., Logothetis, N.K., Eschenko, O. (2014) Unilateral electrical stimulation of rat locus coeruleus elicits bilateral response of norepinephrine neurons and sustained activation of medial prefrontal cortex. *Journal of Neurophysiology*. **111**(12), 2570–2588.
- Marzo, A., Totah, N.K., Neves, R.M., Logothetis, N.K., Eschenko, O. (2014) Unilateral electrical stimulation of rat locus coeruleus elicits bilateral response of norepinephrine neurons and sustained activation of medial prefrontal cortex. *Journal of Neurophysiology*. **111**(12), 2570–2588.
- Mateo, C., Knutsen, P.M., Tsai, P.S., Shih, A.Y., Kleinfeld, D. (2017) Entrainment of Arteriole Vasomotor Fluctuations by Neural Activity Is a Basis of Blood-Oxygenation-Level-Dependent “Resting-State” Connectivity. *Neuron*. **96**(4), 936–948.e3.
- Mazzoni, A., Brunel, N., Cavallari, S., Logothetis, N.K., Panzeri, S. (2011) Cortical dynamics during naturalistic sensory stimulations: Experiments and models. *Journal of Physiology-*

Paris. **105**(1–3), 2–15.

McCall, J.G., Al-Hasani, R., Siuda, E.R., Hong, D.Y., Norris, A.J., Ford, C.P., Bruchas, M.R. (2015) CRH Engagement of the Locus Coeruleus Noradrenergic System Mediates Stress-Induced Anxiety. *Neuron*. **87**(3), 605–620.

McCormick, D.A. (1992) Neurotransmitter actions in the thalamus and cerebral cortex and their role in neuromodulation of thalamocortical activity. *Progress in Neurobiology*. **39**(4), 337–388.

McCormick, D.A., Nestvogel, D.B., He, B.J. (2020) Neuromodulation of Brain State and Behavior. *Annual Review of Neuroscience*. **43**(1), 391–415.

McCune, S.K., Voigt, M.M., Hill, J.M. (1993) Expression of multiple alpha adrenergic receptor subtype messenger RNAs in the adult rat brain. *Neuroscience*. **57**(1), 143–151.

McGinley, M.J., Vinck, M., Reimer, J., Batista-Brito, R., Zagha, E., Cadwell, C.R., Tolias, A.S., Cardin, J.A., McCormick, D.A. (2015) Waking State: Rapid Variations Modulate Neural and Behavioral Responses. *Neuron*. **87**(6), 1143–1161.

Mitchell, A.S. (2015) The mediodorsal thalamus as a higher order thalamic relay nucleus important for learning and decision-making. *Neuroscience & Biobehavioral Reviews*. **54**, 76–88.

Mitra, Partha & Bokli, H. (2007) *Observed Brain Dynamics*. Oxford University Press.

Mitra, A., Kraft, A., Wright, P., Acland, B., Snyder, A.Z., Rosenthal, Z., Czerniewski, L., Bauer, A., Snyder, L., Culver, J., Lee, J.-M., Raichle, M.E. (2018) Spontaneous Infra-slow Brain Activity Has Unique Spatiotemporal Dynamics and Laminar Structure. *Neuron*. **98**(2), 297–305.e6.

Mueller, D., Porter, J.T., Quirk, G.J. (2008) Noradrenergic Signaling in Infralimbic Cortex Increases Cell Excitability and Strengthens Memory for Fear Extinction. *Journal of Neuroscience*. **28**(2), 369–375.

Munn, B.R., Müller, E.J., Wainstein, G., Shine, J.M. (2021) The ascending arousal system shapes neural dynamics to mediate awareness of cognitive states. *Nature Communications*. **12**(1), 6016.

Murayama, Y., Bießmann, F., Meinecke, F.C., Müller, K.-R., Augath, M., Oeltermann, A., Logothetis, N.K. (2010) Relationship between neural and hemodynamic signals during spontaneous activity studied with temporal kernel CCA. *Magnetic Resonance Imaging*. **28**(8), 1095–1103.

Narikiyo, K., Mizuguchi, R., Ajima, A., Shiozaki, M., Hamanaka, H., Johansen, J.P., Mori, K., Yoshihara, Y. (2020) The claustrum coordinates cortical slow-wave activity. *Nature Neuroscience*. **23**(6), 741–753.

Nathanson, J.L., Yanagawa, Y., Obata, K., Callaway, E.M. (2009) Preferential labeling of inhibitory and excitatory cortical neurons by endogenous tropism of adeno-associated virus and lentivirus vectors. *Neuroscience*. **161**(2), 441–450.

Nelson, S.B., Valakh, V. (2015) Excitatory/Inhibitory Balance and Circuit Homeostasis in Autism Spectrum Disorders. *Neuron*. **87**(4), 684–698.

Neuner, I., Arrubla, J., Werner, C.J., Hitz, K., Boers, F., Kawohl, W., Shah, N.J. (2014) The Default Mode Network and EEG Regional Spectral Power: A Simultaneous fMRI-EEG Study D. R. Chialvo, ed. *PLoS ONE*. **9**(2), e88214.

- Neves, R.M., van Keulen, S., Yang, M., Logothetis, N.K., Eschenko, O. (2018) Locus coeruleus phasic discharge is essential for stimulus-induced gamma oscillations in the prefrontal cortex. *Journal of Neurophysiology*. **119**(3), 904–920.
- Newson, J.J., Thiagarajan, T.C. (2019) EEG Frequency Bands in Psychiatric Disorders: A Review of Resting State Studies. *Frontiers in Human Neuroscience*. **12**.
- Niessing, J., Ebisch, B., Schmidt, K.E., Niessing, M., Singer, W., Galuske, R.A.W. (2005) Hemodynamic Signals Correlate Tightly with Synchronized Gamma Oscillations. *Science*. **309**(5736), 948–951.
- Nir, Y., Mukamel, R., Dinstein, I., Privman, E., Harel, M., Fisch, L., Gelbard-Sagiv, H., Kipervasser, S., Andelman, F., Neufeld, M.Y., Kramer, U., Arieli, A., Fried, I., Malach, R. (2008) Interhemispheric correlations of slow spontaneous neuronal fluctuations revealed in human sensory cortex. *Nature Neuroscience*. **11**(9), 1100–1108.
- Noei, S., Zouridis, I.S., Logothetis, N.K., Panzeri, S., Totah, N.K. (2022) Distinct ensembles in the noradrenergic locus coeruleus are associated with diverse cortical states. *Proceedings of the National Academy of Sciences*. **119**(18).
- Nunez, P.L., Srinivasan, R. (2006) *Electric Fields of the Brain*. Oxford University Press.
- O'Reilly, J.X., Croxson, P.L., Jbabdi, S., Sallet, J., Noonan, M.P., Mars, R.B., Browning, P.G.F., Wilson, C.R.E., Mitchell, A.S., Miller, K.L., Rushworth, M.F.S., Baxter, M.G. (2013) Causal effect of disconnection lesions on interhemispheric functional connectivity in rhesus monkeys. *Proceedings of the National Academy of Sciences*. **110**(34), 13982–13987.
- Onken, A., Liu, J.K., Karunasekara, P.P.C.R., Delis, I., Gollisch, T., Panzeri, S. (2016) Using Matrix and Tensor Factorizations for the Single-Trial Analysis of Population Spike Trains M. Bethge, ed. *PLOS Computational Biology*. **12**(11), e1005189.
- Pagani, M., Barsotti, N., Bertero, A., Trakoshis, S., Ulysse, L., Locarno, A., Miseviciute, I., De Felice, A., Canella, C., Supekar, K., Galbusera, A., Menon, V., Tonini, R., Deco, G., Lombardo, M. V., Pasqualetti, M., Gozzi, A. (2021) mTOR-related synaptic pathology causes autism spectrum disorder-associated functional hyperconnectivity. *Nature Communications*. **12**(1), 6084.
- Pagani, M., Bertero, A., Liska, A., Galbusera, A., Sabbioni, M., Barsotti, N., Colenbier, N., Marinazzo, D., Scattoni, M.L., Pasqualetti, M., Gozzi, A. (2019) Deletion of Autism Risk Gene Shank3 Disrupts Prefrontal Connectivity. *The Journal of Neuroscience*. **39**(27), 5299–5310.
- Pan, W.-J., Thompson, G.J., Magnuson, M.E., Jaeger, D., Keilholz, S. (2013) Infralow LFP correlates to resting-state fMRI BOLD signals. *NeuroImage*. **74**, 288–297.
- Panzeri, S., Harvey, C.D., Piasini, E., Latham, P.E., Fellin, T. (2017) Cracking the Neural Code for Sensory Perception by Combining Statistics, Intervention, and Behavior. *Neuron*. **93**(3), 491–507.
- Paxinos, G., Watson, C. (2017) *The Rat Brain in Stereotaxic Coordinates: Compact 7th Edition* (Academic Press).
- Peeters, L.M., Hinz, R., Detrez, J.R., Missault, S., De Vos, W.H., Verhoye, M., Van der Linden, A., Keliris, G.A. (2020) Chemogenetic silencing of neurons in the mouse anterior cingulate area modulates neuronal activity and functional connectivity. *NeuroImage*. **220**, 117088.

- Pesaran, B., Pezaris, J.S., Sahani, M., Mitra, P.P., Andersen, R.A. (2002) Temporal structure in neuronal activity during working memory in macaque parietal cortex. *Nature Neuroscience*. **5**(8), 805–811.
- Pesaran, B., Vinck, M., Einevoll, G.T., Sirota, A., Fries, P., Siegel, M., Truccolo, W., Schroeder, C.E., Srinivasan, R. (2018) Investigating large-scale brain dynamics using field potential recordings: analysis and interpretation. *Nature Neuroscience*. **21**(7), 903–919.
- Ponce-Alvarez, A., Deco, G., Hagmann, P., Romani, G.L., Mantini, D., Corbetta, M. (2015) Resting-State Temporal Synchronization Networks Emerge from Connectivity Topology and Heterogeneity C. C. Hilgetag, ed. *PLOS Computational Biology*. **11**(2), e1004100.
- Power, J.D., Schlaggar, B.L., Petersen, S.E. (2014) Studying Brain Organization via Spontaneous fMRI Signal. *Neuron*. **84**(4), 681–696.
- Pusil, S., López, M.E., Cuesta, P., Bruña, R., Pereda, E., Maestú, F. (2019) Hypersynchronization in mild cognitive impairment: the ‘X’ model. *Brain*. **142**(12), 3936–3950.
- Quirarte, G.L., Galvez, R., Roozendaal, B., McGaugh, J.L. (1998) Norepinephrine release in the amygdala in response to footshock and opioid peptidergic drugs. *Brain Research*. **808**(2), 134–140.
- Quiroga, R.Q., Nadasdy, Z., Ben-Shaul, Y. (2004) Unsupervised Spike Detection and Sorting with Wavelets and Superparamagnetic Clustering. *Neural Computation*. **16**(8), 1661–1687.
- Rajkowski, J., Kubiak, P., Aston-Jones, G. (1994) Locus coeruleus activity in monkey: Phasic and tonic changes are associated with altered vigilance. *Brain Research Bulletin*. **35**(5–6), 607–616.
- Ranasinghe, K.G., Cha, J., Iaccarino, L., Hinkley, L.B., Beagle, A.J., Pham, J., Jagust, W.J., Miller, B.L., Rankin, K.P., Rabinovici, G.D., Vossel, K.A., Nagarajan, S.S. (2020) Neurophysiological signatures in Alzheimer’s disease are distinctly associated with TAU, amyloid- β accumulation, and cognitive decline. *Science Translational Medicine*. **12**(534).
- Rand, W.M. (1971) Objective criteria for the evaluation of clustering methods. *Journal of the American Statistical Association*. **66**(336), 846–850.
- Ray, S., Maunsell, J.H.R. (2011) Different Origins of Gamma Rhythm and High-Gamma Activity in Macaque Visual Cortex L. Ungerleider, ed. *PLoS Biology*. **9**(4), e1000610.
- Reimann, H.M., Niendorf, T. (2020) The (Un)Conscious Mouse as a Model for Human Brain Functions: Key Principles of Anesthesia and Their Impact on Translational Neuroimaging. *Frontiers in Systems Neuroscience*. **14**.
- Reimer, J., McGinley, M.J., Liu, Y., Rodenkirch, C., Wang, Q., McCormick, D.A., Tolia, A.S. (2016) Pupil fluctuations track rapid changes in adrenergic and cholinergic activity in cortex. *Nature Communications*. **7**(1), 13289.
- Rilling, J.K., Barks, S.K., Parr, L.A., Preuss, T.M., Faber, T.L., Pagnoni, G., Bremner, J.D., Votaw, J.R. (2007) A comparison of resting-state brain activity in humans and chimpanzees. *Proceedings of the National Academy of Sciences*. **104**(43), 17146–17151.
- Rocchi, F., Canella, C., Noei, S., Gutierrez-Barragan, D., Coletta, L., Galbusera, A., Stuefer, A., Vassanelli, S., Pasqualetti, M., Iurilli, G., Panzeri, S., Gozzi, A. (2022) Increased fMRI connectivity upon chemogenetic inhibition of the mouse prefrontal cortex. *Nature*

Communications. **13**(1), 1056.

Rousseeuw, P.J. (1987) Silhouettes: A graphical aid to the interpretation and validation of cluster analysis. *Journal of Computational and Applied Mathematics*. **20**(C), 53–65.

Safaai, H., Neves, R., Eschenko, O., Logothetis, N.K., Panzeri, S. (2015) Modeling the effect of locus coeruleus firing on cortical state dynamics and single-trial sensory processing. *Proceedings of the National Academy of Sciences of the United States of America*. **112**(41), 12834–12839.

Sara, S.J., Bouret, S. (2012) Orienting and Reorienting: The Locus Coeruleus Mediates Cognition through Arousal. *Neuron*. **76**(1), 130–141.

Saxena, S., Kinsella, I., Musall, S., Kim, S.H., Meszaros, J., Thibodeaux, D.N., Kim, C., Cunningham, J., Hillman, E.M.C., Churchland, A., Paninski, L. (2020) Localized semi-nonnegative matrix factorization (LocaNMF) of widefield calcium imaging data J. H. Macke, ed. *PLOS Computational Biology*. **16**(4), e1007791.

Scheeringa, R., Petersson, K.M., Oostenveld, R., Norris, D.G., Hagoort, P., Bastiaansen, M.C.M. (2009) Trial-by-trial coupling between EEG and BOLD identifies networks related to alpha and theta EEG power increases during working memory maintenance. *NeuroImage*. **44**(3), 1224–1238.

Schleifer, C., Lin, A., Kushan, L., Ji, J.L., Yang, G., Bearden, C.E., Anticevic, A. (2019) Dissociable Disruptions in Thalamic and Hippocampal Resting-State Functional Connectivity in Youth with 22q11.2 Deletions. *The Journal of Neuroscience*. **39**(7), 1301–1319.

Schmidt, B., Duin, A.A., Redish, A.D. (2019) Disrupting the medial prefrontal cortex alters hippocampal sequences during deliberative decision making. *Journal of Neurophysiology*. **121**(6), 1981–2000.

Schölvinck, M.L., Maier, A., Ye, F.Q., Duyn, J.H., Leopold, D.A. (2010) Neural basis of global resting-state fMRI activity. *Proceedings of the National Academy of Sciences*. **107**(22), 10238–10243.

Schreiber, T. (2000) Measuring Information Transfer. *Physical Review Letters*. **85**(2), 461–464.

Schwarz, L.A., Miyamichi, K., Gao, X.J., Beier, K.T., Weissbourd, B., DeLoach, K.E., Ren, J., Ibanes, S., Malenka, R.C., Kremer, E.J., Luo, L. (2015) Viral-genetic tracing of the input–output organization of a central noradrenaline circuit. *Nature*. **524**(7563), 88–92.

Sforazzini, F., Bertero, A., Dodero, L., David, G., Galbusera, A., Scattoni, M.L., Pasqualetti, M., Gozzi, A. (2016) Altered functional connectivity networks in acallosal and socially impaired BTBR mice. *Brain Structure and Function*. **221**(2), 941–954.

Sforazzini, F., Schwarz, A.J., Galbusera, A., Bifone, A., Gozzi, A. (2014) Distributed BOLD and CBV-weighted resting-state networks in the mouse brain. *NeuroImage*. **87**, 403–415.

Siegel, J.S., Ramsey, L.E., Snyder, A.Z., Metcalf, N. V., Chacko, R. V., Weinberger, K., Baldassarre, A., Hacker, C.D., Shulman, G.L., Corbetta, M. (2016) Disruptions of network connectivity predict impairment in multiple behavioral domains after stroke. *Proceedings of the National Academy of Sciences*. **113**(30).

Siegel, M., Donner, T.H., Engel, A.K. (2012) Spectral fingerprints of large-scale neuronal interactions. *Nature Reviews Neuroscience*. **13**(2), 121–134.

- Siegel, M., Donner, T.H., Oostenveld, R., Fries, P., Engel, A.K. (2008) Neuronal Synchronization along the Dorsal Visual Pathway Reflects the Focus of Spatial Attention. *Neuron*. **60**(4), 709–719.
- Singer, W. (1999) Neuronal Synchrony: A Versatile Code for the Definition of Relations? *Neuron*. **24**(1), 49–65.
- Sohal, V.S., Rubenstein, J.L.R. (2019) Excitation-inhibition balance as a framework for investigating mechanisms in neuropsychiatric disorders. *Molecular Psychiatry*. **24**(9), 1248–1257.
- Van Someren, E.J.W., Van Der Werf, Y.D., Roelfsema, P.R., Mansvelder, H.D., Lopes da Silva, F.H. (2011) Slow brain oscillations of sleep, resting state, and vigilance. In pp. 3–15.
- Steriade, M., Amzica, F., Nunez, A. (1993) Cholinergic and noradrenergic modulation of the slow (approximately 0.3 Hz) oscillation in neocortical cells. *Journal of Neurophysiology*. **70**(4), 1385–1400.
- Steriade, M., McCormick, D.A., Sejnowski, T.J. (1993) Thalamocortical Oscillations in the Sleeping and Aroused Brain. *Science*. **262**(5134), 679–685.
- Strens, L.H., Oliviero, A., Bloem, B.R., Gerschlag, W., Rothwell, J.C., Brown, P. (2002) The effects of subthreshold 1 Hz repetitive TMS on cortico-cortical and interhemispheric coherence. *Clinical Neurophysiology*. **113**(8), 1279–1285.
- Stringer, C., Pachitariu, M., Steinmetz, N., Reddy, C.B., Carandini, M., Harris, K.D. (2019) Spontaneous behaviors drive multidimensional, brainwide activity. *Science*. **364**(6437).
- Suárez, L.E., Markello, R.D., Betzel, R.F., Misic, B. (2020) Linking Structure and Function in Macroscale Brain Networks. *Trends in Cognitive Sciences*. **24**(4), 302–315.
- Swanson, L.W. (1976) The locus coeruleus: A cytoarchitectonic, golgi and immunohistochemical study in the albino rat. *Brain Research*. **110**(1), 39–56.
- Swanson, L.W., Hartman, B.K. (1975) The central adrenergic system. An immunofluorescence study of the location of cell bodies and their efferent connections in the rat utilizing dopamine-B-hydroxylase as a marker. *The Journal of Comparative Neurology*. **163**(4), 467–505.
- Total, N.K., Neves, R.M., Panzeri, S., Logothetis, N.K., Eschenko, O. (2018) The Locus Coeruleus Is a Complex and Differentiated Neuromodulatory System. *Neuron*. **99**(5), 1055–1068.e6.
- Total, N.K.B., Logothetis, N.K., Eschenko, O. (2019) Noradrenergic ensemble-based modulation of cognition over multiple timescales. *Brain Research*. **1709**, 50–66.
- Trakoshis, S., Martínez-Cañada, P., Rocchi, F., Canella, C., You, W., Chakrabarti, B., Ruigrok, A.N., Bullmore, E.T., Suckling, J., Markicevic, M., Zerbi, V., Baron-Cohen, S., Gozzi, A., Lai, M.-C., Panzeri, S., Lombardo, M. V (2020) Intrinsic excitation-inhibition imbalance affects medial prefrontal cortex differently in autistic men versus women. *eLife*. **9**.
- Tu, W., Ma, Z., Ma, Y., Dopfel, D., Zhang, N. (2021) Suppressing Anterior Cingulate Cortex Modulates Default Mode Network and Behavior in Awake Rats. *Cerebral Cortex*. **31**(1), 312–323.
- Tung, C.-S., Ugedo, L., Grenhoff, J., Engberg, G., Svensson, T.H. (1989) Peripheral induction of burst firing in locus coeruleus neurons by nicotine mediated via excitatory amino acids. *Synapse*. **4**(4), 313–318.

- Turchi, J., Chang, C., Ye, F.Q., Russ, B.E., Yu, D.K., Cortes, C.R., Monosov, I.E., Duyn, J.H., Leopold, D.A. (2018) The Basal Forebrain Regulates Global Resting-State fMRI Fluctuations. *Neuron*. **97**(4), 940–952.e4.
- Tyszka, J.M., Kennedy, D.P., Adolphs, R., Paul, L.K. (2011) Intact Bilateral Resting-State Networks in the Absence of the Corpus Callosum. *Journal of Neuroscience*. **31**(42), 15154–15162.
- Uematsu, A., Tan, B.Z., Johansen, J.P. (2015) Projection specificity in heterogeneous locus coeruleus cell populations: implications for learning and memory. *Learning & Memory*. **22**(9), 444–451.
- Uematsu, A., Tan, B.Z., Ycu, E.A., Cuevas, J.S., Koivumaa, J., Junyent, F., Kremer, E.J., Witten, I.B., Deisseroth, K., Johansen, J.P. (2017) Modular organization of the brainstem noradrenaline system coordinates opposing learning states. *Nature Neuroscience*. **20**(11), 1602–1611.
- Vincent, J.L., Patel, G.H., Fox, M.D., Snyder, A.Z., Baker, J.T., Van Essen, D.C., Zempel, J.M., Snyder, L.H., Corbetta, M., Raichle, M.E. (2007) Intrinsic functional architecture in the anaesthetized monkey brain. *Nature*. **447**(7140), 83–86.
- Vogt, B.A., Paxinos, G. (2014) Cytoarchitecture of mouse and rat cingulate cortex with human homologies. *Brain Structure and Function*. **219**(1), 185–192.
- Wang, L., Hermens, D.F., Hickie, I.B., Lagopoulos, J. (2012) A systematic review of resting-state functional-MRI studies in major depression. *Journal of Affective Disorders*. **142**(1–3), 6–12.
- Wang, L., Saalmann, Y.B., Pinsk, M.A., Arcaro, M.J., Kastner, S. (2012) Electrophysiological Low-Frequency Coherence and Cross-Frequency Coupling Contribute to BOLD Connectivity. *Neuron*. **76**(5), 1010–1020.
- Wang, Z., Chen, L.M., Négyessy, L., Friedman, R.M., Mishra, A., Gore, J.C., Roe, A.W. (2013) The Relationship of Anatomical and Functional Connectivity to Resting-State Connectivity in Primate Somatosensory Cortex. *Neuron*. **78**(6), 1116–1126.
- Watanabe, T., Hanajima, R., Shirota, Y., Ohminami, S., Tsutsumi, R., Terao, Y., Ugawa, Y., Hirose, S., Miyashita, Y., Konishi, S., Kunimatsu, A., Ohtomo, K. (2014) Bidirectional effects on interhemispheric resting-state functional connectivity induced by excitatory and inhibitory repetitive transcranial magnetic stimulation. *Human Brain Mapping*. **35**(5), 1896–1905.
- Waterhouse, B.D., Woodward, D.J. (1980) Interaction of norepinephrine with cerebrocortical activity evoked by stimulation of somatosensory afferent pathways in the rat☆. *Experimental Neurology*. **67**(1), 11–34.
- Welch, P. (1967) The use of fast Fourier transform for the estimation of power spectra: A method based on time averaging over short, modified periodograms. *IEEE Transactions on Audio and Electroacoustics*. **15**(2), 70–73.
- Whitesell, J.D., Liska, A., Coletta, L., Hirokawa, K.E., Bohn, P., Williford, A., Groblewski, P.A., Graddis, N., Kuan, L., Knox, J.E., Ho, A., Wakeman, W., Nicovich, P.R., Nguyen, T.N., van Velthoven, C.T.J., Garren, E., Fong, O., Naeemi, M., Henry, A.M., Dee, N., Smith, K.A., Levi, B., Feng, D., Ng, L., Tasic, B., Zeng, H., Mihalas, S., Gozzi, A., Harris, J.A. (2021) Regional, Layer, and Cell-Type-Specific Connectivity of the Mouse Default Mode Network. *Neuron*. **109**(3), 545–559.e8.

- Wiegert, J.S., Mahn, M., Prigge, M., Printz, Y., Yizhar, O. (2017) Silencing Neurons: Tools, Applications, and Experimental Constraints. *Neuron*. **95**(3), 504–529.
- Williams, A.H., Kim, T.H., Wang, F., Vyas, S., Ryu, S.I., Shenoy, K. V., Schnitzer, M., Kolda, T.G., Ganguli, S. (2018) Unsupervised Discovery of Demixed, Low-Dimensional Neural Dynamics across Multiple Timescales through Tensor Component Analysis. *Neuron*. **98**(6), 1099–1115.e8.
- Wu, G.-R., Liao, W., Stramaglia, S., Ding, J.-R., Chen, H., Marinazzo, D. (2013) A blind deconvolution approach to recover effective connectivity brain networks from resting state fMRI data. *Medical Image Analysis*. **17**(3), 365–374.
- Xue, M., Atallah, B. V., Scanziani, M. (2014) Equalizing excitation–inhibition ratios across visual cortical neurons. *Nature*. **511**(7511), 596–600.
- Zerbi, V., Pagani, M., Markicevic, M., Matteoli, M., Pozzi, D., Fagiolini, M., Bozzi, Y., Galbusera, A., Scattoni, M.L., Provenzano, G., Banerjee, A., Helmchen, F., Basson, M.A., Ellegood, J., Lerch, J.P., Rudin, M., Gozzi, A., Wenderoth, N. (2021) Brain mapping across 16 autism mouse models reveals a spectrum of functional connectivity subtypes. *Molecular Psychiatry*. **26**(12), 7610–7620.

